University of California

Los Angeles

Large Scale Dislocation Dynamics Simulation of Bulk Deformation

A dissertation submitted in partial satisfaction

of the requirements for the degree

Doctor of Philosophy in Mechanical and Aerospace Engineering

by

Zhiqiang Wang

2004

The dissertation of Zhiqiang Wang is approved.

A.K. Mal

L. Pilon

J.S. Chen

R. LeSar

N.M. Ghoniem, Committee Chair

University of California, Los Angeles

2004

To my parents and my wife Jennifer...

for their love and encouragement

Table of Contents

List of Figures

List of Tables

Acknowledgments

First of all, I want to thank Professor Nasr Ghoniem for his great guide in my academic study and research, for his patience and his care during the past five years. Then, I would like to thank Dr. Richard LeSar for his knowledgable ideas and help in our collaborations. My thanks go to other members on my doctoral committee, Professor A. Mal, Professor L. Pilon and Professor J.S. Chen, for their efforts and time to participate in the final defense. I also like to thank everyone in the Computational Nano&Micro Mechanics Lab for their help and the wonderful time we spent together.

Vita

1977	Born, a small village in China.
1995-1999	B.S., Mechanical Engineering, University of Science and Technology of China, Hefei, China.
1999-2004	PhD, Mechanical and Aerospace Engineering, University of California, Los Angeles, USA.

Publications

Zhiqiang Wang, Sriram Swaminarayan, Nasr Ghoniem and Richard Lesar, "Parallel Implementation of Large Scale Dislocation Dynamics Code with Hierarchical Tree Algorithm", to be submitted to *Journal of Computational Physics*.

Zhiqiang Wang, Nasr Ghoniem and Richard Lesar, "Multipole Representation of the Elastic Field of Dislocation Ensembles", *Physical Review B*, 69(17): (2004) 174102-07.

Zhiqiang Wang, Rodney J. McCabe, Nasr Ghoniem, Richard Lesar, Amit Misra, and Terence E. Mitchell, "Dislocation Motion in Thin Cu Foils: Comparison between Computer Simulation and Experiment", *Acta. Materialia*, 52(6): (2004) 1535-1542.

X. Han, N.M. Ghoniem and Z.Q. Wang, "Parametric Dislocation Dynamics of Anisotropic Crystalline Materials", *Philosophical Magazine A*, 83(31-34): (2003) 3705-3721.

N.M. Ghoniem, J.M. Huang and Z.Q. Wang, "Affine Covariant-contravariant Vector Forms for the Elastic Field of Parametric Dislocations in Isotropic Crystals", *Philosophical Magazine Letters*, 82(2): (2002) 55-63.

L.Z. Sun, N.M. Ghoniem and Z.Q. Wang, "Analytical and Numerical Determination of the Elastic Interaction Energy between Glissile Dislocations and Stacking Fault Tetrahedra in FCC Metals", *Journal of Materials Science & Engineering*, A309-310: (2001) 178-183.

Abstract of the Dissertation

Large Scale Dislocation Dynamics Simulation of Bulk Deformation

by

Zhiqiang Wang

Doctor of Philosophy in Mechanical and Aerospace Engineering

University of California, Los Angeles, 2004

Professor N.M. Ghoniem, Chair

In this work, the method of Parametric Dislocation Dynamics (PDD) is utilized to develop new computational methods for the simulation of crystal plasticity at the microscale. A vector form of the elastic field is developed and utilized within the PDD framework. A new theoretical treatment for the elastic field of dislocation ensembles has resulted in a multipole expansion, which is shown to be convergent for distance greater than the size of the cell containing the dislocation ensemble. The method is shown to be very efficient for calculations of the long-range elastic field.

A parallel computer code for the simulation of single crystal plasticity is developed. Some of the fundamental concerns involved in dislocation interactions have been calibrated by direct comparison with in-situ experiments on thin film copper foils. Simulations of the elasto-plastic deformation of 5 and 10 micron size single copper crystals are performed. Predictions of the work hardening and microstructure are shown to be consistent with experiments.

CHAPTER 1

Introduction

Recently, considerable progress has been made on the development of computational methods based on the elastic theory of dislocations. One of the main reasons for the rapid development of this area is the interest in computational modelling of material deformation in multi-scales and in the concept of materials-by-design. Computational modeling of the behavior of materials is able to avoid time-consuming and expensive experiments for material evaluation and design in many engineering applications. This work focuses on using a newly developed tool of parametric dislocation dynamics (PDD) to solve some critical problems of plasticity which exist in science and technologies. In this chapter, we first discuss the relationship between dislocations and plasticity of metals. Current research activities in the area will also be reviewed. Then, some experimental results of the problems concerned in the work, work-hardening of single crystals and surface deformation, will be presented. In followed chapters, details of the formulation of PDD model and the implementation of a parallel simulation method will be first presented. Validation of the PDD model with experimental results will be discussed next. Then, applications of the parallel method for work hardening of FCC Cu, the multipole expansion method and statistical extrapolation method for large scale simulations will be presented. Finally, conclusions will be given in the last chapter.

1.1 Material Plasticity and Dislocation Dynamics

Since dislocations are the primary carriers of the plastic deformation of materials, dislocation theory has become a very active research area and is used to understand many of the physical and mechanical properties of crystalline materials. Single dislocation properties have been extensively studied and are well established in past decades. These theories can be applied to explain various phenomena, such as work hardening, crystal growth and grain boundary structure. Considerable successes have been achieved in understanding crystal plasticity by applying these theories. However, full understanding of this problem is still a daunting task for the research community. For simple cases, analytical solutions can be obtained, or simple numerical simulations can be done based on theories of single dislocations. However, for much more complex cases (such as 3D microstructure), even for some simple cases(such as surface image forces), and for cases with a large number of dislocations, it is impossible to obtain analytical solutions for the elastic fields. Thus, new descriptions and numerical simulations of dislocations are a challenge for further understanding of fundamental aspects of the plasticity.

Because the macroscopic mechanical properties are the averages of microscopic events, single dislocation theory can not explain and predict the mechanical behavior of bulk materials containing ensembles of dislocations. To study the plastic flow in crystalline materials, the size of the specimen and the characteristic length scale associated with the external loading must be larger than the size of the dislocation micro-structure so that macroscopic properties can be averaged out to the continuum level[1]. Thus, it is apparent that a model of collective of dislocations is needed. Dislocation dynamics (DD), which is based on single dislocation theory and tries to simulate populations of dislocations with a computer,

is proposed to accomplish this task. In recent years, dislocation dynamics has had significant interest because of its power to simulate material deformation. Several 3D dislocation dynamics models have been recently proposed[2, 3, 4, 5, 6, 7]. The following is a brief review of the models from several major groups, which have large-scale DD capabilities.

1.1.1 The ONERA (France) Group

The ONERA group in france has developed a method to simulate dislocation behavior in materials[7, 5, 8, 9, 10]. Dislocation lines are divided into straight segments. These segments are of pure screw or pure edge characters. The effective shear stress acting on dislocations are calculated from interactions with other dislocations, applied forces, self-interactions and free surface image forces. After the effective shear stress is determined, the velocity of a dislocation segment is described in relation as:

$$v = \frac{\tau^* b}{B} \tag{1.1}$$

where τ^* is the effective shear stress on dislocation, B is the temperature-dependent dislocation mobility.

Then, the dislocation glide follows a Newtonian dynamics such that:

$$x(t + \triangle t) = x(t) + v \times \triangle t \tag{1.2}$$

For large scale simulation, the simulated box is divided into a periodic lattice of overlapping sub-boxes. Based on the assumption that the long range interaction contributions to the local internal stresses vary smoothly in space and slowly in time, the interactions of the segments inside the same sub-box are computed each step. The contribution from other sub-boxes is evaluated only at the center of the considered box and is not evaluated every such often as former one.

The method has been applied to study both individual dislocation behaviors and collective dislocation behaviors. For example, figure 1.1 shows that a dislocation Frank-Read source interacts with a forest of many dislocation segments. The relation between hardening rate and the density of the forest dislocations has been obtained from the study.

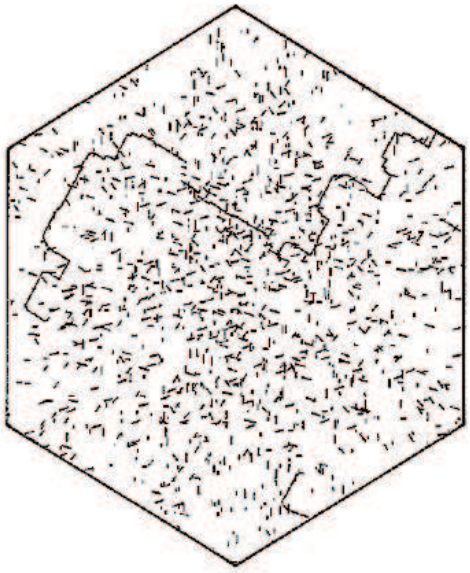

Figure 1.1: A dislocation interacts with a forest of dislocation segments[7].

The method is also applied to study the early stages of the formation of dislocation microstructures in low-strain fatigue[11]. Simulations under various conditions of loading amplitude and grain size have been performed. Both the dislocation microstructures and the associated mechanical behavior are accurately reproduced in single-slip as well as in double-slip loading conditions. The microstructures thus obtained are analyzed quantitatively, in terms of number of slip bands per grain, band thickness and band spacing. Figure 1.2 shows the dislocation microstructure under different different applied loads.

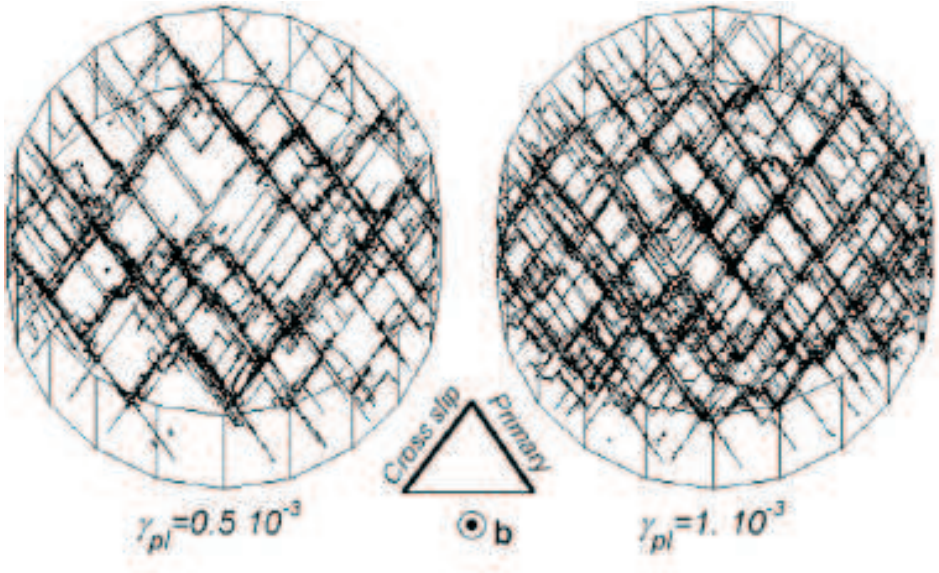

Figure 1.2: Effect of the applied strain amplitude on dislocation microstructure in fatigue deformation[11].

1.1.2 Washington State University Group

The group at Washington State University developed a similar dislocation dynamics method based on straight segments[4, 12, 13, 6]. Different from the ONERA group, these segments are not pure screw or pure edge, but with mixed characters.

In this method, the driving forces **F** for dislocation motions are evaluated at the center of each segment. Especially, interaction from adjacent segments, including line-tension and self-interaction, are computed explicitly based on a model for straight semi-infinite segments. Once the forces are determined, dislocation velocities are known from the velocity-stress relationship:

$$(m_i^* + \frac{1}{M_i(T,p)})\dot{\mathbf{X}}_i = \mathbf{F}_i \tag{1.3}$$

where m_i^* is the effective mass per unit dislocation, M is the mobility which could depend on temperature T and pressure p, and X is the position of a dislocation node.

Then, nodal positions of dislocation segments are solved for the next time step by $X^{t+\triangle t} = X^t + \dot{X}^t \times \triangle t$, where $\triangle t$ is the time step.

Periodic boundary conditions are used in their simulations. To deal with long range interactions, a model of superdislocations (SD) is introduced. The simulated crystal is divided into cubic cells. Within each cell, the interaction from nearest cells is determined directly. For distant cells, the fields are approximated by SDs, where the field of each SD is the same as that of a single dislocation but with a modified magnitude of the Burgers vector.

The method is applied to study the crystal plasticity, such as problems of dislocation interaction with point defects, dislocation patterning and localization. Figure 1.3 shows a pattern of deformation formed inside single crystal copper under a tensile load. The corresponding dislocation microstructure is shown in figure 1.3 (b).

1.1.3 IBM Group

At IBM, a parallel dislocation dynamics code, PARANOID, was developed by a group led by K. Schwarz [15, 16, 17]. In their model, dislocations are represented as segments with mixed characters. The basic equations of dislocation motion are the same as described above. A modified Brown procedure (splitting the dislocation in half, moving the two halves outward by some core parameter and averaging the result) is utilized to obtain the self-interaction, which remains stable and loses accuracy in a controlled manner as the length scale approaches the atomic level. Rules for strong dislocation interactions are discovered and are

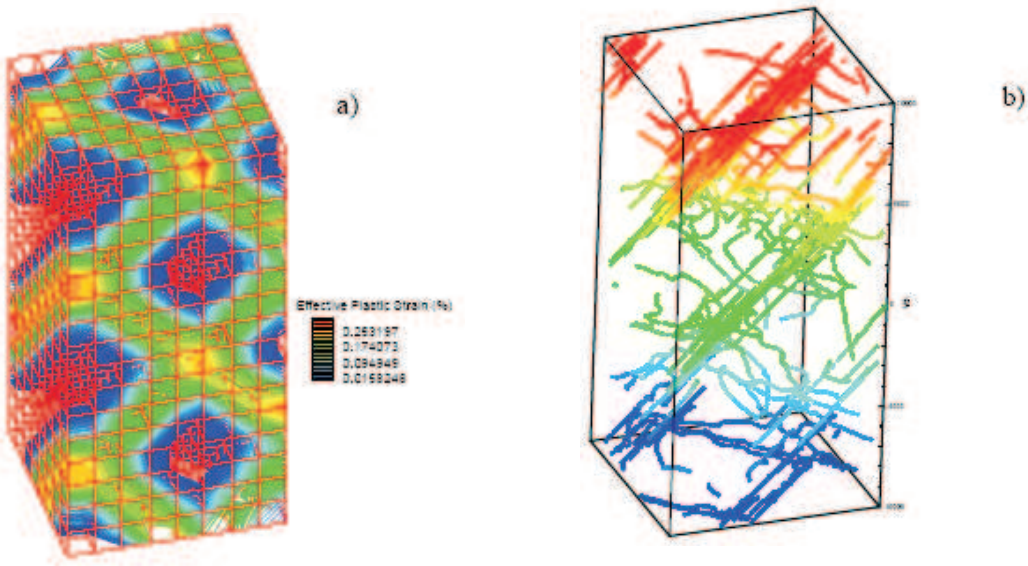

Figure 1.3: (a) Distribution of the plastic strain showing the formation of a cell pattern, (b) the corresponding dislocation pattern[14].

applied to both FCC and BCC crystals.

The code is parallelized to run on IBM clusters. The primary application of the code is to investigate dislocation motion in thin films and semiconductor devices. For example, strain relaxation in thin films (SiGe) are successfully studied. Dislocation networks previously observed from experiments are predicted from simulation. The study also demonstrate that the pairing of the threading dislocations on parallel glide plane is by far the strongest mechanism for immobilizing such dislocations in a thin film.

1.1.4 LLNL Group

Lawrence Livermore National Laboratory group has developed a highly paralleled dislocation dynamics code, ParaDis, to explore the single crystal hardening process[18]. The code is utilizing the huge computational power from fastest su-

percomputers and begins to show the potential of directly computing the strength of materials from collective behavior of dislocations. In the code, dislocations are represented by a network of nodes (figure 1.4). Each node can have two or more segments connecting to neighbor nodes, and each segment carries out a unit of Burgers vector, which denotes the direction and magnitude of the displacement that occurs when a dislocation moves. The nodes moves according to the first order equation of motion:

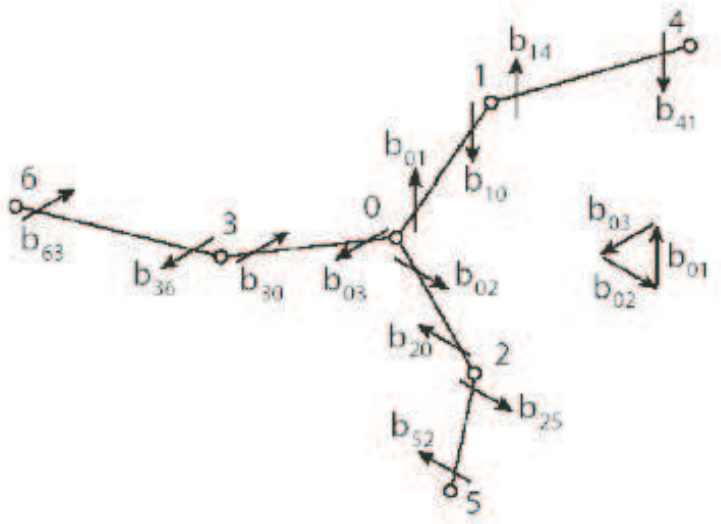

Figure 1.4: A fragment of the dislocation lines network: each line segment xy carries a unit of "vector current" quantified by Burgers vector b_{xy}[18].

$$\begin{aligned} \frac{d\vec{r_i}}{dt} &= M[\vec{f_i}] \\ \vec{f_i} &= -\frac{\partial E[\{\vec{r_i}\}]}{\partial \vec{r_i}} \end{aligned} \tag{1.4}$$

where f_i is the force on node i, E is the energy of the dislocation network, and $M[f_i]$ is a mobility function giving the velocity of node i as a function of node force

f_i. The network energy E includes the interaction between all network segments and between the segments and applied stress. In addition to moving the nodes, ParaDiS evolves the network topology to reflect the physics of dislocation motion and collisions in real crystals by adding or deleting certain nodes.

The code has been running on LLNL supercomputers on simulating single crystal deformation. Two typical outputs are shown in figure 1.5. Transition stages of the stress-strain curves were obtained.

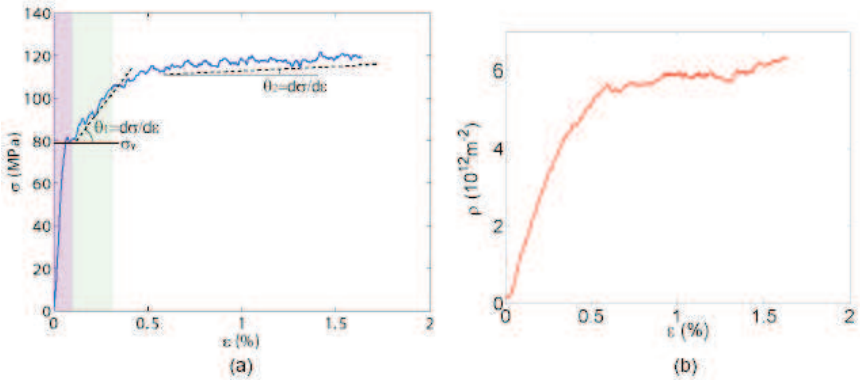

Figure 1.5: (a) Mechanical strength of single crystal molybdenum computed in a single ParaDiS simulation, (b)the behavior of the total density of dislocation lines as a function of strain[18].

Although various dislocation dynamics models discussed above have been applied to solve problems of material plasticity, there are limitations on these work. For example, meshing of dislocation loops with straight segments brings singularities at the connecting points of two such segments in calculation of self-forces of dislocation loops. Also, no accurate consideration of the long-range interaction between dislocations has been developed so far for large scale simulations. In this work, such problems are targeted with a parametric description of the dislocation loops. Applications of the model to single crystal plasticity and work-hardening of copper have been carried out based on an efficient parallel computer code

without requiring supercomputers.

1.2 Multiscale Simulations of Materials

In recent years, with the understanding that material strength is intrinsically a problem at different length and time scales, concepts of multi-scale material plasticity have been introduced to connect various length scales together [19, 20]. The main scales are atomistic scale(nanometers), microscale(micrometers), mesoscale(hundreds of micrometers) and continuum scale(larger than 100 micrometers). Multiscale simulations use a message-passing framework to transfer some information obtained from the small scale to larger scale. In meso-scale, dislocation theory is a tool for determining the physical and mechanical properties. Dislocation dynamics is used to simulate the behavior of many dislocations in material deformation and connect micro-structure evolution with macro-scopic material properties. Driven by technical problems in the area of irradiated material damage, thin film size effects and nano-technology, DD has been rapidly developed during the past two decades. 2D simulations were first investigated by using infinite straight dislocation lines while 3D simulations are now under development.

Classical crystal theories have no length scale, so that they can not explain phenomena exhibiting size-dependence, e.g., in hardness of micro-indentation when the indent size is reduced down to a few microns for a typical crystal. This difficulty of meso-scale modelling requires a single crystal model to provide the constitutive law, which governs the deformation of single crystals as the input to larger length scale models. One of the objectives of DD is to predict the stress-strain curve of single crystals without using phenomenological material variables other than the basic dislocation velocity as a function of the internal stress, which

can be obtained from experiments or from atomic simulations. The simulation results can be used to explain phenomena such as work hardening.

1.3 Work Hardening Theory And Experimental Observations

A higher stress is required to deform a crystal with larger plastic deformation. This is called work (strain) hardening. Work hardening processes are categorized in 3 or more stages (Fig. 1.6), according to the work hardening rate $\theta = \frac{\delta\tau}{\delta\gamma}$, where τ is the resolved shear stress and γ is the shear strain[21]. Stage I is usually characterized with linear hardening, with a hardening rate $\theta = \mu/3000$. Stage II is characterized by a linear work hardening rate $\theta = \mu/300$, which is weakly sensitive to temperature and strain rate. Stage III begins when the flow curve deviates from linearity with the onset stress as τ_{III}, which is strongly temperature and strain rate dependent.

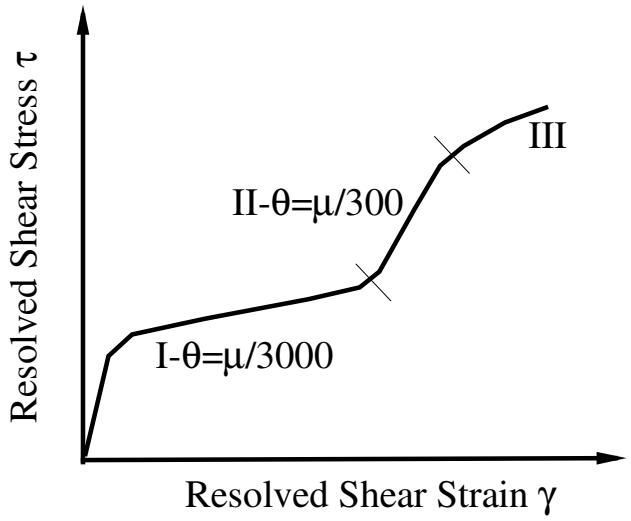

Figure 1.6: Schematic illustration of work hardening stages I-III

Each work hardening stage corresponds to some specific dislocation motion and microstructure[22]. In stage I, the hardening is mainly controlled by the motion of dislocations on primary glide planes. At the end of stage I, dislocations are concentrated in sheets or bundles of dipoles or multipoles. These sheets are parallel to primary glide planes and their spacing is inversely proportional to the resolved shear stress. In the transition region from stage I to stage II, the density of primary dislocations increases linearly while the density of other dislocations increases quadratically with the stress. After stage II is fully established, their densities are roughly the same. In stage II, dislocation cell structures (figure 1.7) [23] begin to form and the size of these cells are inversely proportional to the stress. In stage III, it is widely believed that cross-slip of dislocations controls the hardening, such that τ_{III} is generally considered as a critical stress value for many dislocations to cross-slip. In this stage, dislocations escape from their locks in stage II and internal stresses are relaxed such that the macroscopic stress begins to increase slowly than increasing strain. More 3D dislocation cell structures begin to form compared with 2D cell structures parallel to primary planes in stage II, and walls of cells become sharper and the interior of cells become clearer of dislocations. The sizes of these cells also decreases with increasing stress.

Anongba, Bonneville and Martin[24, 25] did a series of experiments to study work hardening of copper single crystals under different temperatures and strain rates. Their experiments have been able to characterize the hardening stages on the stress-strain curves. Below is a brief review of their observations.

The experiments were done for single copper crystals at 3 strain rates as $2 \times 10^{-4}\ s^{-1}$, $2 \times 10^{-3}\ s^{-1}$, and $2 \times 10^{-2}\ s^{-1}$. The applied tension is in the direction of [112]which initially activated two primary slip systems $[101]/(\bar{1}11)$ and $[011]/(1\bar{1}1)$. So, these experiments are multi-slip cases which have no stage I hard-

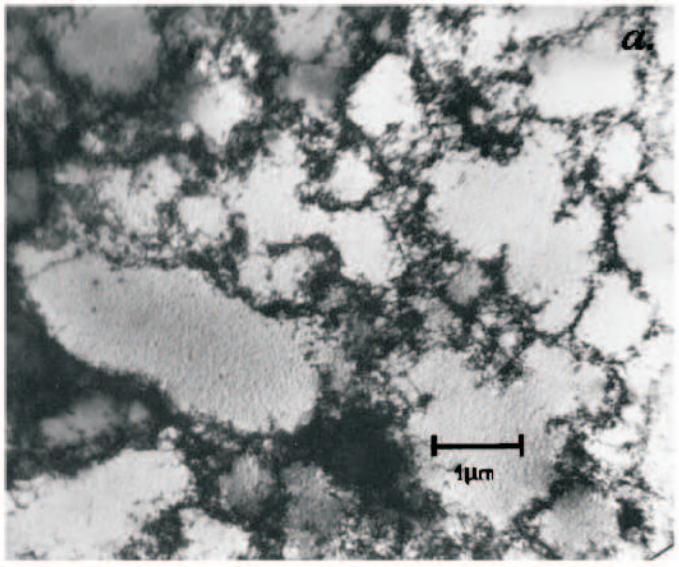

Figure 1.7: Dislocation cell structure in copper single crystal[23].

ening specifically for single slip. The resolved shear stress τ and resolved shear strain γ are calculated with respect to the Schmid factor m, and the hardening rate θ is calculated by numerically differentiating τ with respect to γ. Temperatures vary from $483K$ to $1133K$, which are divided into 3 zones as $483K - 678K$, $874K - 1064K$, $935K - 1133K$ for different strain rates. Typical results are shown in figure 1.8 1.10).

At room temperature (figure 1.8), normal stage II and stage III are observed. Figure 1.8 (b) shows the hardening rate calculated. For stage II, a constant hardening rate $\theta_{II} \approx \frac{\mu}{300}$ is measured. For stage III, the hardening rate decreases linearly as stress increases, in agreement with previous observations[26, 27].

At higher temperatures, in addition to stage II and III, two more new hardening stages, IV and V, have been observed (figure 1.9 and 1.10). Figure 1.9 (b) and figure 1.10 (b) shows that stage IV is characterized by a constant or increasing rate of hardening with stress, while at the same time stage V has a hardening

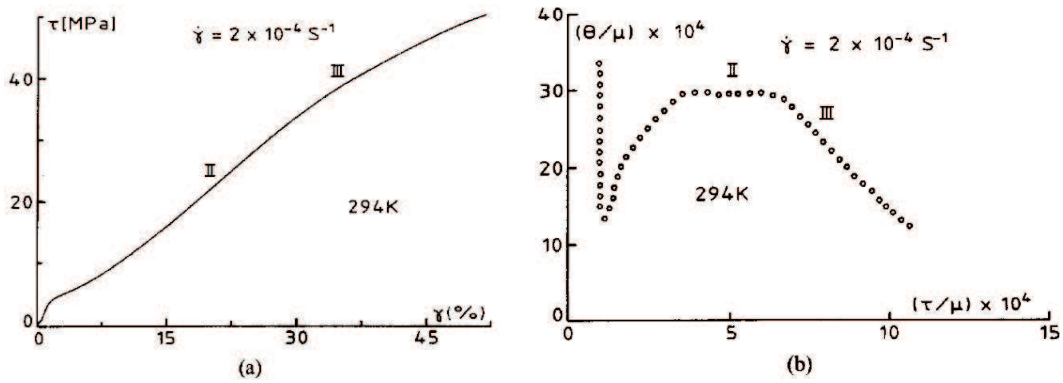

Figure 1.8: Experimental results at temperature $294K$ for strain rate $2\times10^{-4}s^{-1}$, (a)strain-stress curves and (b) the associated hardening rates[24].

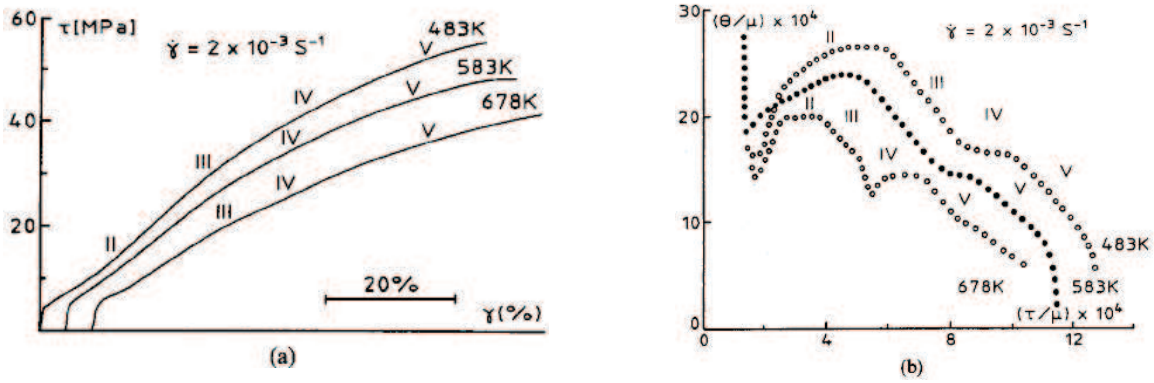

Figure 1.9: Experimental results at temperature $483K$-$678K$ for strain rate $2\times10^{-3}s^{-1}$, (a) stress-strain curves and (b) the associated hardening rates[24].

rate decreasing with stress or remaining to be constant.

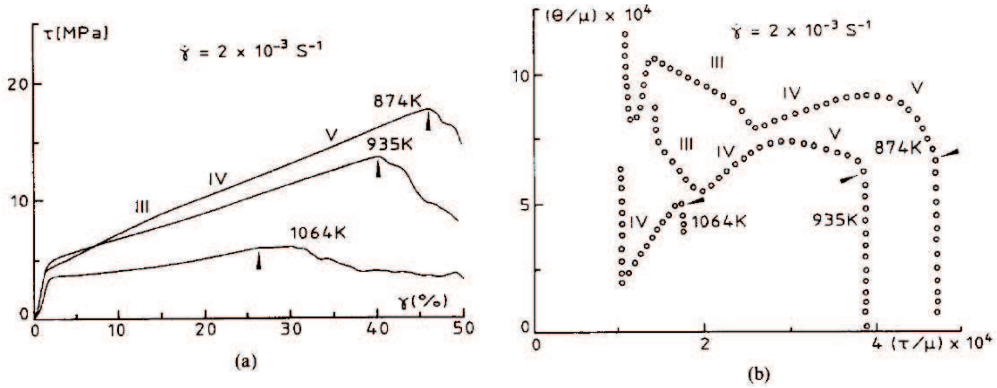

Figure 1.10: Experimental results at temperature $874K$-$1064K$ for strain rate $2 \times 10^{-3} s^{-1}$, (a) stress-strain curves and (b) the associated hardening rates[24].

The experimental results show that hardening rate is strongly temperature and stress dependent. In temperature regime 1 $(483K - 678K)$, θ is stress independent in stage II and IV and decreases when temperature is raised. In stage III and V, θ is decreasing with stress. In regime 2 $(874K - 1064K)$, stage II is not observed anymore. θ is still a decreasing function of stress in stage Ill and V, but increases in stage IV (figure 1.10). In regime 3 $(935K - 1133K)$, plastic deformation starts with stage IV where θ is temperature independent and increasing with stress. In stage V, θ is practically stress independent. The transition stresses for different hardening stages are found to be temperature and strain-rate dependent.

The experimental results provided detailed information on hardening stages with respect to stress and temperature. The study suggests that the origin of the observed hardening stages is the dislocation motion and microstructure formation under different strain rate and temperature.

1.4 Free Surface Problems and Dislocation Dynamics

More recently, free surface boundary conditions have been implemented in DD codes [9, 28], because dislocation interaction with the free surface plays a very important role in explaining many phenomena. Surface-dislocation interaction is significant in fatigue problems. Persistent slip bands (PSBs)(figure 1.11) [29] are always observed in materials under cyclic loading. They are formed with multi-parallel slip planes and large plastic deformation. These PSBs progressively elongate and finally reach the surface. When they intersect with the free surface, extrusions or intrusions form at the free surface [30]. These extrusions or intrusions are the source of micro cracks. After many cycles, extrusions and/or intrusions grow and fatigue cracks nucleate at these locations. Fatigue crack nucleation is believed to account for a substantial part of the fatigue life of components[31]. So, microstructure evolution is fundamental to understanding fatigue life of components.

Dislocation motion in thin films or in materials with free surfaces is different from that in bulk materials. Free surface boundary conditions must be satisfied, and the dislocation behavior is affected by an additional image stress field introduced by free surfaces. To study this type of surface related problems, coupling between surface effect on dislocations and surface deformation caused by dislocation loop evolution should be solved. 2D problems are relatively easy [32, 33, 34, 35, 36, 37]. In these cases, dislocations are either infinite, semi-infinite straight long, or parallel to the free surface. However, for 3D problems, proper accounting for surface effects becomes more complex, because dislocation loops are of finite size and are not straight. Also, they are not necessarily parallel to the free surface. Some researchers adopted the approximation of straight line image forces into 3D simulations [15]. In this case, surface effects are consid-

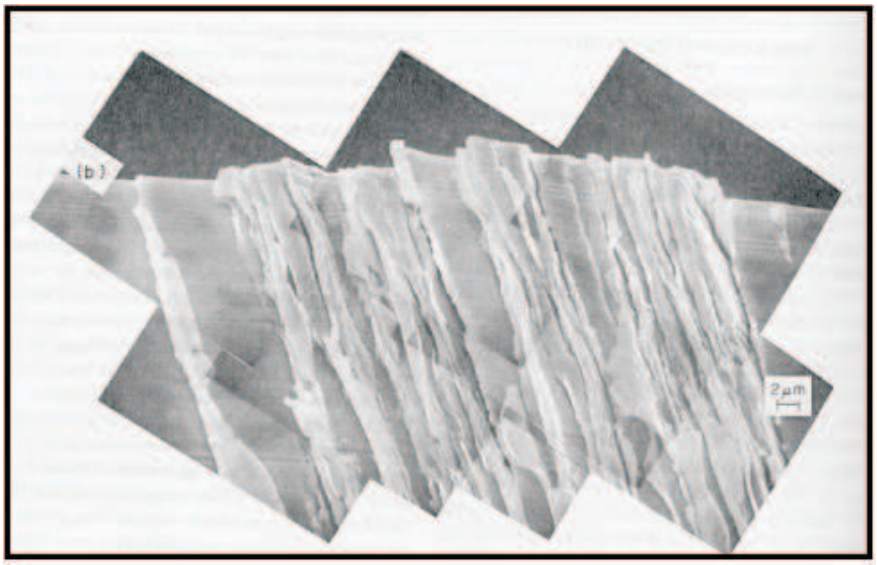

Figure 1.11: Surface roughness due to PSB/surface interaction in Cu crystal fatigue test. Strain amplitude 2×10^{-3}, 120000 cycles.

ered but not in a rigorous fashion. For greater accuracy, dislocation dynamics is combined with the finite element method to study surface image forces [28, 13], while other investigations implemented the Green's function method and the Boussinesq-point-force method[9, 10].

CHAPTER 2

Formulation of Parametric Dislocation Dynamics

The approach of dislocation dynamics (DD) was first applied to two-dimensional (2D), straight, infinitely long dislocations. When applied to 3-dimensional (3D) simulation of plastic deformation, it requires more calculations. It is also critical to get precise and simple equations to describe the mechanics of dislocations in solid materials for such numerical simulations. Such equations would be able to obtain accurate results of dislocation motions and interactions, maintain good 3D dislocation line shapes, while at the same time reduce the total number of dislocation segments to keep high computational efficiency for simulations of large systems. In this chapter, the parametric dislocation dynamics (PDD) formulation is presented, which includes the description of dislocation lines, the equations of motions, and the equations of dislocation fields for displacements, stresses and strains.

2.1 Parametric dislocation dynamics

Dislocations are line defects in materials. A parametric dislocation dynamics method has been developed[3, 38, 39, 40] for 3D simulations. This method is different from other methods that represent dislocation loops as many straight

segments[4, 5, 8, 15]. In this method, dislocation loops are divided into segments that are represented as cubic spline curves.

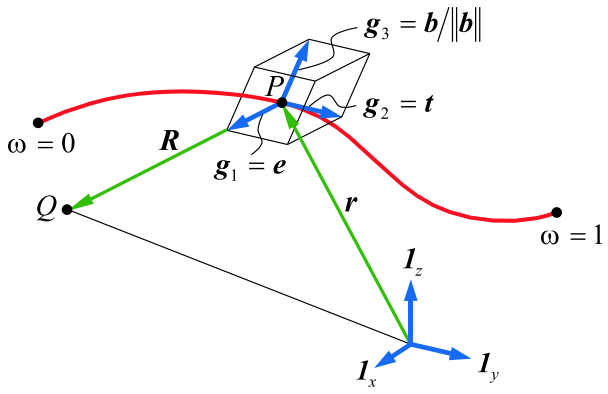

Figure 2.1: Differential geometrical representation of a general parametric curved dislocation segment

As shown in figure 2.1, segment j is expressed as a function of a variable ω, which is from 0 to 1, and the positions of two dislocation nodes:

$$\mathbf{r}^{(j)}(\omega) = \sum_{i=0}^{4} C_i(\omega)\mathbf{Q}_i \tag{2.1}$$

where $\mathbf{r}$ is the vector of a point on dislocation segment, $C_i(\omega)$ are general shape functions for cubic spline., $\mathbf{Q}_i$ are general coordinates of the dislocation nodes. $C_i(\omega)$ are:

$$\begin{aligned} C_1(\omega) &= 2\omega^3 - 3\omega^2 + 1 \\ C_2(\omega) &= -2\omega^3 + 3\omega^2 \\ C_3(\omega) &= \omega^3 - 2\omega^2 + \omega \\ C_4(\omega) &= \omega^3 - \omega^2 \end{aligned} \tag{2.2}$$

and $\mathbf{Q}_i$ are:

$$\begin{aligned} \mathbf{Q}_1 &= \mathbf{P}^{(j)}(0) \\ \mathbf{Q}_2 &= \mathbf{P}^{(j)}(1) \\ \mathbf{Q}_3 &= \mathbf{T}^{(j)}(0) \\ \mathbf{Q}_4 &= \mathbf{T}^{(j)}(1) \end{aligned} \tag{2.3}$$

where $\mathbf{P}^{(j)}(0)$ and $\mathbf{T}^{(j)}(0)$ are position and tangent vectors of the beginning point of segment j where $\omega = 0$, and $\mathbf{P}^{(j)}(1)$ and $\mathbf{T}^{(j)}(1)$ are position and tangent vectorss of the ending point of segment j where $\omega = 1$.

2.2 Equations of motion

A derivation based on thermodynamics has been developed to obtain a variational form for the equations of motion (EOM) for dislocation loops. The EOM is expressed as[3, 41]:

$$\oint_T (f_k^t - B_{\alpha k} V_\alpha) \delta r_k |ds| = 0 \tag{2.4}$$

where $B_{\alpha k}$ is the resistive matrix which is related to the mobility of dislocations, V_α is the velocity of dislocations, and $\mathbf{f}^t = \mathbf{f}_S + \mathbf{f}_O + \mathbf{f}_{PK}$ is the total force acting on the dislocations and is a summation of the self-force $\mathbf{f}_S$ of the dislocations, the osmotic force $\mathbf{f}_O$ and the Peach-Koehler force $\mathbf{f}_{PK}$. The Peach-Koehler force can be written as:

$$\mathbf{f}_{PK} = \mathbf{b} \cdot \Sigma \times \mathbf{t} \tag{2.5}$$

where $\mathbf{b}$ is the burgers vector of dislocations, $\mathbf{t}$ is the tangent vector of the dislocation lines, and Σ is the stress fields from applied stresses, interaction of dislocations, etc.

Suppose that the dislocation line is divided into N_s segments, by applying the

Galerkin method and using the fast-sum strategy[3], the equation of motion 2.4 can be written as:

$$F_k = \sum_{l=1}^{N_{total}} \Gamma_{kl} Q_{l,t} \tag{2.6}$$

where $[F_k]$ is the general force load, $[\Gamma_{kl}]$ is the general resistivity matrix and $[Q_{l,t}]$ is the general coordinates of dislocation nodes. By solving this equation, dislocation positions are obtained.

2.3 Affine vector forms of the elastic fields of dislocations

The displacement vector $\mathbf{u}$, strain ε and stress σ tensor fields of a closed dislocation loop need to be evaluated in the simulation. They are given by deWit (1960):

$$u_i = -\frac{b_i}{4\pi} \oint_C A_k dl_k + \frac{1}{8\pi} \oint_C \left[\epsilon_{ikl} b_l R_{,pp} + \frac{1}{1-\nu} \epsilon_{kmn} b_n R_{,mi} \right] dl_k \tag{2.7}$$

$$\varepsilon_{ij} = \frac{1}{8\pi} \oint_C \left[-\frac{1}{2} \left(\epsilon_{jkl} b_i R_{,l} + \epsilon_{ikl} b_j R_{,l} - \epsilon_{ikl} b_l R_{,j} - \epsilon_{jkl} b_l R_{,i} \right)_{,pp} \frac{\epsilon_{kmn} b_n R_{,mij}}{1-\nu} \right] dl_k \tag{2.8}$$

$$\sigma_{ij} = \frac{\mu}{4\pi} \oint_C \left[\frac{1}{2} R_{,mpp} \left(\epsilon_{jmn} dl_i + \epsilon_{imn} dl_j \right) + \frac{1}{1-\nu} \epsilon_{kmn} \left(R_{,ijm} - \delta_{ij} R_{,ppm} \right) dl_k \right] \tag{2.9}$$

Where μ & ν are the shear modulus and Poisson's ratio, respectively, $\mathbf{b}$ is Burgers vector of Cartesian components b_i, and the vector potential $A_k(\ \mathbf{R}) = \epsilon_{ijk} X_i s_j / [R(R + \mathbf{R} \cdot s)]$ satisfies the differential equation: $\epsilon_{pik} A_{k,p}(\ \mathbf{R}) = X_i R^{-3}$, where $\mathbf{s}$ is an arbitrary unit vector. The radius vector $\mathbf{R}$ connects a source point on the loop to a field point, as shown in Fig.2.1, with Cartesian components R_i,

successive partial derivatives $R_{,ijk....}$, and magnitude R. The line integrals are carried along the closed contour C defining the dislocation loop, of differential arc length $d\mathbf{l}$ of components dl_k. Also, the interaction energy between two closed loops with Burgers vectors $\mathbf{b}_1$ and $\mathbf{b}_2$, respectively, can be written as:

$$E_I = -\frac{\mu b_{1i} b_{2j}}{8\pi} \oint_{C^{(1)}} \oint_{C^{(2)}} \left[R_{,kk} \left(dl_{2j} dl_{1i} + \frac{2\nu}{1-\nu} dl_{2i} dl_{1j} \right) + \frac{2}{1-\nu} (R_{,ij} - \delta_{ij} R_{,ll}) dl_{2k} dl_{1k} \right] \tag{2.10}$$

The higher order derivatives of the radius vector, $R_{,ij}$ & $R_{,ijk}$ are components of second and third order Cartesian tensors, respectively, which can be cast in the form:

$$\begin{aligned} R_{,ij} &= \left(\delta_{ij} - \frac{X_i}{R}\frac{X_j}{R} \right) / R \\ R_{,ijk} &= \left(3\frac{X_i}{R}\frac{X_j}{R}\frac{X_k}{R} - \left[\delta_{ij}\frac{X_k}{R} + \delta_{jk}\frac{X_i}{R} + \delta_{ki}\frac{X_j}{R} \right] \right) / R^2 \end{aligned} \tag{2.11}$$

Where X_i are Cartesian components of $\mathbf{R}$. Substituting $R_{,ij}$ and $R_{,ijk}$ in Eqns.2.7-2.10, and considering the contributions only due to a differential vector element $d\mathbf{l}$, we obtain the differential relationships:

$$du_i = -\frac{b_i A_k dl_k}{4\pi} + \frac{1}{8\pi R(1-\nu)} \left[(1-2\nu)\epsilon_{ikl} b_l dl_k - \frac{1}{R^2} \epsilon_{kmn} b_n X_m X_i dl_k \right] \tag{2.12}$$

$$\begin{aligned} d\varepsilon_{ij} &= \frac{1}{8\pi} \left[\frac{1}{R^3} \left(\epsilon_{jkl} b_i X_l + \epsilon_{ikl} b_j X_l \right) dl_k + \frac{3}{R^5(1-\nu)} \epsilon_{kmn} b_n X_i X_j X_m dl_k \right. \\ &\quad - \frac{1}{R^3(1-\nu)} \epsilon_{kmn} b_n X_m \delta_{ij} dl_k + \frac{\nu}{R^3(1-\nu)} \epsilon_{jkl} b_l X_i dl_k \\ &\quad \left. + \frac{\nu}{R^3(1-\nu)} \epsilon_{ikn} b_n X_j dl_k \right] \end{aligned} \tag{2.13}$$

$$
\begin{aligned}
d\sigma_{ij} &= \frac{\mu}{4\pi}\frac{1}{R^3}\left[-\epsilon_{jmn}X_m b_n dl_i - \epsilon_{imn}X_m b_n dl_j\right. \\
&\quad + \frac{1}{1-\nu}\left(\frac{3}{R^2}\epsilon_{kmn}X_m b_n X_i X_j - \epsilon_{kjn}X_i b_n - \epsilon_{kin}X_j b_n\right. \\
&\quad \left.\left. + \epsilon_{kmn}X_m b_n \delta_{ij}\right) dl_k\right] \qquad (2.14)
\end{aligned}
$$

Fig.2.1 shows a parametric representation of a general curved dislocation line segment, which can be described by a parameter ω that varies, for example, from 0 to 1 at end nodes of the segment. The segment is fully determined as an affine mapping on the scalar interval $\in [0,1]$, if we introduce the tangent vector $\mathbf{T}$, the unit tangent vector $\mathbf{t}$, the unit radius vector $\mathbf{e}$, and the vector potential $\mathbf{A}$, as follows:

$$
\mathbf{T} = \frac{\mathbf{dl}}{d\omega},\ \mathbf{t} = \frac{\mathbf{T}}{|\mathbf{T}|},\ e = \frac{\mathbf{R}}{R},\quad \mathbf{A} = \frac{\mathbf{e}\times\mathbf{s}}{R(1+\mathbf{e}\cdot\mathbf{s})}
$$

The following relations can be readily verified:

$$
\begin{aligned}
A_k dl_k &= \mathbf{A}\cdot\mathbf{T}d\omega = Td\omega(\mathbf{A}\cdot\mathbf{t}) = \frac{Td\omega}{R}\cdot\frac{(\mathbf{e}\times\mathbf{s})\cdot\mathbf{t}}{1+\mathbf{e}\cdot\mathbf{s}} \\
\epsilon_{ikl}b_l dl_k \mathbf{e}_i &= -\mathbf{b}\times\mathbf{t} \\
\frac{1}{R^2}\epsilon_{kmn}b_n X_m X_i dl_k \mathbf{e}_i &= -\frac{1}{R^2}\epsilon_{knm}b_n X_m X_i dl_k \mathbf{e}_i \\
&= -\frac{d\omega}{R^2}[(\mathbf{T}\times\mathbf{b})\cdot\mathbf{R}]\ \mathbf{R} = -d\omega[(\mathbf{T}\times\mathbf{b})\cdot\mathbf{e}]\ \mathbf{e} \\
(\epsilon_{jkl}b_i X_l + \epsilon_{ikl}b_j X_l) dl_k \mathbf{e}_i\mathbf{e}_j &= \mathbf{b}\otimes(\mathbf{T}d\omega\times\mathbf{R}) + (\mathbf{T}d\omega\times\mathbf{R})\otimes\mathbf{b} \\
&= RTd\omega\ [\mathbf{b}\otimes(\mathbf{t}\times\mathbf{e}) + (\mathbf{t}\times\mathbf{e})\otimes\mathbf{b}] \\
\epsilon_{kmn}b_n X_i X_j X_m dl_k \mathbf{e}_i\mathbf{e}_j &= [(\mathbf{T}d\omega\times\mathbf{R})\cdot\mathbf{b}]\ \mathbf{R}\otimes\mathbf{R} = R^3 Td\omega[(\mathbf{t}\times\mathbf{e})\cdot\mathbf{b}]\ \mathbf{e}\otimes\mathbf{e} \\
\epsilon_{kmn}b_n X_m \delta_{ij} dl_k \mathbf{e}_i\mathbf{e}_j &= [(\mathbf{T}d\omega\times\mathbf{R})\cdot\mathbf{b}]\ \mathbf{I} = RTd\omega\ [(\mathbf{t}\times\mathbf{e})\cdot\mathbf{b}]\ \mathbf{I}
\end{aligned}
$$

Let the Cartesian orthogonal basis set be denoted by $\mathbf{1} \equiv \{\mathbf{1}_x, \mathbf{1}_y, \mathbf{1}_z\}$, $\mathbf{I} = \mathbf{1}\otimes\mathbf{1}$ as the second order unit tensor, and $\otimes$ denotes tensor product. Now define the three vectors ($\mathbf{g}_1 = \mathbf{e},\ \mathbf{g}_2 = \mathbf{t},\ \mathbf{g}_3 = \mathbf{b}/|\mathbf{b}|$) as a covariant basis set for the

curvilinear segment, and their contravariant reciprocals as: $\mathbf{g}^i \cdot \mathbf{g}_j = \delta^i_j$, where δ^i_j is the mixed Kronecker delta and $V = (\mathbf{g}_1 \times \mathbf{g}_2) \cdot \mathbf{g}_3$ the volume spanned by the vector basis, as shown in Fig. 2.1 [42]. When the previous relationships are substituted back into Eqns. 2.12-2.14, with $V_1 = (\mathbf{s} \times \mathbf{g}_1) \cdot \mathbf{g}_2$, and $\mathbf{s}$ an arbitrary unit vector, we obtain:

$$
\begin{aligned}
\frac{d\mathbf{u}}{d\omega} &= \frac{|\mathbf{b}||\mathbf{T}|V}{8\pi(1-\nu)R}\left\{\left[\frac{(1-\nu)V_1/V}{1+\mathbf{s}\cdot\mathbf{g}_1}\right]\mathbf{g}_3 + (1-2\nu)\mathbf{g}^1 + \mathbf{g}_1\right\} \\
\frac{d\varepsilon}{d\omega} &= -\frac{V|\mathbf{T}|}{8\pi(1-\nu)R^2}\left\{-\nu\left(\mathbf{g}^1\otimes\mathbf{g}_1 + \mathbf{g}_1\otimes\mathbf{g}^1\right) + (1-\nu)\left(\mathbf{g}^3\otimes\mathbf{g}_3 + \mathbf{g}_3\otimes\mathbf{g}^3\right)\right. \\
&\quad \left. + (3\mathbf{g}_1\otimes\mathbf{g}_1 - \mathbf{I})\right\} \\
\frac{d\sigma}{d\omega} &= \frac{\mu V|\mathbf{T}|}{4\pi(1-\nu)R^2}\left\{\left(\mathbf{g}^1\otimes\mathbf{g}_1 + \mathbf{g}_1\otimes\mathbf{g}^1\right) + (1-\nu)\left(\mathbf{g}^2\otimes\mathbf{g}_2 + \mathbf{g}_2\otimes\mathbf{g}^2\right)\right. \\
&\quad \left. - (3\mathbf{g}_1\otimes\mathbf{g}_1 + \mathbf{I})\right\} \\
\frac{d^2E_I}{d\omega_1 d\omega_2} &= -\frac{\mu|\mathbf{T}_1||\mathbf{b}_1||\mathbf{T}_2||\mathbf{b}_2|}{4\pi(1-\nu)R}\left\{(1-\nu)\left(\mathbf{g}_2^I\cdot\mathbf{g}_3^I\right)\left(\mathbf{g}_2^{II}\cdot\mathbf{g}_3^{II}\right) + 2\nu\left(\mathbf{g}_2^{II}\cdot\mathbf{g}_3^I\right)\left(\mathbf{g}_2^I\cdot\mathbf{g}_3^{II}\right)\right. \\
&\quad \left. - \left(\mathbf{g}_2^I\cdot\mathbf{g}_2^{II}\right)\left[\left(\mathbf{g}_3^I\cdot\mathbf{g}_3^{II}\right) + \left(\mathbf{g}_3^I\cdot\mathbf{g}_1\right)\left(\mathbf{g}_3^{II}\cdot\mathbf{g}_1\right)\right]\right\} \\
\frac{d^2E_S}{d\omega_1 d\omega_2} &= -\frac{\mu|\mathbf{T}_1||\mathbf{T}_2||\mathbf{b}|^2}{8\pi R\,(1-\nu)}\left\{(1+\nu)\left(\mathbf{g}_3\cdot\mathbf{g}_2^I\right)\left(\mathbf{g}_3\cdot\mathbf{g}_2^{II}\right) - \left[1+(\mathbf{g}_3\cdot\mathbf{g}_1)^2\right]\left(\mathbf{g}_2^I\cdot\mathbf{g}_2^{II}\right)\right\}
\end{aligned}
\tag{2.15}
$$

The superscripts $I\&II$ in the energy equations are for loops $I\&II$, respectively, and $\mathbf{g}_1$ is the unit vector along the line connecting two interacting points on the loops. The self energy is obtained by taking the limit of $\frac{1}{2}$ the interaction energy of two identical loops, separated by the core distance. Note that the interaction energy of prismatic loops would be simple, because $\mathbf{g}_3 \cdot \mathbf{g}_2 = 0$. The field equations are affine transformation mappings of the scalar interval neighborhood $d\omega$ to the vector ($d\mathbf{u}$) and second order tensor ($d\varepsilon,\ d\sigma$) neighborhoods, respectively, such that $d\mathbf{u} = \mathbf{U}d\omega,\ d\sigma = \mathbf{S}d\omega,\ d\varepsilon = \mathbf{E}d\omega$. The maps are given by the covariant, contravariant and mixed vector and tensor functions:

$$
\begin{aligned}
\mathbf{U} &= u^i \mathbf{g}_i + u_i \mathbf{g}^i \\
\mathbf{S} &= sym[tr(A^i_{.j} \mathbf{g}_i \otimes \mathbf{g}^j)] + A^{11}(3\mathbf{g}_1 \otimes \mathbf{g}_1 - \mathbf{1} \otimes \mathbf{1}) \\
\mathbf{E} &= sym[tr(B^i_{.j} \mathbf{g}_i \otimes \mathbf{g}^j)] + B^{11}(3\mathbf{g}_1 \otimes \mathbf{g}_1 + \mathbf{1} \otimes \mathbf{1})
\end{aligned}
\tag{2.16}
$$

The scalar metric coefficients $u_i, u^i, A^i_{.j}, B^i_{.j}, A^{11}, B^{11}$ are obtained by direct reduction of Eqn.2.15 into Eqn.2.16.

CHAPTER 3

Parallel Implementation of the UCLA-MICROPLASTICITY Computer Simulation

3.1 Introduction

Current major DD codes developed by several groups are limited to model only a small number of dislocations in a small volume of material because of the high increase in computational cost. Such high demand on computer resources results from dislocation interaction calculations for large scale simulations. The increase in computational time is on the order of N^2, where N is the number of interacting segments. To go beyond the current limitation, a larger volume of material and more dislocations are needed. To improve the computational capability, a parallel implementation should be applied to solve the problem instead of doing serial simulations on one computer.

Because of recent developments in computer technology, it is much easier to build a computer cluster instead of a super computer. A computer cluster is composed of many single PCs (cluster node), and parallel program codes can run on these nodes. Communication is possible between the cluster nodes and should be carefully taken care of. A special computer language library, called message passing interface (MPI), was developed for this purpose[43, 44]. Communications

can be done by calling the library subroutines. The computer program requires a good algorithm to partition the data space such that the data is distributed evenly on different cluster nodes. Among many parallel designs, one popular approach is the master-slave structure. One node is defined as a master, which is responsible for handling Input/Output, data management, etc, while the others are defined as slaves, which are responsible for doing the main calculation.

Large scale DD simulations share some similar properties as the so-called N-body problem in astrophysics, fluid mechanics, molecular dynamics, composite material design, etc. Many algorithms and their parallelization have been developed by scientists for large scale N-body simulation[45, 46, 47]. Thus, we can draw on existing experience in other fields for large scale DD simulations.

In this chapter, the N-body problem and several well-developed algorithms are first reviewed. Then, the parallel algorithm and the implementation of DD simulations will be discussed. Finally, numerical results of the parallel code are presented.

3.2 The N-body problem

The N-body problem refers to problems involving the behavior of N particles, which mutually interact with each other via a long-range force field. The difficulty to simulate such systems lies in the calculation of the interaction forces or energies between particles, which is on the order of N^2. It has long been a goal to decrease the problem complexity to $O(N^\alpha)$ where $\alpha < 2$. To decrease the order of the calculation, and thus to increase the speed of simulation requires a careful design of the computational algorithm.

Many approximate methods have been developed to reduce the computational

complexity. Two of the most famous ones are the Barnes-Hut(BH) method and the fast-multipole method(FMM)[48, 45]. The BH method has a computation complexity as $O(NlgN)$ and the FMM method as $O(N)$ if they are properly implemented. Both methods are based on the concept of hierarchical representation of the computational domain. A spatial tree is constructed with the following rules: the domain is represented as the root node of the tree and then is recursively split into sub-domains (sub-nodes of the tree) until each leaf of the tree contains only a certain number of particles (for the BH method, the number is 1, for FMM, it may be larger than 1). Each node in the tree contains geometrical information of the sub-domain it represents, such as the coordinates of the center point and its size. With the tree constructed, different approximate methods are applied in the BH and FMM methods. Both methods calculate the force on an individual object from close neighbors directly and from far neighbors approximately[45]. For the BH method, the far-field force is replaced by a single point mass located at its center of mass, which is then recursively applied to the tree. For the FMM method, the far-field force is approximated by a multipole expansion. A multipole acceptance criteria(MAC) is used to determine what kind of interaction(direct or approximate) should be included for each particle.

Parallel formulations for both methods exist in the literature[45, 49, 50, 51, 47]. After the computational domain is represented by a tree data structure, the partition of the domain takes place by splitting the tree structure and distributing different parts of the tree to individual processors. It is easy to partition the tree because the data is grouped together in the tree nodes. The partition is designed to minimize communications between different processors, and to balance the computational load between processors. To minimize communications between processors, particles that are close to each other are grouped together and sent to a single processor. For load balancing, the number of particles on each processor

is required to be approximately equal.

3.3 Concept of Dislocation Nodal-points

Dealing with problems containing dislocations is different from dealing with problems containing particles since dislocations are continuous lines. When the computational domain is partitioned into sub-domains, the continuity of dislocation lines must be preserved. In this section, a mathematical model for dislocations is developed such that the problem can be solved by representing dislocation lines with groups of "nodal-points". This model helps in simplifying the problem and may be solved as an N-body problems.

Parametric dislocation dynamics is developed to simulate the material behavior. Details can be found in references[3, 39, 40]. For each dislocation, the equations of motion finally turns into a linear equation array. The resulted equation arrays, in matrix forms, are like[3]:

$$\begin{bmatrix} * & * & * & 0 & 0 & 0 & 0 \\ 0 & * & * & * & 0 & 0 & 0 \\ 0 & 0 & S_1 & S_2 & S_3 & 0 & 0 \\ 0 & 0 & 0 & * & * & * & 0 \\ 0 & 0 & 0 & 0 & * & * & * \end{bmatrix} \begin{bmatrix} * \\ * \\ Q_1 \\ Q_2 \\ Q_3 \\ * \\ * \end{bmatrix} = \begin{bmatrix} * \\ * \\ F_1 \\ F_2 \\ F_3 \\ * \\ * \end{bmatrix} \tag{3.1}$$

where S_i, F_i are conceptually elements of the stiffness matrix and force matrix related to a dislocation node, which is called "nodal-points", and $Q_i = [P_x, T_x, P_y, T_y]$ are the general degrees of freedom of those "nodal-points". In these equations, the only non-zero elements are those related to dislocation nodes ("nodal-points") that are neighboring to each other. By applying the Gauss-

Jacobi or Gauss-Seidel iteration method[52], the solution of equation (3.1), i.e., the solution for an arbitrary dislocation nodal-point "2" at time step $t+1$ can be obtained through:

$$S_2 Q_2^{j+1} = F_2 - (S_1 Q_1^j + S_3 Q_3^j) \tag{3.2}$$

where j is the iteration step, and $Q_i^0 = Q_i^{(t)}$ with $Q_i^{(t)}$ as solutions for nodal-points at time step t. This equation can be solved independently for nodal-point 2 at time step $t+1$ provided that the solutions of nodal-point 1 and 3 at time step t have been obtained.

It is obvious that each dislocation node i can be considered as a virtual particle, with the attributes of connection points, glide planes, and Burger vectors in addition to that special consideration of connection between those nodal-points should be implemented. So, the implementation of the parallelization will be mostly similar the particle problem.

3.4 DD code parallelization

Based on above discussions, parallelization of the dislocation dynamics code developed at UCLA is presented in this section.

3.4.1 Tree structure in the DD code

The same concept of a hierarchical tree in N-body problems is used in solving DD problems. Based on the description in section (3.3) of nodal-points, the hierarchical tree building process is similar to those in N-body problems. The root node of the tree represents the whole domain. The process is recursively applied to each node as described below. The dislocation nodal-points in the sub-domain represented by the tree node are continuously introduced into the

tree node if the number of the nodal-points in the tree node is less than a critical value. If the number is larger than a critical value, the tree node is split into two sub-nodes and the group of nodal-points is divided to the sub-nodes according to their positions. The same process is repeated on the sub-tree node until all the dislocation nodal-points are put into the tree. The nodes of the tree, as in N-body problems, contain geometrical information of the domain. To split the domain evenly (i.e., to balance computational load between processors), the split is always in the direction which has the largest domain size. Therefore the tree is built on the basis of dislocation nodal-points. The tree structure is used to help group and distribute data, calculate multipole expansions for the interaction, and search for dislocations neighbors.

3.4.2 Domain Partitioning—The Tree Structure

To implement the parallel DD code, the computational domain, represented by a hierarchical tree data structure, must be partitioned and distributed to different processors. To partition and distribute the tree structure, three new tree conceptions are defined as follows.

1. **The Global Tree:** The global tree is the first part of the hierarchical tree. It is used to represent how the domain is split for a number of processors(Fig. 3.1). Suppose that there are n_1 processors and there are n_2 nodal-points. The critical value of the number of nodal-points in each node of the tree is set to n_1/n_2 so that the global tree will be built with n_1 leaves, corresponding to processors. Each leaf now contains a group of nodal-points and they will be distribute to different processors respectively. Each processor will have a copy of the global tree so that it will have the information of other processors, which will be used in the calculation later.

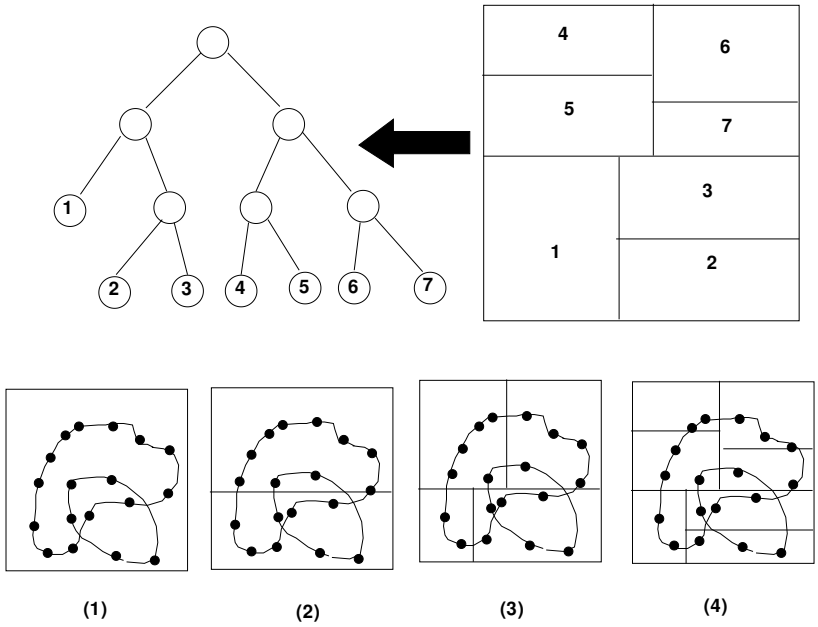

Figure 3.1: Domain decomposition to build a tree structure.

2. **The Local Tree:** The local tree is the second part of the hierarchical tree. After it has been assigned with a group of nodal-points, each processor will repeat the tree-building process on these nodal-points, by setting the critical value of the number of nodal-points in each node to 1. Thus, a local tree is built with each leaf containing only one nodal-point. The next step is to combine the local tree with the global tree by linking the local root to the specific global tree's leaf, which is corresponds to the current processor, where the local tree is built.

3. **The Ghost Tree:** In parallel computations, each processor needs to know some information from other processors, e.g., the information about the boundaries of sub-domains. Generally, parts of the data of other processors

need to be transferred to the current processor. This kind of data is called ghost data. In this algorithm, parts of the local trees on other processors are transferred. These are called ghost trees. Ghost trees are close to the current processor and contain information from other processors. They are needed to be considered as neighbors in further calculations. Ghost trees are determined by comparing the distance between local tree nodes and global leaves(excluding the one corresponding to the current processor). If the distance is smaller than a critical value, the local tree node will be considered as part of the ghost tree. After each processor receives its ghost trees from other processors, these ghost trees will be attached to the global leaves corresponding to the processor where they come from.

After the above sub-trees are constructed and combined together, each processor will have a local essential tree (Fig. 3.2), which has all the information that is required for simulation.

3.4.3 Searching for Dislocation Neighbors

After the tree structure has been built on each processor, dislocation neighbors are searched through the tree traversal process based on the Close Neighbor Criteria (CNC). This is described as follows: if any two dislocation segments represented by nodal-points are close to each other within a critical distance, these two segments are direct neighbors and their interaction will be calculated directly, otherwise their interaction will be calculated by using multipole expansions, which can be found in reference [53]. The tree traversal process is recursive and executed as follows. The process will be done for each nodal-point on the processor. For each nodal-point, the process always begins from the root tree node and it is called the current-nodal-point. If the tree node is not a leaf, i.e., it does not

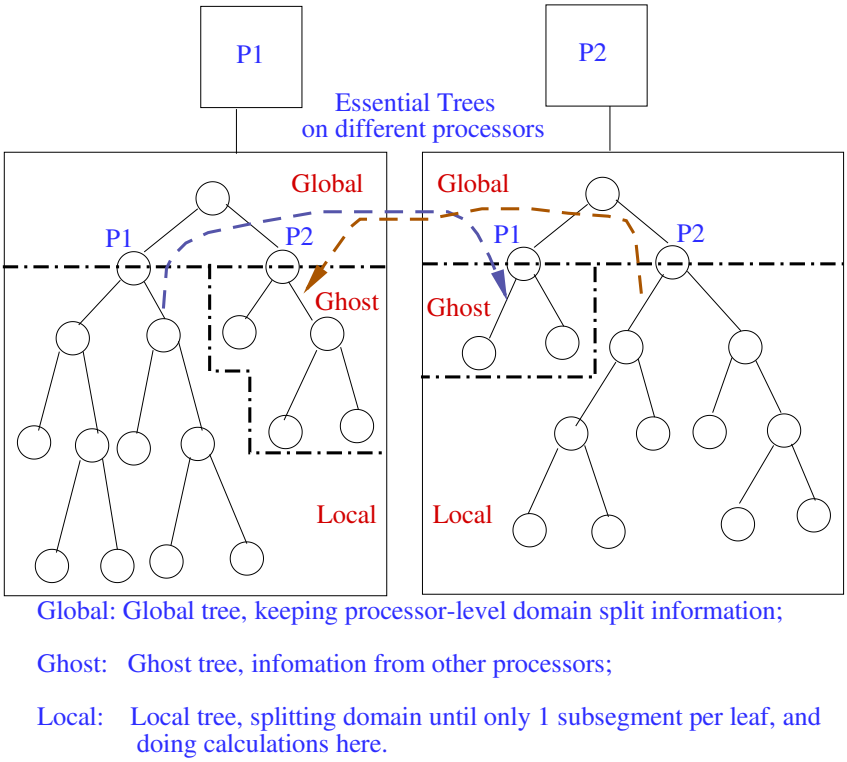

Figure 3.2: Tree structure on each processor.

contain only one nodal-point, the distance between the current-nodal-point and the tree node is evaluated. If the distance is larger than the critical distance, this tree node will be added as a multipole neighbor in the nodal-point's neighbor list and the node's children will not be visited.

If the tree node is a leaf and contains only one nodal-point, called leaf-nodal-point, the distance between the current-nodal-point and the leaf-nodal-point is evaluated. If the distance is larger than the critical distance, the tree node is added as multipole neighbor. Otherwise, the dislocation segment which contains the leaf-nodal-point is added as a direct neighbor to the current-nodal-point.

After the traversal process, dislocation neighbors will be in the lists of each nodal-point and available for calculation.

3.4.4 Updateing Tree Information

After the above operations, each processor can begin to solve for the dislocation dynamics. After the dynamics part is solved, dislocations move and their distributions in space change. Thus, the tree structure need to be rebuilt and the dislocation neighbor-lists need to be reconstructed. In this process, load balancing is also maintained. The most accurate way to update is every time step. But this will take a lot of time for communication and it may not be necessary. Thus, an update is only done every certain number of steps depending on the accuracy requirements.

3.5 Flowchart of the Parallel Code

The flow chart of the parallel code is shown in figure 3.3. The detailed list of files will be shown in the appendix.

There are totally four parts of the code, which are described as follows:

1. **Initialization:** This part is used to initialize the code to be ready to run. It reads dislocation coordinate data, material data and simulation control data from files. Variables are declared and memories are allocated. In this part, the code has the ability to begin a new simulation from the beginning or to restart a halted simulation from previous steps.

2. **Distribution of loads:** This part is the process where the tree structure is built, as discussed in previous sections. The computational loads are distributed to processors. Each processor builds an essential tree locally. Dislocation neighbor lists are constructed.

3. **Solving dislocation dynamics:** In this part, the equations of motions

of dislocations are solved. Numerical integration is performed to get the positions of dislocations.

4. **Updating:** In this part, the dislocation microstructure is updated. Mechanical properties, such as stress and strain, are calculated. The I/O operations are also performed here. All other detailed statistical information of the simulation, like the dislocation density, number of the annihilation events, is calculated here.

After the final step, the code will either stop or repeat itself until desire simulation steps are finished.

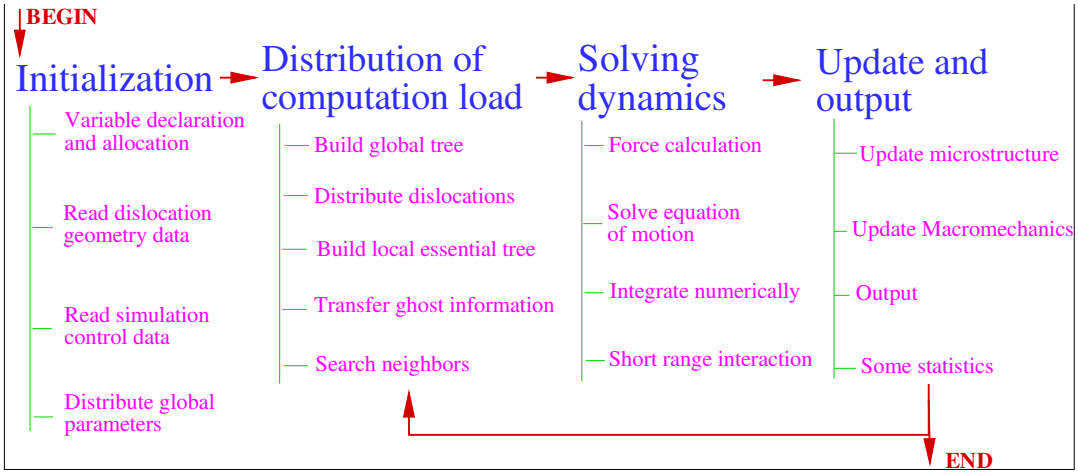

Figure 3.3: Flowchart of the parallel code.

3.6 Test Results and Discussion

The parallel code, named as UCLA-Microplasticity, was tested on the UCLA ISIS cluster. In the test cases, up to 60 nodes were used for 600 dislocations loops. Significant time speedup (speedup factor $S = \frac{t_1}{t_N}$, where t_1 and t_N are the

computation times for 1 and N processors respectively) was obtained, showing that the algorithm works well (figure 3.4).

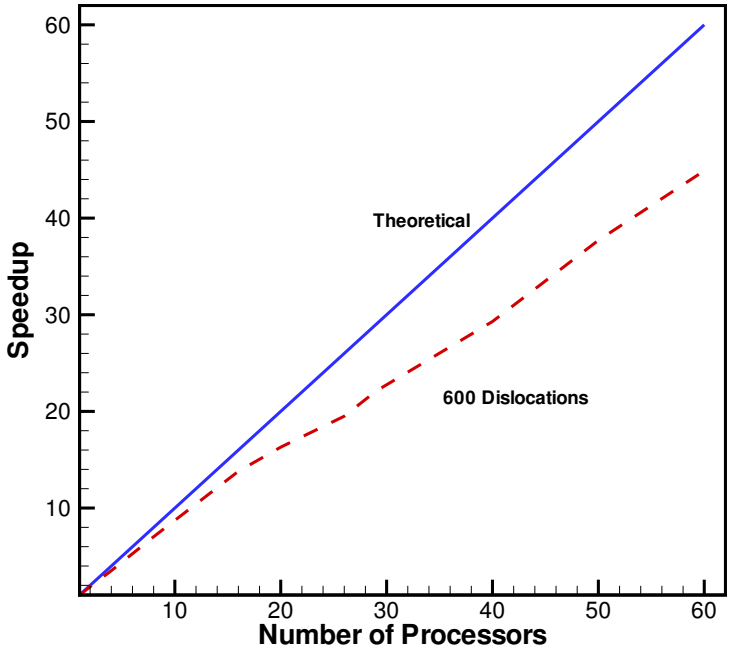

Figure 3.4: Time scaling of parallel DD code.

To study the communication efficiency, several cases were tested. For every case, each processor has the same number of degrees of freedom to be solved and the number of processors are increased. Because of communication overhead increases with the number of processors, the speedup ratio (here it is called the communication efficiency) is expected to decrease. This is seen in the test result (figure 3.5. However, it also shows that the communication efficiencies for different numbers of processors remain above 85%. This shows that heavy communication overhead has been avoided and load-balancing is well controlled.

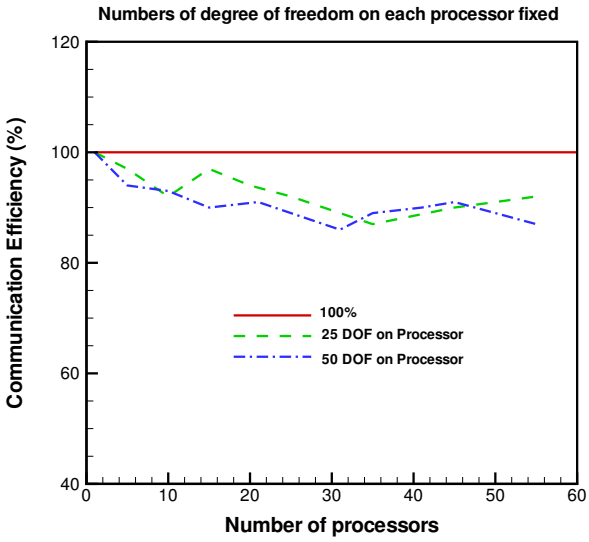

Figure 3.5: Communication efficiency of parallel code remain above 85%.

3.7 Discussion

A parallel computer code for large scale simulation of materials based on dislocation dynamics was developed. Dislocations are represented as conceptual nodal-points, which helps implementing the algorithm in a way similar to particle problems while the continuity of the dislocation lines is still maintained. A hierarchical tree data structure is designed to represent the computational domain and help the partitioning and distribution of the computational load. The code has a good performance with high speedup factors and good control of communications and load balancing.

The parallel code enhances the simulation greatly by increasing the computational efficiency. This improvement makes it a potential method to directly simulate material deformation and to study the mechanical behavior of materials and their microstructure. This will finally help improve the understanding of plasticity and design stronger materials.

CHAPTER 4

Validation of Dislocation Dynamics Simulation with Thin Film Experiments

4.1 Introduction

In Dislocation Dynamics (DD) methods, forces on individual dislocations are calculated and the motion of the dislocations computed [54]-[39]. Nevertheless, accurate description of complex 3-dimensional (3D) motion (e.g., glide, cross-slip, and climb) of dislocations requires direct experimental observation for validation of computer simulations. The lack of detailed experiments on the 3-D motion of single dislocations does not allow computer simulations direct access to experimentally-verifiable mechanisms that control dislocation configurations. Most dislocation microstructures in strained materials are highly complex, spanning many scales from the microscopic level to the polycrystalline domain. Therefore, comparison of computer simulation to such experiments can only be based on qualitative features of the microstructures.

Transmission Electron Microscopy (TEM) offers the most direct method of comparison for DD simulations. However, few such comparisons have been made to date, and these have been qualitative examinations and not quantitative comparisons between experiment and modelling [55, 56]. Comparisons of DD simulations to static TEM images are necessarily indirect and qualitative since stan-

dard TEM images are two-dimensional thin foil projections of static microstructures. Dynamic dislocation behavior in thin foils can be observed by in-situ TEM, and several interesting experimental studies have been made using this technique[57, 58]. Some 3D information about dislocation motion can be ascertained if travelling dislocations leave a slip trace on the surface. However, information on the relative positions of dislocations is largely limited to 2D results, and without 3D information on dislocation configurations, the elastic interactions between dislocations cannot be accurately determined. A technique has been developed in which 3D dislocation configurations can be quantified before and during an in-situ straining TEM experiment [59]. Although direct 3D observations of dislocation motion is not possible, knowledge of 3D configurations preceding and following deformation, along with 2D in-situ records of motion can be used to reconstruct the overall 3D behavior. Such information can also be used for direct validation of 3D DD simulations.

This chapter details a direct comparison between experimental observations and computer simulations of dislocations in thin foils. The goal is to use these comparisons to ascertain the nature of forces on dislocations and the salient mechanisms that control their motion. The effects of the constrained geometry of the foil and the free surface on dislocation motion are explored. Simplified elasticity calculations of dislocation forces and motion are not reliable to correlate with experimental data because of the complex 3D structure of observed dislocations and the influence of surface image forces. Thus, utilization of 3D computer simulations, including surface image effects is necessary.

Two effects are examined here, which are particular to dislocation behavior in thin foils. First, since dislocation loops may terminate at free surfaces, computer simulations must track the position of dislocation-free surface intersections.

Thus, special boundary conditions must be applied to the study of thin foil deformation. Second, the free surfaces of a thin foil may strongly influence dislocation behavior by introducing image stresses, which become significant when dislocations approach the surface. Strong image forces can influence dislocations by enhancing their out-of-plane motion through cross-slip and climb mechanisms.

Numerous experiments have shown that cross-slip, which is thermally activated, plays an important role during stage-III work hardening in FCC single crystals[60]-[6]. Double cross-slip results in dislocation generation by expanding new Frank-Read sources on neighboring glide planes[36]. Only segments of screw (or nearly screw) character may perform cross-slip, because they are able to move on any favorably-oriented glide plane. The probability of a dislocation segment to cross-slip onto a neighboring slip plane increases significantly when the resolved shear stress on that plane is high. Any large internal stress field, which may arise from inclusions and other obstacles to glide, surfaces, or interfaces, may induce cross-slip events.

Motion out of the glide plane can also be accomplished by climb [61, 62, 63]. At low temperatures or in the absence of a non-equilibrium concentration of point defects, dislocation motion is restricted almost entirely to glide. However, at higher temperatures or owing to a locally-high stress, an edge dislocation can move out of its slip plane by climb.

The objective of this chapter is to utilize 3D stereo-TEM in conjunction with in-situ straining TEM to describe the evolution of the spatial topology of dislocations in thin foils. DD computer simulations are used to investigate the salient mechanisms that determine experimentally-observed dislocation shapes. In doing so, the importance of image surface forces and their effects on out-of-plane dislocation motion by the cross-slip and climb mechanisms are explored. It is shown

that surface-force induced cross-slip greatly influences the structure and dynamics of the dislocation microstructure in thin foils, and that dislocation motion in thin foils may not be representative of bulk behavior.

4.2 Experimental Procedure and Results

Researchers at Los Alamos National Lab has done a series experiments to study the motion of dislocation in materials. Here, a brief review of the experimental procedure and results is given.

Stereo-TEM was used in conjunction with in-situ straining to describe the evolution of the spatial distribution of dislocations in thin Cu foils. In-situ TEM experiments are generally used to develop an understanding of bulk material properties. However, the inference of bulk material properties from thin foil in-situ observations is often controversial due to the effects of free surfaces on dislocation configurations. It is planed here to link direct experimental observations of dislocation motion and reconfiguration with computer simulations so as to discern dislocation mechanisms that are specific to thin films. Examining thin foil behavior is an advantage in that it includes surface effects, and can thus better gauge the fidelity of DD models.

TEM in-situ tensile specimens were cut, ground, and electro-polished from a well annealed copper sample. Tensile Cu foils were prepared with dimensions of 11.5 mm by 2.5 mm and a thickness of approximately 175 μm as shown in Fig. 4.1. Electrolytic polishing was used to thin the center of the specimen to perforation. The geometry of the thinned region can be approximated as two hemispherical dimples intersecting the top and bottom surfaces at 2 mm circles. Thinning produced a hole approximately 400 μm in diameter, and the specimen thickness

at the edge of the hole is generally 10-20 nm. The experimental observations were made near the top edge of the hole at a position where the sample thickness is about 200 nm.

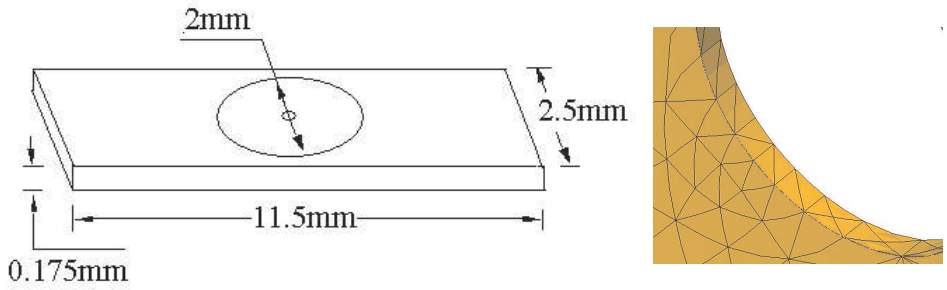

Figure 4.1: (a) The solid model of the sample, and (b) FEM mesh around the central hole.

Deformation was carried out inside the TEM using a displacement control, single tilt, straining specimen holder. During in-situ straining TEM experiments, it is advantageous to pre-strain the specimen while viewing an area of interest until some dislocation activity begins. This is primarily to ensure that dislocation motion will occur in the area of interest before spending significant time doing stereo and Burgers vector analysis. However, once the specimen is pre-strained, there is potential for the specimen to relax somewhat while analysis is being performed, and some dislocations can change position or escape the region being observed.

The stereo-coupled in-situ experiments involve obtaining a 3D description of the dislocation configuration prior to and following in-situ straining in the microscope. 3D configurations are obtained using a modified stereo-TEM technique detailed elsewhere [59]. Standard stereo-microscopy of crystalline materials is

almost never possible with a single-tilt TEM holder making it unfeasible for all commercially available in-situ straining TEM holders. The modified approach is a weak beam technique involving changing the sign of **g** (the imaging beam) and/or s_g (how far the imaging beam deviates from the exact Bragg condition) between images while tilting across a Kikuchi band that is at less than approximately 10° to the tilting direction.

The stereo pair and diffraction pattern demonstrating the modified stereo technique for the initial dislocation configuration is shown in Fig.(4.2), with the tensile axis direction vertical (same as stereo tilt axis and specimen holder axis). The positions of the dislocations are measured using a computer program that allows the user to mark points along a dislocation line with a 3D cursor while viewing micrographs stereoscopically [64]. The orientations of the tensile axis and specimen plane normal with respect to the grain are $[53(\bar{6}\bar{8})51]$ and $[(\bar{7}\bar{8})(1\bar{5})61)]$, respectively. Based on this geometry, Schmid factors for the common fcc slip systems obtained assuming a simple tension assumption are given in Table 4.1. Burgers vector analysis was performed on several key dislocations. Dislocations labeled 11, 13, and 22 in Fig. 4.2 have a Burgers vector of [101] and dislocation 12 has a Burgers vector of $[\bar{1}0\bar{1}]$.

Table 4.1: Schmid factors for Cu thin foil under simple tension.

(111)			$(11\bar{1})$		
$[01\bar{1}]$	$[10\bar{1}]$	$[1\bar{1}0]$	$[011]$	$[101]$	$[1\bar{1}0]$
0.174	0.003	0.177	0.046	0.279	0.325
$(\bar{1}11)$			$(1\bar{1}1)$		
$[01\bar{1}]$	$[101]$	$[110]$	$[011]$	$[10\bar{1}]$	$[110]$
0.339	0.296	0.043	0.119	0.014	0.105

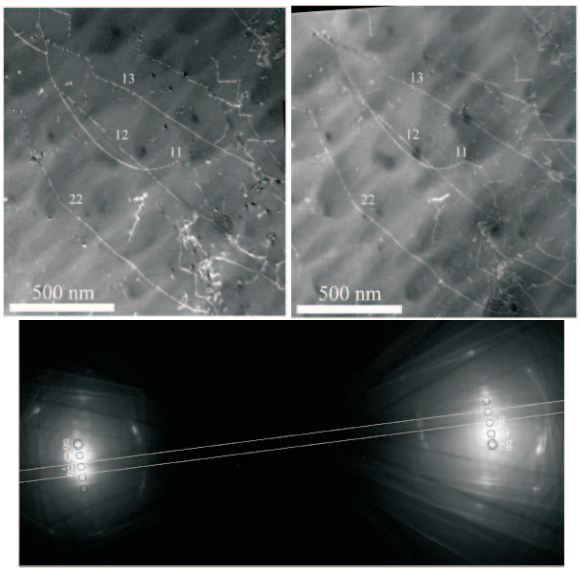

Figure 4.2: Stereo pair (top) and diffraction pattern demonstrating the modified stereo technique.

During in-situ straining, dislocation motion was monitored in the TEM at 30 frames per second. Figure 4.3 shows dislocation configurations at various times during the in-situ straining. Comparing the first frame of Fig. 4.3 with the configuration seen in Fig. 4.2, it is evident that dislocation 11 and 22 moved between the time when the stereo pair was taken and when the straining was continued and recorded. However, these two dislocations do not move during further straining. Three dimensional representations of the dislocation configuration before and after straining are given in Fig. (4.4). In the 3D representations and the DD calculations based on these configurations, the initial and final configurations of dislocation 11 are assumed to be the same, specifically the configuration given by the final stereo pair. This assumption is reasonable, since dislocations 11 and 22 do not react with one another in changing configuration, because the two dislocations have the same Burgers vector.

Dislocations 12 and 13 share the same primary glide plane, $(11\bar{1})$, and Burgers

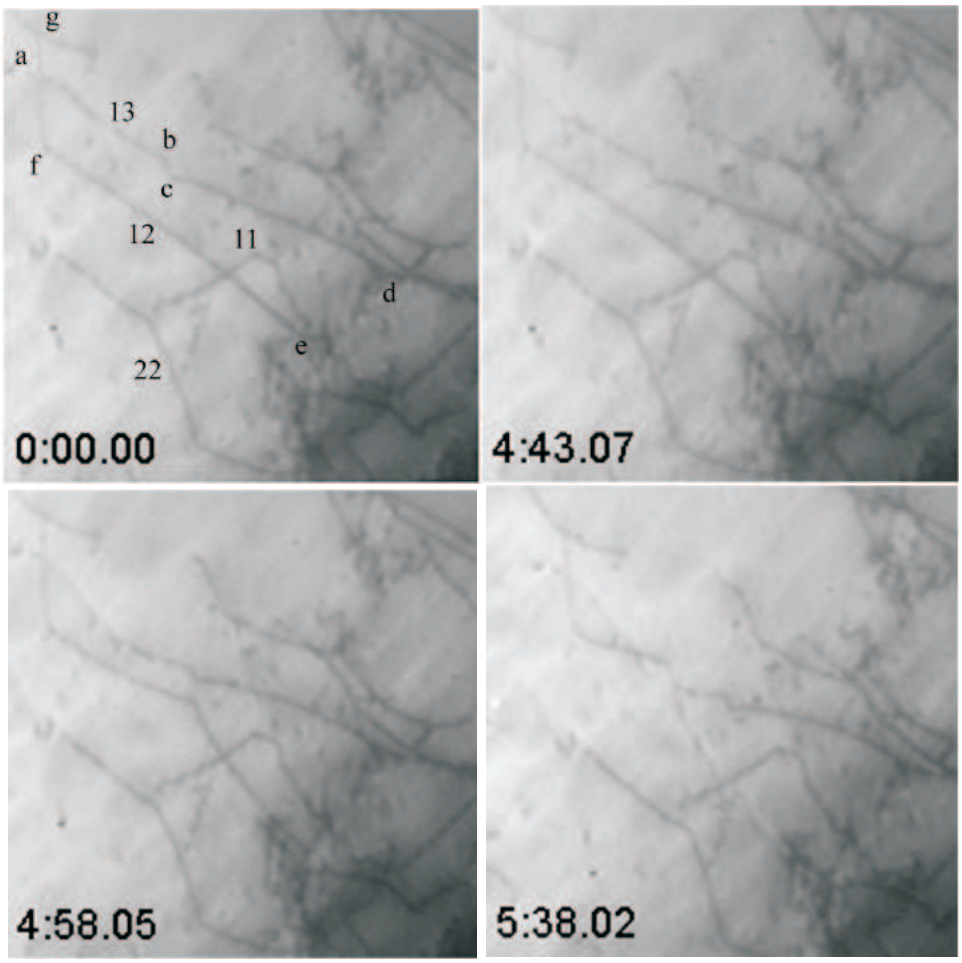

Figure 4.3: Time sequence of in-situ TEM measurements during straining. Time units are - min:sec:sec fraction

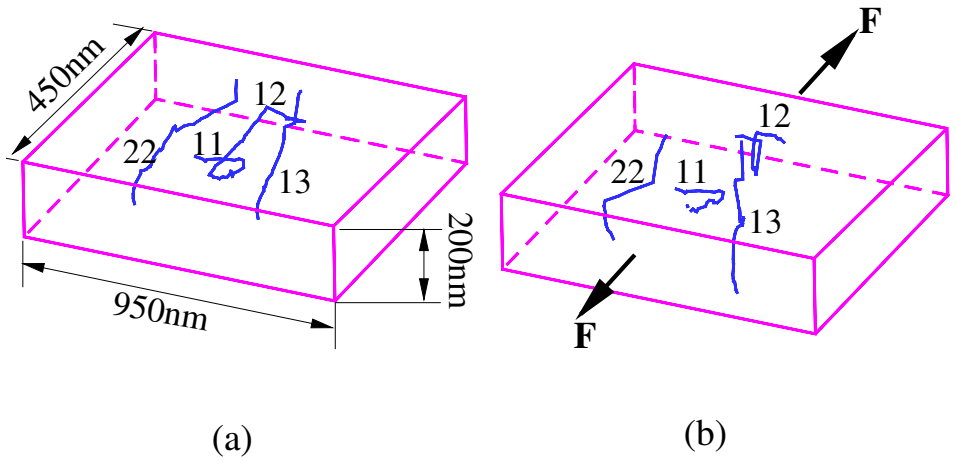

Figure 4.4: 3D rendering of experimentally-observed dislocation configurations in the Cu thin foil - (a) before deformation, and (b) after deformation.

vector but have opposite signs. Hence, they move in opposite directions. One end of dislocation 13 is pinned at a node (point labeled (d) in the first frame) while the other end terminates at the foil surface (point labeled (a) in first frame). There is a jog, labeled (bc), along the length of dislocation 13 lying on the $(\bar{1}11)$ plane. During straining, the right end remains pinned at the node and the segment (ab) glides downward in the image. Dislocation 12 starts out pinned at a different node, labeled (e). A straight segment (labeled (ef)) of dislocation 12 extends from the node diagonally across the image towards the top left corner where it jogs upwards towards the free surface (segment labeled (fg)). During straining, unlike dislocation 13, dislocation 12 escapes from the pinning point (e) (third frame) first, only to be pinned again at another node directly below the first pinning point, labeled (e) in the third frame. The result is the formation of a jog along the length of dislocation 12 as seen in frame 3. The segment (he) appears to glide

to the left, while insignificant movement of segment (hfg) was discerned up to frame 3. In frame 4-6, the segment (fh) glides upward in the image. This motion eventually leads to dislocation 12 escaping from the pinning point (e) and soon after that, a large portion of the dislocation segment (he) escapes to the surface. A key question not resolved from Fig. 4.3 is whether dislocations 12 and 13 intersect during glide (frames 4 and 5 appear to indicate a possible interaction). This is very difficult to discern from the 2D in-situ straining images, but the stereo imaging (Fig. 4.3) reveals that these dislocations do not intersect. Another question is the distance of the various dislocation segments from the free surfaces that can only be resolved from stereo imaging of the in-situ strained dislocation substructures. As shown later in this paper, having quantitative information of the dislocation positions in the in-situ straining experiment is crucial in modeling the dynamics of dislocations in thin foils.

The bowed out segment of dislocation 11 in Fig. 4.4 is not visible in the first frame of Fig. 4.3. This implies that this segment glided out to the free surface in the time between stereo imaging and the onset of further straining. Since the specimen is under strain during this time, beam heating may lead to escape of bowed out segments that are near the free surface. The remaining segments seen in Fig. 4.3 are not on the glide plane, and hence no further motion is detected.

Dislocation 22 appears as a straight line in Fig. 4.2 but kinked in the first frame of Fig. 4.3. It is possible that it experiences a similar type of motion to that described above for dislocation 12 in frames 1-3. The kinked dislocation 22 may be strongly pinned at both ends (although the details of the pinning points are not discerned clearly in these images) and hence, no further motion is detected in the in-situ straining sequence shown in Fig. 4.3. Motion of dislocations motions shown in Fig. 2 appear to be more evident for dislocations that terminate at a

free surface. The influence of surface forces on dislocation dynamics in thin films is discussed in more detail in the DD simulation section of this paper.

Based on slip trace analysis, dislocation glide has taken place on two glide planes: $(11\bar{1})$ and $(\bar{1}11)$. The resolved shear stresses for the $[101](11\bar{1})$ and $[101](\bar{1}11)$ dislocations are approximately the same, although slightly less than the highest stressed slip systems.

There is extensive discussion of the error involved in conventional and modified stereo-TEM given elsewhere [59]. The experimental error in the third dimension (z) for standard stereo-TEM depends on the stereo angle and is around an order of magnitude greater than the measurement error in the other two dimensions. With the measurement error in the x and y directions being on the order of 1nm, the measurement error in the z direction is around 10 nm. The error for the modified technique is the same as for standard stereo provided both $\mathbf{g}$ and s_g change sign but not magnitude.[59] In the present case, these ideal imaging conditions were not obtained, likely resulting in a somewhat larger error in z. These errors are to be kept in mind during the direct comparison of the modeling results to the experimental data.

4.3 Dislocation Dynamics in Thin Foils

In this chapter, Parametric Dislocation Dynamics (PDD) method developed in previous chapters is applied to simulate the motion and interaction of dislocations[3]-[38]. Additional forces are incorporated here on dislocations as a result of their interaction with the free surface. There are several models available to calculate the effects of surface forces, or to directly include the image stress field into DD simulations. These approaches include Lothe's energy theorem [35], Gosling and

Willis' Green's function method [9], and the superposition method based on solution of the Boussinesq problem [9]. For complex dislocation configurations and boundary conditions, image stresses due to surfaces and interfaces can now be computed by the finite element method (FEM) [65, 28]. In this chapter, Lothe's theorem for direct calculations of surface forces was implemented into the PDD code [39]. For an isotropic medium, Lothe [35] determined the force per unit length induced by a free surface on a straight dislocation segment [15]:

$$\mathbf{F} = \frac{\mu b^2}{4\pi\,(1-\nu)\,\lambda}\left[|(1-\nu\cos^2\beta)\tan\theta|\mathbf{n}_1 + |2\nu\cos\beta\sin\beta|\mathbf{n}_2\right] \quad , \tag{4.1}$$

where μ, ν are the material's shear modulus and Poisson's ratio, respectively. Parameters are shown in Fig. 4.5. λ is the distance from point P, where the force is evaluated, to point O at which the dislocation line intersects the free surface. $\mathbf{n}_1$ is a unit vector on the plane OO'P, with direction perpendicular to the dislocation line, $\mathbf{n}_2$ is a unit vector on the plane containing OP and the Burgers vector, with direction perpendicular to the dislocation line on the glide plane. $\mathbf{n}_1$ represents the direction of the force component, which acts to rotate the dislocation line so that it is normal to the surface, while $\mathbf{n}_2$ represents the direction of the force component, which acts to align the dislocation along its Burgers vector. The angle β is between the tangent and Burgers vectors, while θ refers to the angle between the tangent vector and the surface normal. The surface force is then decomposed to a component on the glide plane, and added to be a part of the resolved glide forces, along with those dictated by the applied stress and interaction forces. Because curved dislocation segments are employed, the tangent vector is extended to its intersection with the free surface, and EQN. (4.1) is used to compute the force per unit length at any point on the dislocation line. This force is also integrated along the parametric curves to determine the

nodal positions and coordinates, as described in reference [39].

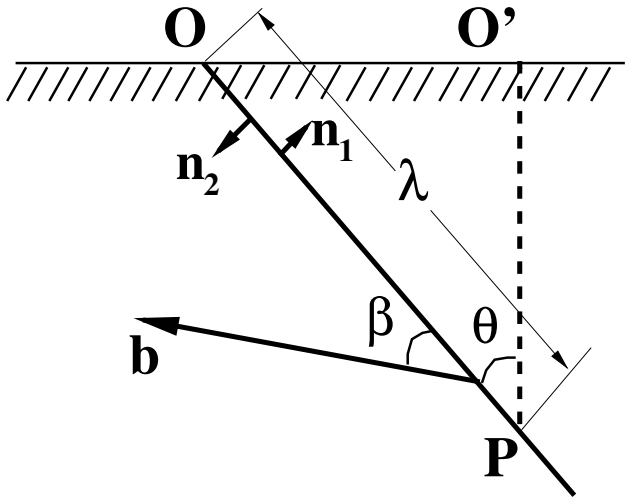

Figure 4.5: Illustration of Lothe's formula to calculate surface image force.

In the present model, dislocation loops are discretized into several curved segments that can glide on different glide planes (see Table 4.2). Internal nodes belonging to two different glide planes can only move along the intersection line of the two planes. Dislocations may end at the surface or at some joint nodes with other dislocations inside the material. Surface nodes can move along the intersection line of the glide and surface planes. Since the motion of surface nodes is associated with the creation of surface steps, the mobility of these nodes is assumed to be 20% of the bulk mobility (10^4 Pa^{-1} s^{-1})[38].

Because screw dislocation segments can move on different intersecting glide planes, cross-slip is possible [36]. In the present simulations, the orientation of various segments are checked to determine if the average tangent vector on the segment is aligned within 15° of its Burgers vector orientation. If that is the case,

Table 4.2: Nodal segment distributions on dislocations, with corresponding Burgers vectors ($\boldsymbol{b}$), glide plane Miller indices. All segments are in mixed characters.

Dislocation	Seg. 1 Miller	Seg. 1 Nodes	Seg. 2 Miller	Seg. 2 Nodes	Seg. 3 Miller	Seg. 3 Nodes	$\boldsymbol{b}$
11	jog	1-15	$(11\bar{1})$	15-16	$(\bar{1}11)$	16-29	[101]
12	$(11\bar{1})$	1-7	$(\bar{1}11)$	7-24	$(11\bar{1})$	24-41	$[\bar{1}0\bar{1}]$
13	$(11\bar{1})$	1-27	$(\bar{1}11)$	27-28	$(11\bar{1})$	28-36	[101]
22	$(11\bar{1})$	1-18	$(\bar{1}11)$	18-37	$(11\bar{1})$	37-44	[101]

another check is made on the resolved shear stress magnitude on all glide planes on which the segment may glide. Following the Friedel-Escaig mechanism[60], the probability of a cross-slip event to occur is related to the activation energy and the resolved shear stress on any glide plane as[66, 67]:

$$P = \beta \frac{L}{L_0} \frac{\delta t}{\delta t_0} \exp(V \cdot \frac{\tau - \tau_{III}}{kT}) \tag{4.2}$$

where β is a normalizing coefficient that makes the probability ranging from 0 to 1, $\tau_{III} = 32$ MPa is the critical resolved shear stress at the onset of stage III of work hardening, $V = 300\ b^3$ is the activation volume, k is Boltzmann constant, T is the temperature, $L_0 = 1\ \mu m$ and $\delta t_0 = 1$ sec are respectively references to length and time, τ is the resolved shear stress on the cross-slip plane, L is the length of the screw segment, and δt is the discrete time-step[67].

After the probabilities of cross-slip on each plane are calculated, the plane with a larger probability of cross-slip is selected for dislocation to move. When the dislocation segment approaches the free surface, the resolved shear stress on possible glide planes increases dramatically, and the probability of cross-slip is

enhanced. Further analysis of the experimental data also indicated the presence of many small jogs on dislocation lines. Such jogs can produce vacancies as they move towards the sample surface, which may result in additional out-of-plane motion due to climb of edge components as well. As a simple model of climb, comparison between the experimental and the computed dislocation structures was made and climb movement was attempted for segments that showed large differences. In summary, the simulations proceeded in the following way: (1) dislocation motion along glide planes only, (2) cross-slip motion, and (3) climb.

One uncertainty in the calculation is the stress state acting on experimentally-observed dislocations. The direction of the shear stress was determined by examining the dislocation bow out and motion. In the simulations, the applied stress was increased until the final position of the dislocations matched the experiment. A 3-D Finite Element Model (FEM) was also used to analyze the stress state in the sample. The model consisted of 7880 tetrahedral elements, corresponding to 16268 nodes. A displacement boundary condition was used, corresponding to sample straining by edge displacements in the range of (0-4) microns. A solid model for the sample is shown in Fig. 4.1. Results of the axial (normal) stress components along the tensile axis (y-direction) and along its perpendicular (x-direction) are shown in Fig. (4.6). Also shown in Fig. 4.7 is the corresponding normal stress contour around the central perforation. Although large stress gradients are observed near the central hole region, the zone where dislocations are observed extend over a relatively small length (microns), and the axial stress level is estimated to be 150 MPa for the full 4 μm displacement. It is also found that the shear stress component in this zone is negligible, confirming that tensile stress state in our DD model is close to the correct value.

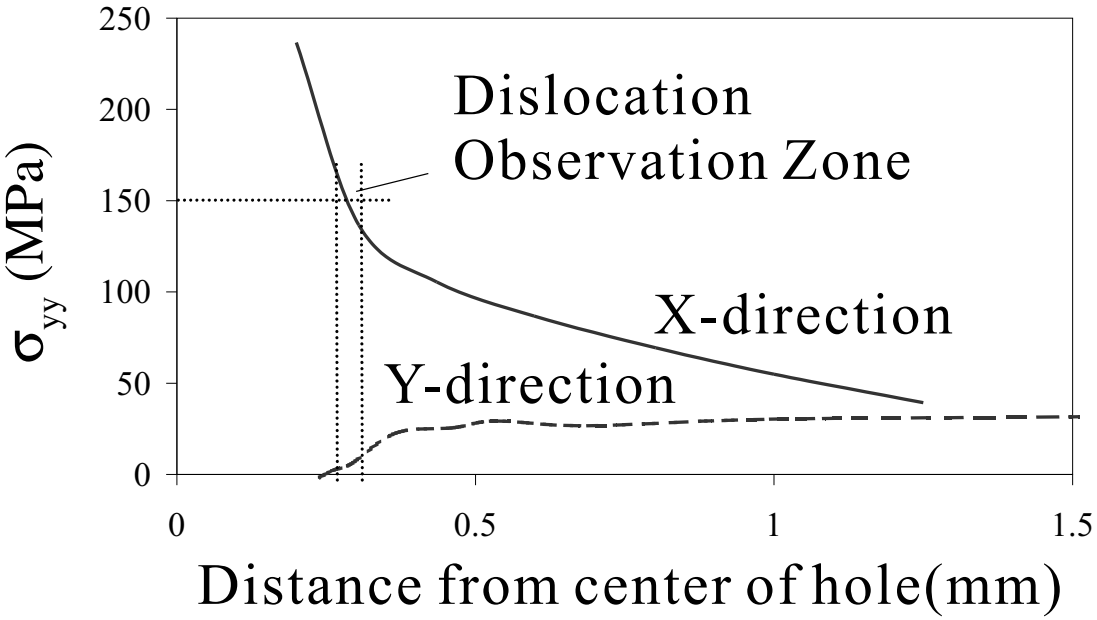

Figure 4.6: FEM results for normal stress distribution in the sample along the axial direction (y) and its normal (x).

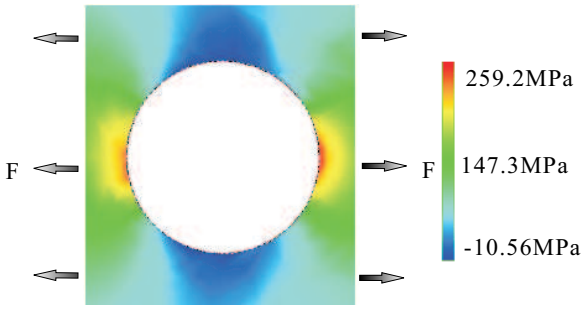

Figure 4.7: FEM results for σ_{yy} contour around the central hole.

4.4 PDD Simulations for Experimental Analysis

Initial PDD computer simulations of the experimental data restricted the motion of dislocations to movement on the glide plane. The initial results indicated that while the experimental dislocation motion on the glide planes is matched reasonably well in the simulations, motion in the direction normal to the TEM observation plane is greatly underestimated by the simulations. To be more concrete, with no climb or cross-slip mechanisms invoked, the difference between the simulations and experiments for dislocation 11 is approximately 16 nm within the observation plane and 12 nm out-of-plane, roughly within the experimental uncertainty. The other dislocations were less well determined, with a difference in dislocations 22 and 13 within the observation plane of approximately 61 nm and an out-of-plane error of 80 nm. The motion of dislocation 12 is even more poorly modeled, with an in-plane difference of 200 nm and an out-of-plane error of 140 nm.

PDD simulations that include dislocation cross-slip and climb (using the methods described above) were thus performed. These simulation results are shown in Fig. (4.8) and are compared with experimental observations of Figs. (4.2) and (4.4). The results show that dislocation 22 undergoes cross-slip motion, dislocation 13 climbs, and dislocation 12 shows both climb and cross-slip motion. Details of the cross-slip mechanism of dislocation 22 are shown in Fig. (4.9), where it is seen that the segment reconfigures from the original slip plane to the neighboring one with a higher probability of cross-slip motion. The cross-slip probabilities of two screw segments are listed in table (4.3). It is obvious that cross-slip planes have larger probabilities. Although cross-slip does not have to happen on cross-slip plane, the dislocation segment will select the plane that has large a larger probability.

Table 4.3: Probabilities of cross-slip of screw segments at an applied stresses of 100 MPa

Segment on Dislocation	Original Plane	Cross-slip Plane
segment 2 on Dislocation 12	P=0.44	P=1.0
segment 2 on Dislocation 22	P<0.01	P=0.63

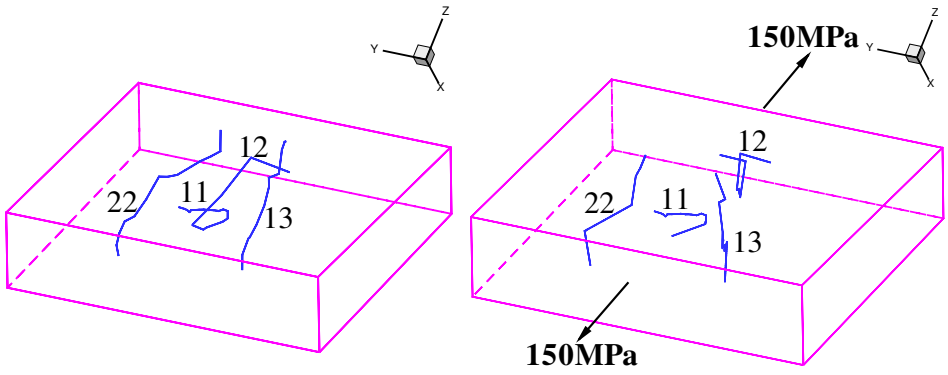

Figure 4.8: Initial and final dislocation configurations simulated by PDD

Image stresses play an important role in activating the cross-slip by changing the resolved shear stress on the cross-slip planes. For example, when cross-slip occurs, for dislocation 12, the resolved shear stresses resulting from image forces on the cross-slip plane$(11\bar{1})$ and on the original plane $(\bar{1}11)$ are 37.76 MPa and 20.15 MPa, respectively. The resolved shear stresses resulting from applied stress on the cross-slip plane and the original plane are 46.22 MPa and 48.18 MPa, respectively. The cross-slip plane has even a lower stress without the image effect. The average final resolved shear stresses on the cross-slip plane and the original plane are 81.98 MPa and 60.07 MPa, which shows that surface image forces greatly increase the cross-slip probability on the cross-slip plane. For climb, the

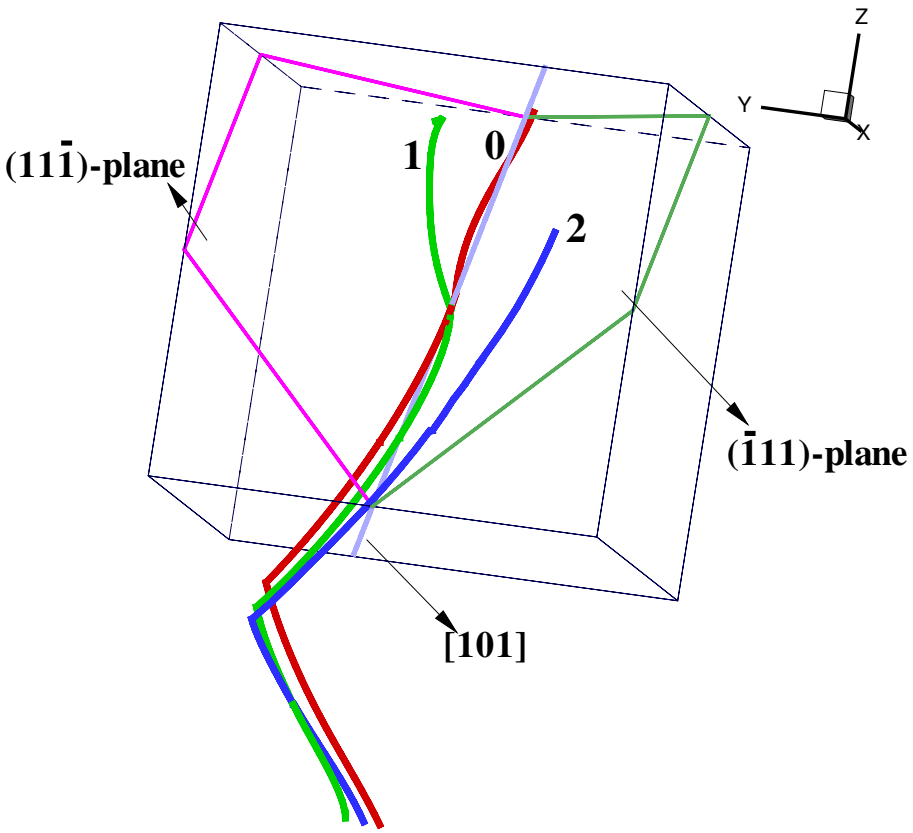

Figure 4.9: Dislocation 22 positions during cross-slip motion: (1) Final configuration without cross-slip, (2) Final configuration with cross-slip

climb stresses on dislocation 12 and 13 are calculated as 208.3 MPa and 294.3 MPa at the end of straining, respectively. It is believed that these high stresses can lead to pipe diffusion that results in dislocation climb[62, 63]. Careful analysis of node coordinates of the simulated and experimental configurations shows great reduction in the positional difference when cross-slip and climb motion are included, with the largest difference for any of the dislocations of about 13 nm in-plane and 17 nm out-of-plane. These uncertainties are well within experimental error.

4.5 Discussion

Direct validation of DD simulations with experiments (in situ straining coupled with 3D imaging in TEM) allowed to correctly model the motion of dislocations in thin, annealed Cu foils with a low initial dislocation density where surface image forces play a significant role in determining the dislocation dynamics. It is shown, through systematic comparison between experimental observations and PDD simulations, that dislocation configurations in thin copper foils acquire considerable 3-dimensional components that cannot be explained by glide events alone. The structure of dislocation lines is highly jogged, with non-planar components. Surface image forces in the thin copper foil appear to have two main effects: (1) they result in the inducement of cross-slip for screw components; (2) they also nucleate jogs on dislocation lines. Possibly through vacancy flow from the surface, the motion of these jogs may also result in additional out of plane displacement of edge dislocation segments as well.

CHAPTER 5

Computer Simulation of Single Crystal Plasticity

5.1 Introduction

The connection between the microstructure of materials at micron and submicron scale has been well-established. Recently, there has been a surge in attempts to derive the mechanical response of metals starting from its dislocation microstructure. Such microstructures could be very heterogeneous with dislocation cells, tangles, and slip bands. The collective and individual behavior of dislocations is very critical in determining the mechanical properties. Dislocation motion and the processes by which they form different microstructures under various loading conditions is important in understanding the physics of strength and failure of materials. Because of the intrinsic complexity of microstructures, such understanding is still a open problem and can not be solved by experiments and analytical theories alone. Direct numerical simulation of dislocation motion provides an alternative way to effectively study the relation between the microstructure and macroscale properties, and to improve the understanding of deformation behavior of materials. This will eventually help in designing new engineering materials that are much stronger than those currently in use in many modern industries, such as aerospace, semiconductor and automotive industry.

In this chapter, the UCLA-MICROPLASTICITY dislocation dynamics computer code is applied to study the work-hardening of single crystal copper. Dislocation microstructure of deformed copper was simulated and corresponding stress-strain curves of the crystal were obtained from the simulation.

5.2 Simulation Procedure

A uniaxial tensile stress is applied to simulate the deformation of bulk materials. The stress is applied at a constant strain rate in the direction of [100]. Define

$$c = \dot{\epsilon}_{11} = \dot{\epsilon^e}_{11} + \dot{\epsilon^p}_{11} \tag{5.1}$$

as the applied strain rate, where $\dot{\epsilon^e}_{11}$ is an element of the elastic strain rate tensor $\dot{\boldsymbol{\epsilon}}^e$ and $\dot{\epsilon^e}_{11}$ an element of the plastic strain rate tensor $\dot{\boldsymbol{\epsilon}}^p$. The plastic strain rate tensor is obtained from the motion of dislocations as

$$\dot{\boldsymbol{\epsilon}}^p = -\frac{1}{2V}\sum_{i=1}^{N}\oint_0^{l^{(i)}} v^{(i)}(\mathbf{p})[\mathbf{n}^{(i)}(\mathbf{p})\otimes\mathbf{b}^{(i)} + \mathbf{b}^{(i)}\otimes\mathbf{n}^{(i)}(\mathbf{p})]dl \tag{5.2}$$

where N is total number of dislocation loops, $l^{(i)}$ is the length of dislocation i, V is the volume of the simulated material, $\mathbf{n}$ is a unit vector defined as $\mathbf{v}\times\xi$, $\mathbf{v}$ and ξ are the velocity vector and the tangent vector of the dislocation loop at point $\mathbf{p}$ on dislocation lines, respectively.

The elastic strain rate in [100] direction is defined as:

$$\dot{\epsilon^e}_{11} = \frac{\dot{\sigma}_{11}}{E} \tag{5.3}$$

where E is Young's modules and $\boldsymbol{\sigma}$ the stress tensor.

Substituting Eq. 5.2 and 5.3 into Eq. 5.1, the expression for the relation between the measured stress and applied strain rate is obtained as

$$\dot{\sigma}_{11} = E(c - \dot{\epsilon^p}_{11}) \tag{5.4}$$

Because of $\dot{\sigma}_{11} = \frac{\sigma_{11}^{t+1} - \sigma_{11}^{t}}{\delta t}$, Eq. 5.4 leads to

$$\sigma_{11}^{t+1} = \sigma_{11}^{t} + E\delta t(c - \dot{\epsilon}_{11}^{p}) \tag{5.5}$$

where δt is the time step used in the simulation.

Substituting the plastic strain rate from Eq. 5.2 into Eq. 5.5, the stress-strain curves (σ_{11} vs ϵ_{11}) can be calculated. The simulations directly relate the dislocation motion at the microscale to the macroscale mechanical properties.

5.3 Geometric Generation of The Initial Dislocation Microstructure

In dislocation dynamics simulations, an important factor affecting the accuracy and efficiency is that dislocation micro-structures are properly represented, especially in 3D. A method has been developed to generate initial dislocation microstructures in a material representative volume (MRV) automatically for any dislocation density. The generated microstructure is then used as an initial input of the simulation.

The dislocation density is generally expressed in the form of the total length of dislocations in a unit volume of material, in units of cm/cm^3 or m/m^3, i.e., cm^{-2} or m^{-2}. The average length of a dislocation segment is written as $1/\sqrt{\rho}$. And this is also the average distance between dislocations.

In this method, a dislocation loop is composed of two parts: super-jogs and Frank-Read sources (Fig. 5.1). Super-jogs are not on the glide plane so that they will not be able to glide. Frank-read sources are on glide planes and then can glide on these planes. Glide planes are first generated in the MRV. On these glide planes, dislocations loops are generated. If they cross the volume boundary,

these loops are mapped back to the volume according to their position at the opposite side. This method is called Periodic Boundary Condition (PBC), which is commonly used for bulk material simulations. In this case, the central cube is called a representative material cube and all the simulations are inside it. At the same time as the microstructure is generated, the corresponding data that is needed in the following dynamics simulation as input are written to files.

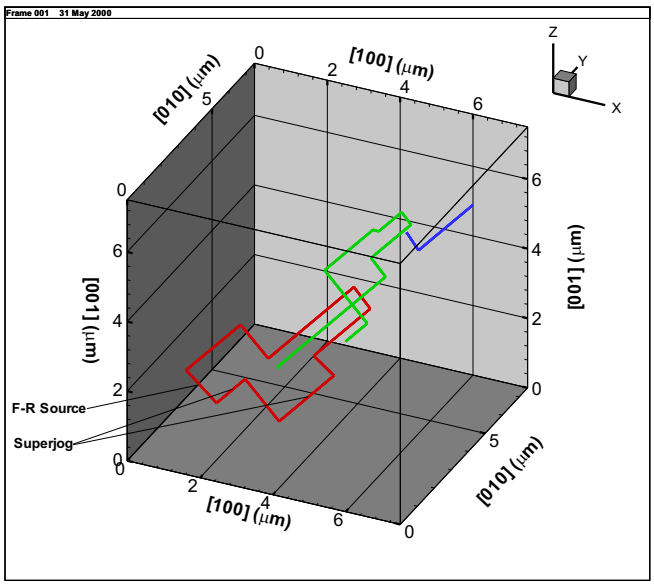

Figure 5.1: Dislocation loop composed of F-R source and super-jog. Periodic boundary conditions are applied.

The only input of this generation code are the cube length and the dislocation density. Once it receives the two parameters, it will automatically generate the dislocation micro-structure. The generation is loop by loop, after each loop is generated, the dislocation density is checked. The process is continued until the generated density is equal to the desired density.

Figure 5.2 shows the microstructure in 3D. In figure 5.3, a 2D cross section of the microstructure along the indicated plane is shown. The dimensions of the

volume are $2\mu m \times 2\mu m \times 2\mu m$, the dislocation density here is $10^{10} cm^{-2}$, and the number of dislocation loops is 1356.

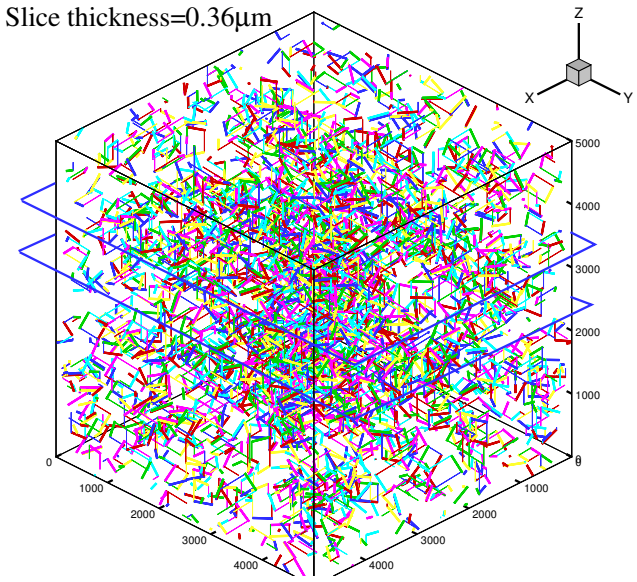

Figure 5.2: Dislocation microstructure in a $2\mu m \times 2\mu m \times 2\mu m$ with density as $1 \times 10^{10} cm^{-2}$. Thick lines are FR sources and thin lines are super-jogs. Two cross-section cutting planes are shown.

5.4 Simulation Results

Several simulations are performed on different cases to study the single crystal plasticity of FCC Cu, especially to obtain the dislocation microstructure evolution during deformation and the stress-strain curves. In simulations, the following material parameters for Cu are used: the lattice constant $a = 0.3615 \times 10^{-9} m$, the shear modulus $\mu = 50\ GPa$, the Possion ratio $\nu = 0.31$, the Young's modulus $E = 131\ GPa$, and a dislocation mobility $m = 10^4\ Pa^{-1} s^{-1}$.

At the same time, the three simulations are specially designed to study the effect of the sizes of simulation volumes (case 1 and case 2 have the same initial

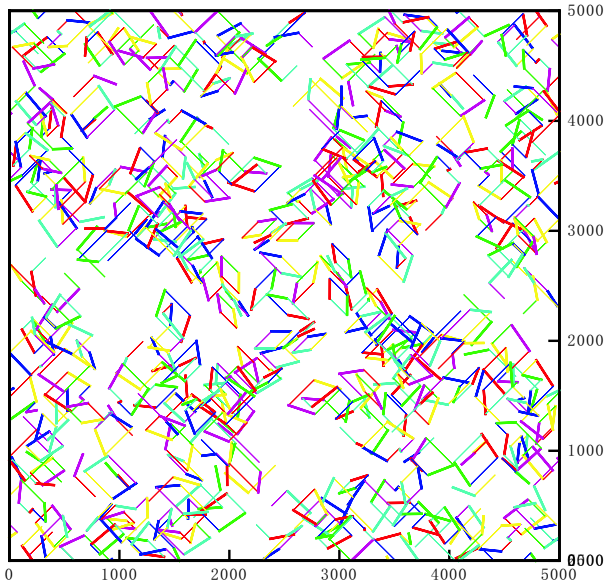

Figure 5.3: A cross-sectional slice view of dislocation microstructure shown in figure 5.2

dislocation density but different sizes of the simulation volumes) and the effect of different dislocation densities (case 3 has a higher density than case 2) on the mechanical behavior.

5.4.1 Case 1: 5 Micron Crystal with Low Initial Density

In this case, the simulation volume is $5\mu m \times 5\mu m \times 5\mu m$, and the initial dislocation density is $1 \times 10^7 cm/cm^3$. The applied constant strain rate is $100s^{-1}$. The simulated stress-strain curve and dislocation density-strain curve are shown in figures 5.4, the simulated strain is up to 0.4%; and the dislocation density reaches $1.4 \times 10^9 cm/cm^3$. Microstructures at different strain levels are shown in figures 5.5 to 5.8. The significant hardening of the stress-strain curve results from small volume effects on dislocation annihilations and interactions.

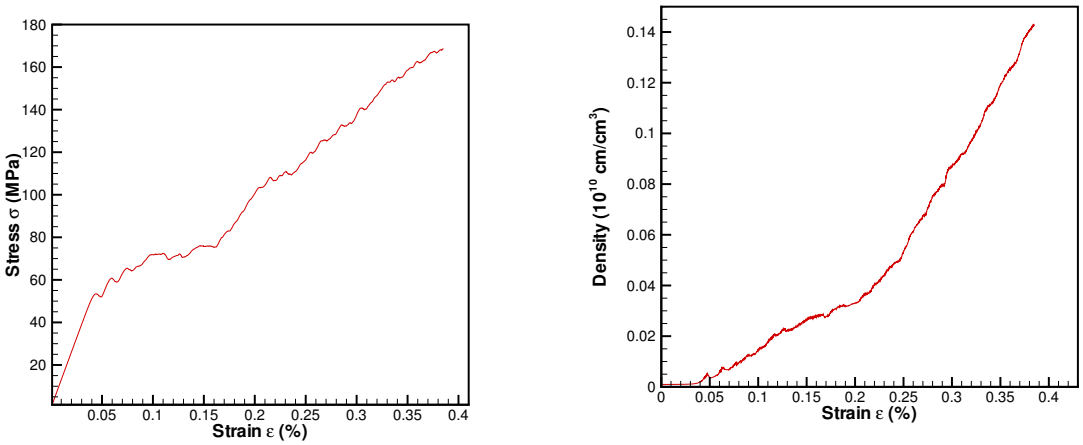

(a) (b)

Figure 5.4: (a) The simulated strain-stress curve; (b) Dislocation density vs strain.(Case 1)

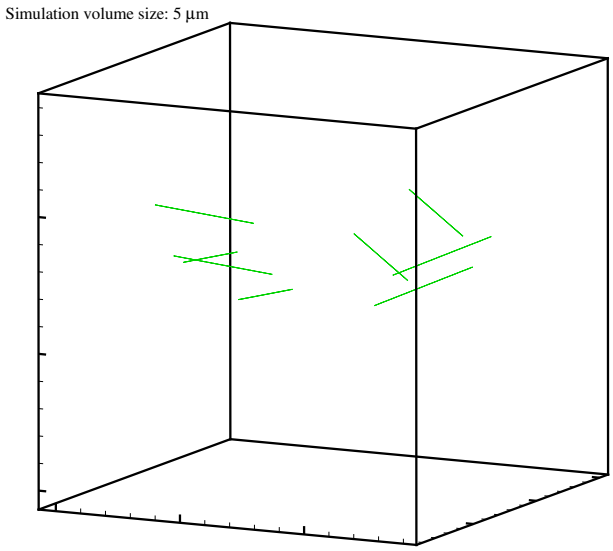

Figure 5.5: (a) Initial simulation microstructure(Case 1, $5\mu m \times 5\mu m \times 5\mu m$)

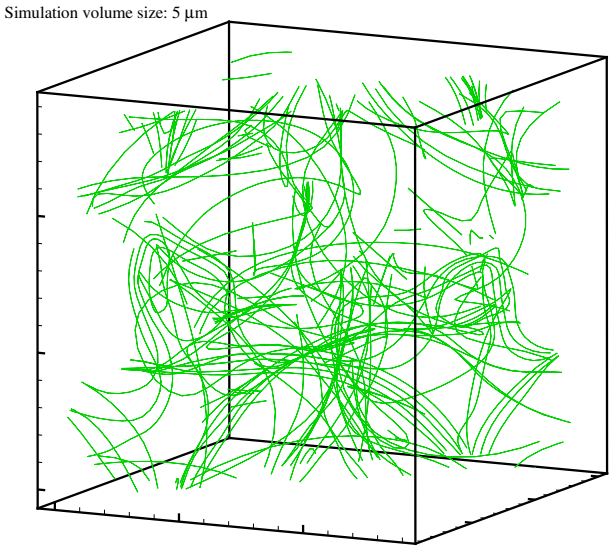

Figure 5.6: Simulated microstructure at strain of 0.15%(Case 1, volume size $5\mu m \times 5\mu m \times 5\mu m$).

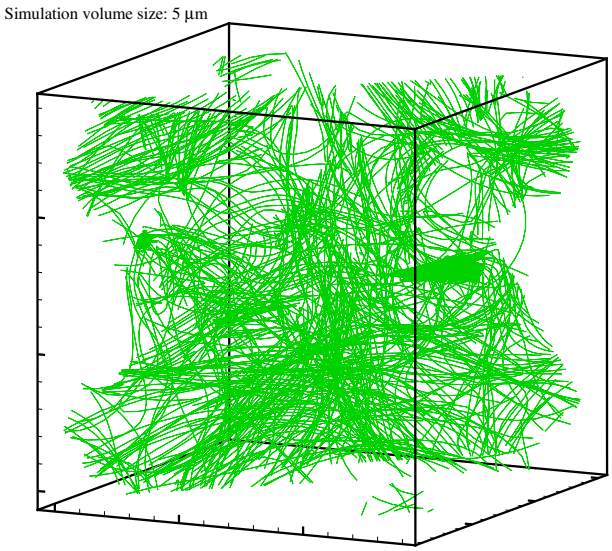

Figure 5.7: Simulated microstructure at strain of 0.4% (Case 1, volume size $5\mu m \times 5\mu m \times 5\mu m$)

Figure 5.8: (111) slice view of the simulated microstructure at strain 0.4%(Case 1, volume size $5\mu m \times 5\mu m \times 5\mu m$)

5.4.2 Case 2: 10 Micron Crystal with Low Initial Density

In this case, the simulation volume is $10\mu m \times 10\mu m \times 10\mu m$, and the initial dislocation density is $1 \times 10^7 cm/cm^3$. The applied constant strain rate is $100s^{-1}$. The simulated stress-strain curve and density-strain curve are shown in figures 5.9, the simulated strain is up to 0.3% and dislocation density reaches $8 \times 10^8 cm/cm^3$. The initial microstructure and the ones for increasing strain levels up to 0.3% are shown in figures 5.10 to 5.13.

5.4.3 Case 3: 5 Micron Crystal with High Initial Density

In this case, the simulation volume is $5\mu m \times 5\mu m \times 5\mu m$, and the initial dislocation density is $1 \times 10^9 cm/cm^3$. The applied constant strain rate is $100s^{-1}$. The stress-strain curve and the density-strain curve are shown in figures 5.14 and 5.15. The initial microstructure and those for increased strain levels up to 0.3% are shown

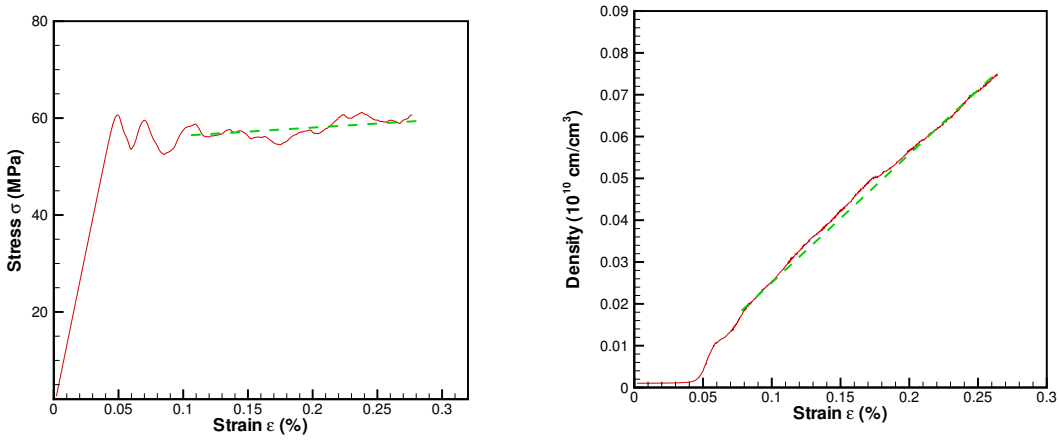

(a) (b)

Figure 5.9: (a) Simulated strain-stress relation; (b) Dislocation density and strain relation.(Case 2, volume size $10\mu m \times 10\mu m \times 10\mu m$)

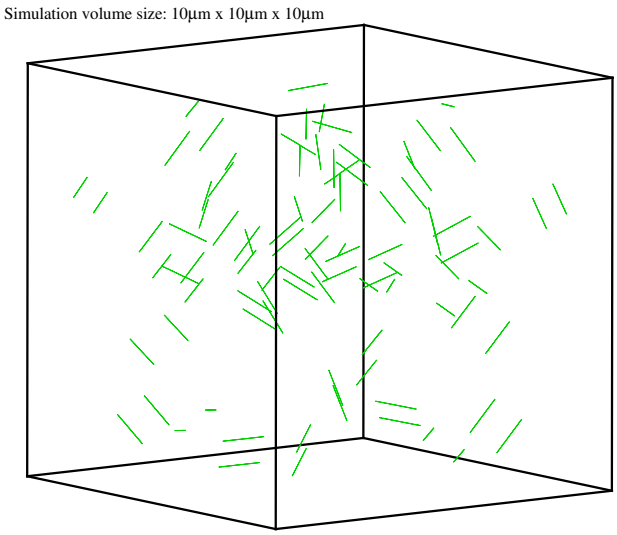

Figure 5.10: Initial simulated microstructure.(Case 2, volume size $10\mu m \times 10\mu m \times 10\mu m$)

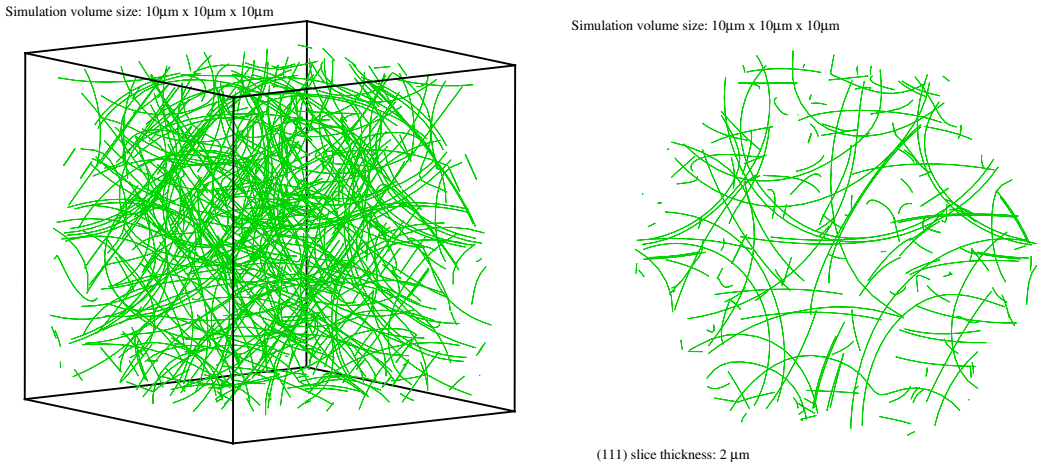

Figure 5.11: (a) Simulated microstructure at stain of 0.1%, (b) (111) slice view of the microstructure.(Case 2,volume size $10\mu m \times 10\mu m \times 10\mu m$)

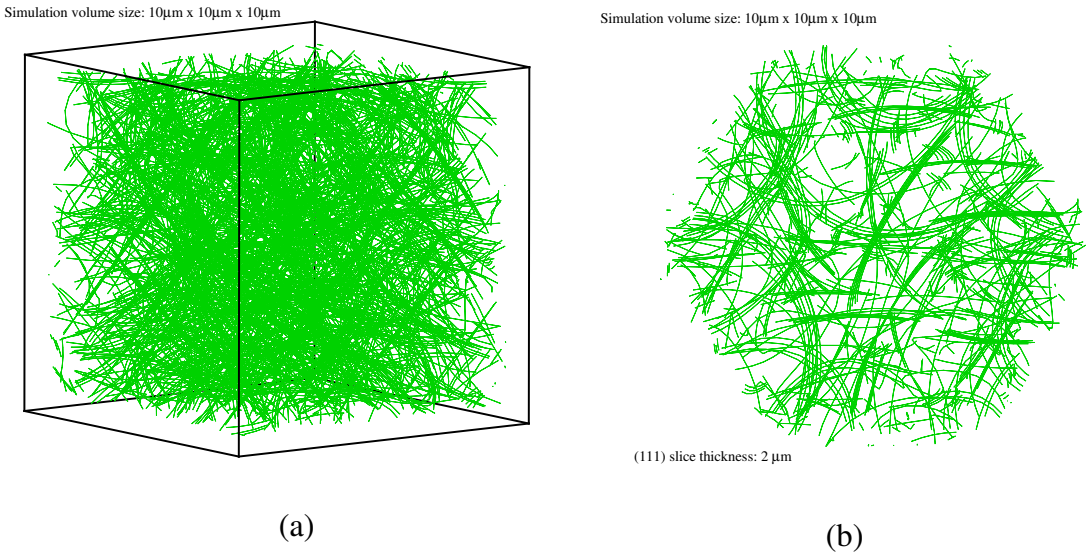

Figure 5.12: (a) Simulated microstructure at strain of 0.2%, (b) (111) slice view of the microstructure (Case 2, volume size $10\mu m \times 10\mu m \times 10\mu m$)

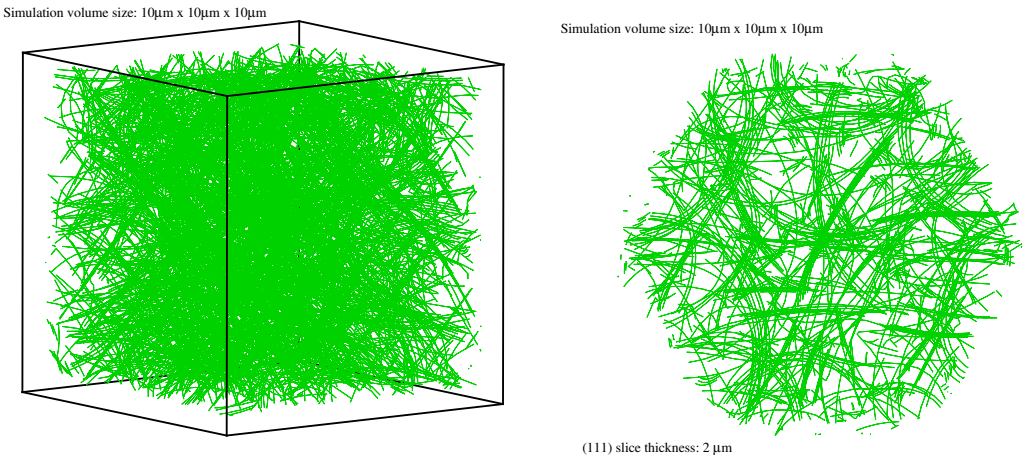

Figure 5.13: (a) Simulated microstructure at strain of 0.3%, (b) (111) slice view of the microstructure (Case 2, $10\mu m \times 10\mu m \times 10\mu m$)

in figures 5.16 to 5.20.

5.5 Discussion

5.5.1 General observations

In general, with increasing strain, dislocations rearrange into different microstructures like dislocation tangles, dislocation slip bands and cell structures. These microstructures interact with dislocations and the strain-stress curves reflect these underlying interaction between defects. The interactions between dislocations lead to the formation of different patterns.

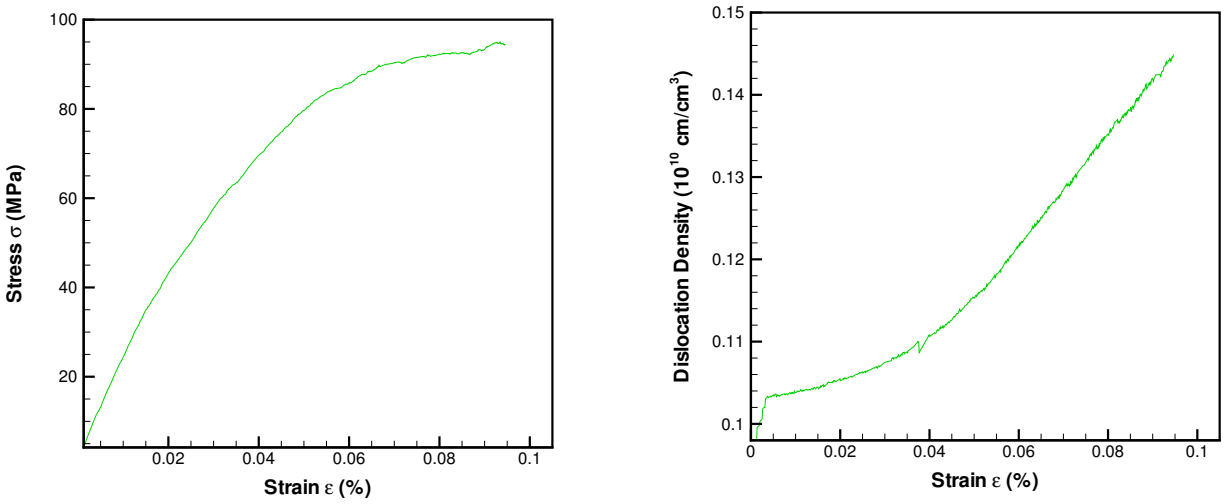

Figure 5.14: (a) The simulated strain-stress curve; (b) dislocation density vs strain. (Case 3, volume size $5\mu m \times 5\mu m \times 5\mu m$)

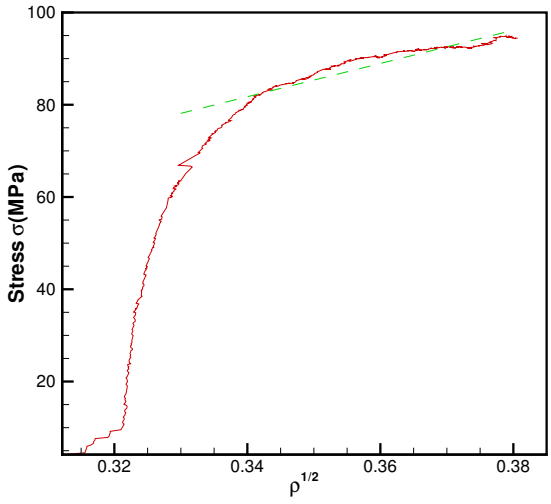

Figure 5.15: Relation of stress to the square-root of the dislocation density, the dashed line is the linear fit from least-square method.(Case 3, volume size $5\mu m \times 5\mu m \times 5\mu m$)

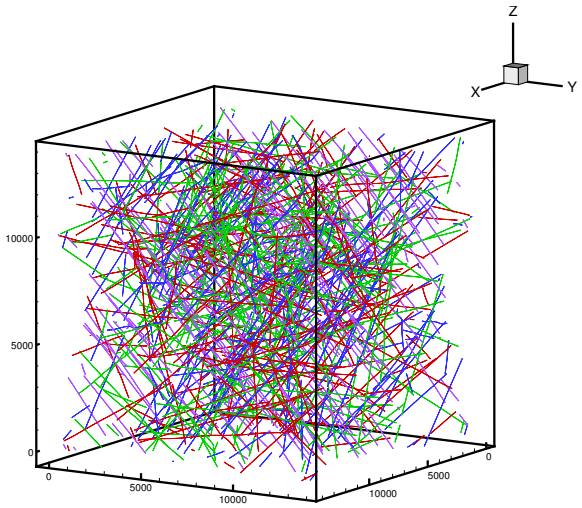

Figure 5.16: Initial simulated microstructure.(Case 3, volume size $5\mu m \times 5\mu m \times 5\mu m$)

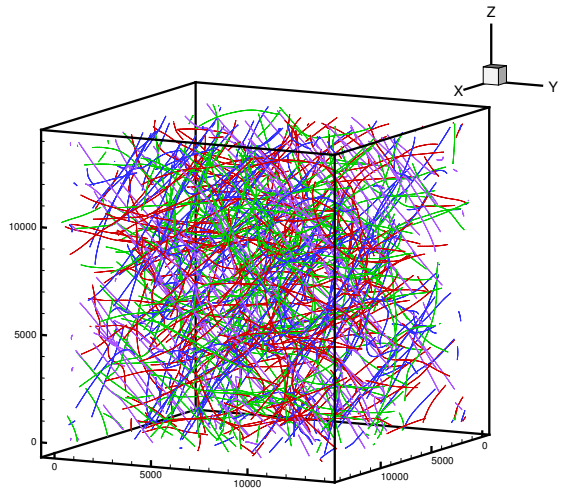

Figure 5.17: Simulated microstructure at strain of 0.03%.(Case 3, volume size $5\mu m \times 5\mu m \times 5\mu m$)

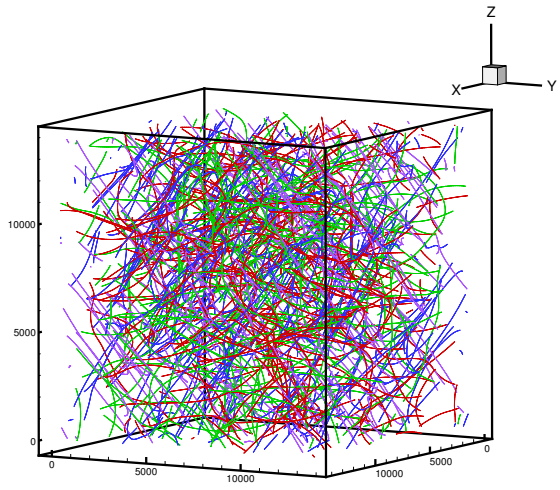

Figure 5.18: Simulated microstructure at strain of 0.06%.(Case 3, volume size $5\mu m \times 5\mu m \times 5\mu m$)

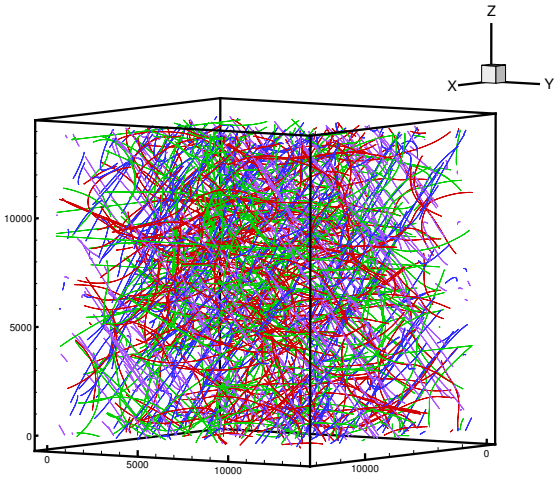

Figure 5.19: Simulated microstructure at strain of 0.1%.(Case 3, volume size $5\mu m \times 5\mu m \times 5\mu m$)

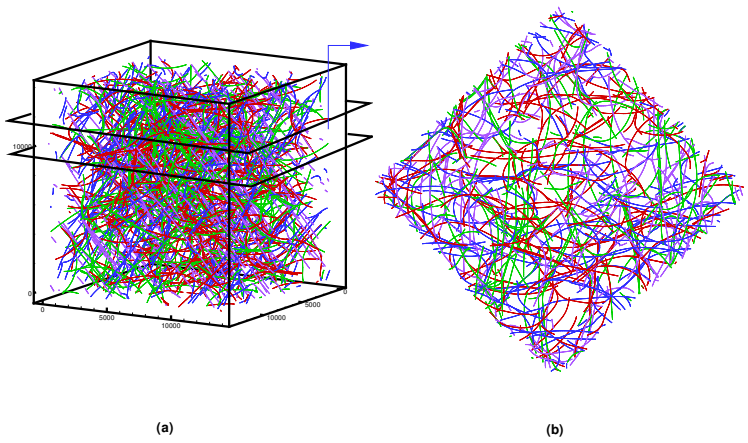

Figure 5.20: Dislocations form into complex microstructures, strain at 0.1%.(Case 3, volume size $5\mu m \times 5\mu m \times 5\mu m$)

5.5.2 Dislocation density

In all cases, dislocation densities are initially low and the deformation is primarily due to the glide on each individual slip system. After the dislocation density builds up to a larger strain, dislocation interactions tend to play a more significant role in the formation of microstructure patterns. It should be noted that a more vivid dislocation microstructure pattern is observed in case 3 (volume size $5\mu m \times 5\mu m \times 5\mu m$ with the high initial dislocation density $1 \times 10^9 cm/cm^3$) than the other cases with a low initial density.

Beyond a strain of 0.05%, dislocation density ρ has a linear relation to the strain. Initially, this linear relation can be expressed as $\frac{d\rho}{d\epsilon} = 0.2 \sim 0.3 \times 10^{10} cm/cm^3$, which is calculated from case 1 and case 2. When the dislocation density is higher (case 1 after a strain of 0.3%, or case 3), this linear relation is calculated to be $\frac{d\rho}{d\epsilon} \doteq 0.68 \times 10^{10} cm/cm^3$.

5.5.3 Stress-strain curves

The stress-strain curves are closely related to and are a direct result of dislocation motions and interactions. All stress-strain curves present a linear elastic region in the beginning of the deformation. When the dislocation density begins to increase linearly with strain, plastic strain from dislocation motion also increases which causes the stress-strain curve deviating from the elastic regime to the plastic regime. The underlying dislocation motion and interactions affect the plastic strain and are reflected by the stress-strain curves.

After transition from the elastic region to the plastic region, stress-strain curves continue to develop with a specific hardening rate $\frac{d\sigma}{d\epsilon}$. For case 1, the hardening rate is about 2500 MPa, which is high and due to the effect of small simulation volume. For case 2 and case 3, the hardening rates are about $1330MPa \approx \frac{\mu}{30}$ and 2432 $MPa \approx \frac{\mu}{20}$, respectively. The higher yielding stress and hardening rate in case 3 are believed to due to more interaction between dislocations for the higher dislocation density in the simulation volume.

The experimental hardening rate for different hardening stages are usually expressed as $\theta = \frac{\delta\tau}{\delta\gamma}$, with τ as the resolved shear stress and γ the resolved shear strain for a single slip. For stage II, θ has a value of $\frac{\mu}{300} \sim \frac{\mu}{200}$. To compare the simulation results of multislip to experimental results, a simple analysis is made as follows to illustrate the translation of the experimental shear hardening rate $\frac{\delta\tau}{\delta\gamma}$ to simulated tensile hardening rate $\frac{d\sigma}{d\epsilon}$.

In figure 5.21 (a), a specimen under applied force F has plastic deformation along the slip direction. The resolved shear stress for this plastic deformation can be calculated as:

$$\tau = \frac{F\cos\lambda}{A/\cos\phi} = \frac{F}{A}\cos\lambda\cos\phi = \sigma\cos\lambda\cos\phi \tag{5.6}$$

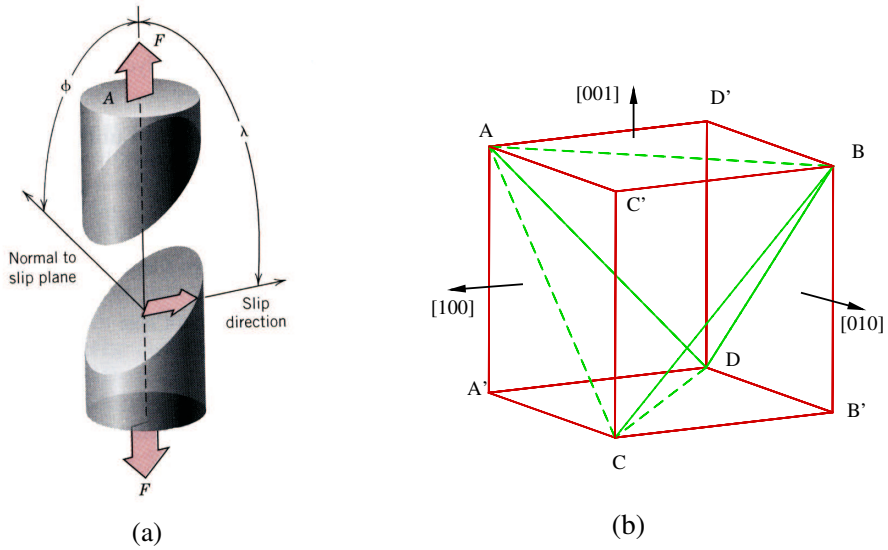

Figure 5.21: (a). Calculation of resolved shear stress, (b). Slip planes form a tetrahedra ABCD in FCC crystals.

where A is the area under the force F, λ is the angle between the slip direction and the tensile axis, ϕ is the angle between the normal to slip plane and the tensile axis, and σ is the normal tensile stress.

Knowing that the macroscopic and microscopic work are equal, $\sigma \cdot \epsilon = \tau \cdot \gamma$, the resolved shear strain can be calculated as:

$$\gamma = \frac{\epsilon}{\cos\phi \cos\lambda} \tag{5.7}$$

Thus, from equation 5.6 and 5.7, it is obtained that:

$$\frac{d\sigma}{d\epsilon} = \frac{\partial\tau}{\partial\gamma} \cdot \frac{1}{(\cos\phi\cos\lambda)^2} = \frac{\partial\tau}{\partial\gamma} \cdot \frac{1}{m^2} \tag{5.8}$$

where m is the Schmid factor.

Considering FCC crystals in figure 5.21 (b), there are 4 different slip planes with slip directions on each plane along the dashed lines. The normals to the slip planes are [111] (ABC), [11$\bar{1}$] (ABD), [$\bar{1}$11] (ACD) and [$\bar{1}$1$\bar{1}$] (BCD). The

six slip directions are $[011]/[0\bar{1}\bar{1}]$, $[0\bar{1}1]/[01\bar{1}]$, $[101]/[\bar{1}0\bar{1}]$, $[10\bar{1}]/[\bar{1}01]$, $[110]/[\bar{1}\bar{1}0]$, and $[1\bar{1}0]/[\bar{1}10]$.

The tensile axis in the simulation is along [100] direction and all the slip systems in the crystal are symmetric to this axis. It has been shown that for such a multislip deformation, the macroscopic hardening rate $\frac{d\sigma}{d\epsilon}$ can be expressed similarly as in equation 5.8 as[68]:

$$\frac{d\sigma}{d\epsilon} = M^2 \frac{\partial \tau}{\partial \gamma} \tag{5.9}$$

where M is called Taylor factor. The only difference of this equation from equation 5.8 is that the Taylor factor M is used to count for the contribution of plastic deformation from multislip systems to the average macroscopic deformation. The Taylor factor is calculated to have a value around 3 for FCC crystals, which give the relation $\frac{d\sigma}{d\epsilon} \approx 10 \times \frac{\partial \tau}{\partial \gamma}$.

It is obvious that the simulated hardening rates $\frac{d\sigma}{d\epsilon}$ on the order of $\frac{\mu}{30} \sim \frac{\mu}{20}$ are in very good agreement with experimental results expressed in the form of $\frac{\partial \tau}{\partial \gamma}$ according to above analysis.

On the other hand, direct measured $\frac{d\sigma}{d\epsilon}$ from experimental result of a tensile stress-strain curve[69] compares well with simulation results. The curve for single crystal copper is shown in figure 5.22. The tensile axis here is 5^o from $[\bar{1}00]$ toward [011], which activates almost symmetric multislip in the experiment. The hardening rate of the curve is calculated to be on the order of $\frac{\mu}{20}$.

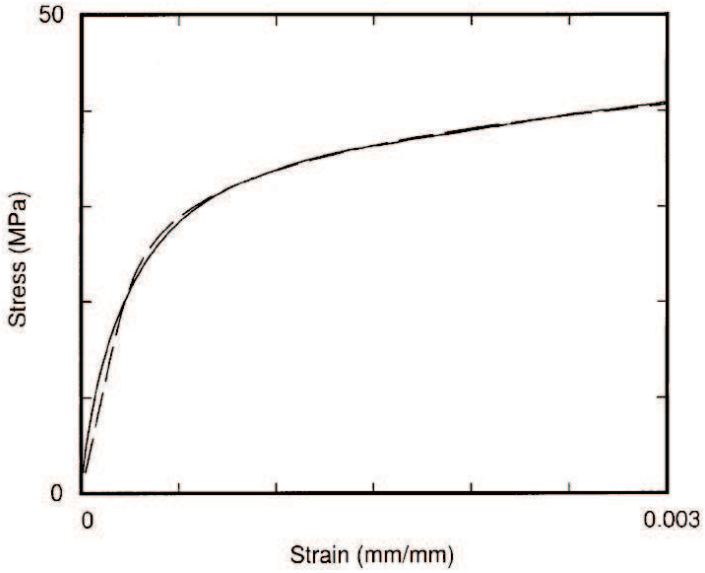

Figure 5.22: A stress-strain curve to 0.3% obtained from experiments shows hardening rate on the order of $\frac{\mu}{20}$[69].

CHAPTER 6

Multipole Representation of The Elastic Field of Dislocation Ensembles and Statistical Extrapolation of DD Simulation

6.1 Introduction

The development of a physically-based theory of plasticity has been one of the most challenging endeavors attempted in recent years. Despite the recognition of the inadequacy of continuum mechanics to resolve important features of plastic deformation, attempts to include the physics of plastic deformation through constitutive relations are far from satisfactory. This is particularly evident for the resolution of critical phenomena, such as plastic instabilities, work hardening, fatigue crack initiation, persistent slip band (PSB) formation, etc.

Although DD has been successfully applied to a wide range of physical problems, especially for problems involving length scales in the nano-to-micro range[70, 71], the extension of the approach to larger length scales (e.g. for application in polycrystalline material deformation) is still a daunting task. The main impediment in this direction is the lack of methods for systematic and rigorous "coarse-graining" of discrete dislocation processes. Notable recent developments in this area have been advanced by LeSar and Rickman[72].

The main objective in this chapter is to develop a "coarse-graining" approach

for evaluation of the elastic field of large dislocation loop ensembles of arbitrary geometric complexity. The method is an extension of the Lesar-Rickman multipole expansion of the elastic energy of dislocation ensembles[72]. The broad "coarse-graining" objective of this chapter is associated with a number of motivating reasons for this development, as given below.

1. To access the physics of plasticity through direct large-scale computer simulations of dislocation microstructure evolution. This is enabled by a substantial reduction of the speed of computation.

2. To remove the "cut-off" distance limitation in dislocation-dislocation interactions, and hence facilitate our understanding of microstructure evolution sensitivity to such computational limitation.

3. To allow efficient determination of the "effective" influence of dislocation arrays (e.g. in some representation of grain boundaries), or complex dislocation blocks (e.g. in dislocation walls and tangles) on the interaction with approaching dislocations.

4. To enable embedding into well established, $O(N)$, computational procedures for particle systems of long-range interactive force fields[73].

5. To shed more light on the connection between discrete dislocation dynamics, the Kröner-Kosevich continuum theory of dislocations[74], and moments of a basic local tensor that characterize the spatial distribution of dislocations.

In the following, a multipole expansion method (MEM) formulation is presented in section 6.2.1. In $O(N)$ methods for calculation of the effective fields in particle systems with long range interaction force fields, moments evaluated for smaller volumes are usually transferred or combined with moments defined in

other volumes. This issue will be explained in section 6.2.2. Results for the far-field expansion of the stress field and interaction forces are given in section 6.2.3, while applications of the method to dislocation arrays in special boundaries or dislocation walls are presented in section 6.2.4. Finally conclusions of this work are presented in section 6.4.

Simulation results shown in the previous chapters are obtained at small strains in comparison to practical situations. To achieve larger strain, special techniques must be applied to overcome the bottleneck for long time scale simulations. Here, based on the statistical distribution of the dislocation loops in the representative volume, a statistical extrapolation method (SEM) is developed to extend the direct dislocation dynamics simulation to large strains.

6.2 Multipole Expansion Method

6.2.1 Formulation of the Multipole Representation

The stress field at any point from a single closed dislocation loop can be written as[40]:

$$\sigma_{ij} = \frac{\mu b_n}{8\pi} \oint [R_{,mpp}(\epsilon_{jmn} dl_i + \epsilon_{imn} dl_j) + \frac{2}{1-\nu} \epsilon_{kmn} (R_{,ijm} - \delta_{ij} R_{,ppm}) dl_k] \quad (6.1)$$

where $\mathbf{R} = \mathbf{Q} - \mathbf{P}$ is the vector connecting field point Q and source point P at dislocations (Figure 6.1 (a)). The stress field per unit volume of an ensemble of dislocation loops in a volume Ω, some of them may not be closed within Ω, is given by:

$$\begin{aligned} \sigma_{ij} &= \frac{\mu}{8\pi\Omega} \left\{ \sum_{\xi=1}^{N_L^{CLOSED}} \oint_{\xi} [R_{,mpp}(\epsilon_{jmn} dl_i + \epsilon_{imn} dl_j) + \frac{2}{1-\nu} \epsilon_{kmn} (R_{,ijm} - \delta_{ij} R_{,ppm}) dl_k] \right. \\ &\left. + \sum_{\xi=N_L^{CLOSED}+1}^{N_L} \int_{\xi} [R_{,mpp}(\epsilon_{jmn} dl_i + \epsilon_{imn} dl_j) + \frac{2}{1-\nu} \epsilon_{kmn} (R_{,ijm} - \delta_{ij} R_{,ppm}) dl_k] \right\} \end{aligned}$$

(6.2)

where N_L^{CLOSED} is the number of closed dislocation loops within the volume Ω, N_L^{OPEN} is the number of open dislocation loops, which intersect the surfaces of the volume Ω, $N_L = N_L^{CLOSED} + N_L^{OPEN}$ is the total number of dislocation loops in the volume Ω.

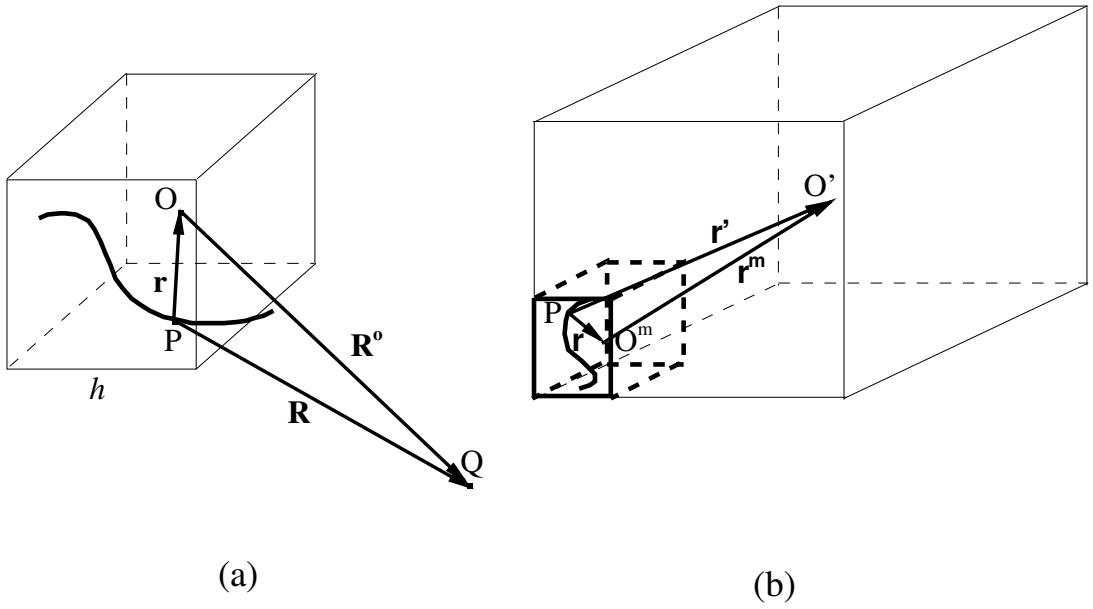

Figure 6.1: Illustration of the geometries of (a) a single volume with center O containing dislocations, (b) a single volume (center O') containing many small volumes with centers O^m.

Suppose that the distance between point P on a dislocation and a field point Q is relatively larger than the size h of a certain volume that contains the dislocation loop, as shown in Figure 6.1. Point O is the center of the volume. Let us write the Taylor series expansion of the derivatives of vector $\mathbf{R}$ at point O as follows:

$$R_{,ijm} = R^o_{,ijm} + R^o_{,ijmk} r_k + \frac{1}{2!} R^o_{,ijmkl} r_k r_l + \frac{1}{3!} R^o_{,ijmkln} r_k r_l r_n + ... \tag{6.3}$$

where $\mathbf{r} = \mathbf{O} - \mathbf{P}$ and $\mathbf{R}^o = \mathbf{Q} - \mathbf{O}$.

Substituting these expansions in equation (6.2), and recognizing that $R^o_{,mpp}$, $R^o_{,ijm}$, $R^o_{,ppm}$ and their higher order derivatives depend only on $\mathbf{R}^o$, it is found:

$$\begin{aligned}
\sigma_{ij} &= \frac{\mu}{8\pi}\Big\{\Big[R^o_{,mpp}(\epsilon_{jmn}\alpha_{ni} + \epsilon_{imn}\alpha_{nj}) + R^o_{,mppq}(\epsilon_{jmn}\beta_{niq} + \epsilon_{imn}\beta_{njq}) \\
&+\frac{1}{2!}R^o_{,mppqs}(\epsilon_{jmn}\gamma_{niqs} + \epsilon_{imn}\gamma_{njqs}) \\
&+\frac{1}{3!}R^o_{,mppqst}(\epsilon_{jmn}\psi_{niqst} + \epsilon_{imn}\psi_{njqst}) + ...\Big] \\
&+\frac{2}{1-\nu}\epsilon_{kmn}\Big[R^o_{,ijm}\alpha_{nk} + R^o_{,ijmq}\beta_{nkq} \\
&+\frac{1}{2!}R^o_{,ijmqs}\gamma_{nkqs} + \frac{1}{3!}R^o_{,ijmqs}\psi_{nkqst} + ...\Big] \\
&-\frac{2}{1-\nu}\delta_{ij}\epsilon_{kmn}\Big[R^o_{,ppm}\alpha_{nk} + R^o_{,ppmq}\beta_{nkq} \\
&+\frac{1}{2!}R^o_{,ppmqs}\gamma_{nkqs} + \frac{1}{3!}R^o_{,ppmqst}\psi_{nkqst} + ...\Big]\Big\} \qquad (6.4)
\end{aligned}$$

where the dislocation moments of zeroth order within the volume Ω are defined as:

$$\begin{aligned}
\alpha_{ij} &= \frac{1}{\Omega}\sum_{\xi=1}^{N_L^{CLOSED}}\oint_\xi E^\xi_{ij}dl + \frac{1}{\Omega}\sum_{\xi=N_L^{CLOSED}+1}^{N_L}\int_\xi E^\xi_{ij}dl \\
&= \frac{1}{\Omega}\sum_{\xi=N_L^{CLOSED}+1}^{N_L}\int_\xi E^\xi_{ij}dl \qquad (6.5)
\end{aligned}$$

where $dl = |d\mathbf{l}|$ is an infinitesimal line length along the unit tangent $\mathbf{t}$. The Eshelby rational tensor E_{ij}, defined as $E^\xi_{ij} = b^\xi_i t^\xi_j(\mathbf{P})$, is a local tensor because it is defined at point $\mathbf{P}$ on a loop ξ, where t^ξ_i is the tangent vector at position $\mathbf{P}$ and $\mathbf{b}^\xi$ is the Burgers vector of the loop. It is clear that the only contribution to the tensor α_{ij} is from open loops (i.e. the second term), since the contribution of closed loops is identically zero by virtue of the closed loop property. Equation 6.5 gives Nye's dislocation density tensor α_{ij}[75, 76]. This tensor is directly related

to the lattice curvature tensor $\boldsymbol{\kappa}$ by[74]:

$$\boldsymbol{\kappa} = \frac{1}{2} Tr(\boldsymbol{\alpha}) \boldsymbol{I} - \boldsymbol{\alpha} \tag{6.6}$$

where $\mathbf{I}$ is the second-order unit tensor. Higher-order tensors $\boldsymbol{\beta}$, $\boldsymbol{\gamma}$, $\boldsymbol{\psi}$, ..., correspond to higher-order moments of the Eshelby rational tensor, and are defined as:

$$\begin{aligned}
\beta_{ijk} &= \frac{1}{\Omega} \sum_{\xi=1}^{N_L} \int_{\xi} r_k E_{ij} dl \\
\gamma_{ijkl} &= \frac{1}{\Omega} \sum_{\xi=1}^{N_L} \int_{\xi} r_k r_l E_{ij} dl \\
\psi_{ijklq} &= \frac{1}{\Omega} \sum_{\xi=1}^{N_L} \int_{\xi} r_k r_l r_q E_{ij} dl \\
\zeta_{ijklq...p} &= \frac{1}{\Omega} \sum_{\xi=1}^{N_L} \int_{\xi} r_k r_l r_q \dots r_p E_{ij} dl
\end{aligned} \tag{6.7}$$

The stress field resulting from a dislocation ensemble within the volume Ω can be written as:

$$\begin{aligned}
\sigma_{ij} = \frac{\mu\Omega}{8\pi} \sum_{t=0}^{\infty} \frac{1}{t!} \Big[& R^o_{,mppa_1...a_t} (\epsilon_{jmn} \langle \zeta_{nia_1...a_t} \rangle + \epsilon_{imn} \langle \zeta_{nja_1...a_t} \rangle) \\
& + \frac{2}{1-\nu} \epsilon_{kmn} R^o_{,ijma_1...a_t} \langle \zeta_{nka_1...a_t} \rangle - \frac{2}{1-\nu} \delta_{ij} \epsilon_{kmn} R^o_{,ppma_1...a_t} \langle \zeta_{nka_1...a_t} \rangle \Big]
\end{aligned} \tag{6.8}$$

where $\langle \zeta_{ijk...} \rangle$ represent the moments defined above of different orders, as α_{ij}, β_{ijk}, γ_{ijkl}, etc. These moments depend only on the selected center point O and the distribution of the dislocation microstructure within the volume. They can be evaluated for each volume independently. After the moments are determined, the stress field and interaction forces on other dislocations that are sufficiently well separated from the volume Ω are easily obtained.

6.2.2 Rules for Combination of Moments

For a fixed field point, if the distance of a volume to this point is larger than its characteristic size, moments obtained from smaller sub-volumes can be utilized to generate moments for the total volume. This procedure is similar to the "parallel axis theorem" for shifting moments of inertia for mass distributions in mechanics. Suppose that this large volume is composed of several sub-volumes and multipole expansions are available for each sub-volume, a procedure to obtain multipole expansion for the large volume from those for the sub-volumes is developed instead of doing the calculations again for each dislocation loop. This idea is very suitable for hierarchical tree algorithms, such as the Greengard-Rokhlin method[48]. Formulations for combination of multipole expansions are described in this section.

Assume that a large material volume Ω centered at $\mathbf{O}^{'}$ contains M small sub-volumes centered at O^m, with their volumes as Ω^m, where m is an index(Figure 6.1 (b)). Here, $\mathbf{r}^m$ is the vector connecting O^m and $O^{'}$. The new vector connecting the center $O^{'}$ and a point on a dislocation is $\mathbf{r}^{'} = \mathbf{r} + \mathbf{r}^m$, where $\mathbf{r}^m = \mathbf{O}^{'} - \mathbf{O}^m$. With the dislocation moments for the m^{th} small material volume as α_{ij}^m, β_{ijk}^m, ..., the moments of dislocations in the m^{th} sub-volume in the large volume can be written as follows:

$$
\begin{aligned}
\alpha_{ij}^{m'} &= \frac{1}{\Omega} \sum_{\xi=N_L^{CLOSED^m}+1}^{N_L^m} \int_\xi E_{ij}^\xi dl = f^m \alpha_{ij}^m \\
\beta_{ijk}^{m'} &= \frac{1}{\Omega} \sum_{\xi=1}^{N_L^m} \int_\xi r_k^{'} E_{ij}^\xi dl \\
&= \frac{1}{\Omega} \sum_{\xi=1}^{N_L^m} \int_\xi (r_k + r_k^m) E_{ij}^\xi dl \\
&= \frac{1}{\Omega} \sum_{\xi=1}^{N_L^m} \int_\xi r_k E_{ij}^\xi dl + \frac{1}{\Omega} \sum_{\xi=1}^{N_L^m} \int_\xi r_k^m E_{ij}^\xi dl
\end{aligned}
$$

$$
\begin{aligned}
&= f^m(\beta^m_{ijk} + r^m_k \alpha^m_{ij}) \\
\gamma^{m'}_{ijkl} &= \frac{1}{\Omega}\sum_{\xi=1}^{N^m_L}\int_\xi r'_k r'_l E^\xi_{ij} dl \\
&= f^m(\gamma^m_{ijkl} + r^m_k \beta^m_{ijl} + r^m_l \beta^m_{ijk} + r^m_k r^m_l \alpha^m_{ij}) \\
&\ldots
\end{aligned} \tag{6.9}
$$

where $f^m = \frac{\Omega^m}{\Omega}$, N^m_L and $N^{CLOSED^m}_L$ are volume fraction, the number of total dislocation loops, and the number of closed loops in the mth volume, respectively.

Then, the total moments of dislocation loop distributions within the large volume are given by:

$$
\begin{aligned}
\alpha_{ij} &= \sum_{m=1}^{M} \alpha^{m'}_{ij} = \sum_{m=1}^{M} f^m \alpha^m_{ij} \\
\beta_{ijk} &= \sum_{m=1}^{M} \beta^{m'}_{ijk} = \sum_{m=1}^{M} f^m \left(\beta^m_{ijk} + r^m_k \alpha^m_{ij}\right) \\
\gamma_{ijkl} &= \sum_{m=1}^{M} \gamma^{m'}_{ijkl} = \sum_{m=1}^{M} f^m \left(\gamma^m_{ijkl} + r^m_k \beta^m_{ijl} + r^m_l \beta^m_{ijk} + r^m_k r^m_l \alpha^m_{ij}\right) \\
&\ldots
\end{aligned} \tag{6.10}
$$

Equation (6.10) can be written in a compact form as:

$$
\zeta_{ija_1\ldots a_n} = \sum_{m=1}^{M} f^m \left\{ \sum_{p=0}^{n} \left[\sum_{q=1}^{C^p_n} \left[\left(r^m_{t_1} r^m_{t_2} \ldots r^m_{t_p} \right) \langle \zeta^m_{ijt_{p+1}\ldots t_n} \rangle \right] \right] \right\} \tag{6.11}
$$

where $n = 0, 1, 2, \ldots$ is the order of the moment. Here, $\sum_{q=1}^{C^p_n}$ means that r^m's sub-index group of $t_1 \ldots t_p$ are selected from the n index group of a_n in a permutational manner, and group of indices $t_{p+1} \ldots t_n$ are the corresponding $n-p$ indices of a_n after the selection.

6.2.3 Numerical Results

Based on the equations developed in the previous sections, the multipole expansion for the stress field of a dislocation ensemble is numerically implemented,

expressed by equation (6.8). The results of the full calculation based on equation (6.2) are considered as reference, and relative errors from the MEM are calculated as $|\sigma_{MEM} - \sigma_{ref}|/\sigma_{ref}$. Tests are performed on a volume with h=10 μm for different expansion orders and different values of R/h. Dislocations are generated randomly inside the volume and with a density of 5×10^8 cm/cm^3. Numerical results are shown in figure (6.2)-(6.6). From these results, it is clear that the approximate moment solutions converge fast. For different values of R/h, the second order expansion gives a relative error less than 1%, while the fourth order expansion gives a relative error less than 0.05%.

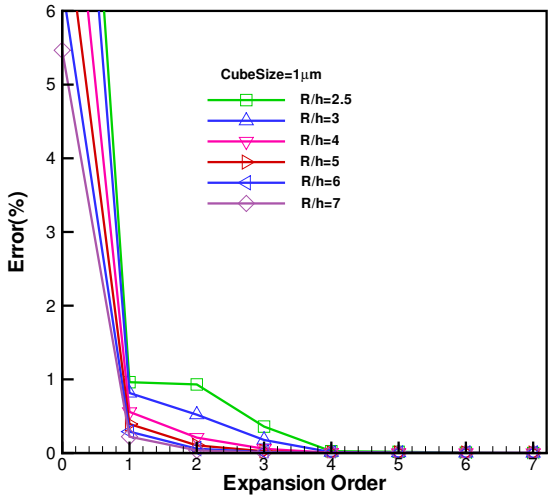

Figure 6.2: Relative error vs the expansion order for different R/h, Volume size $1\mu m$.

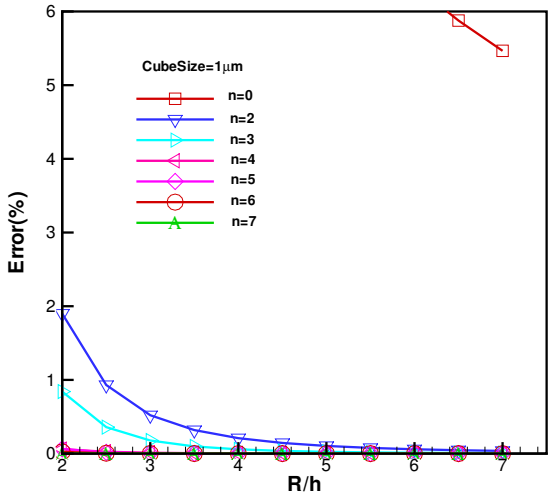

Figure 6.3: Relative error vs R/h for different expansion orders, Volume size $1\mu m$..

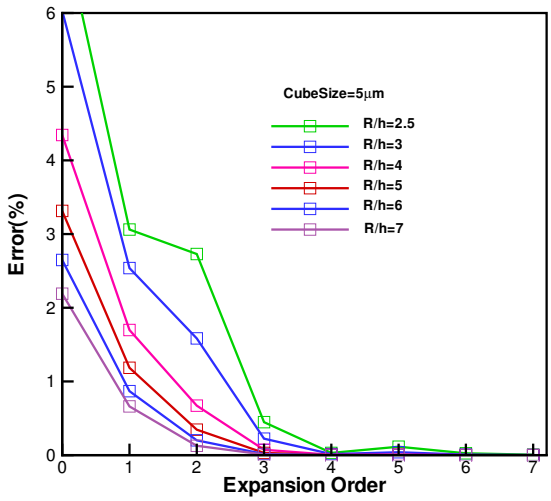

Figure 6.4: Relative error vs the expansion order for different R/h, Volume size $5\mu m$.

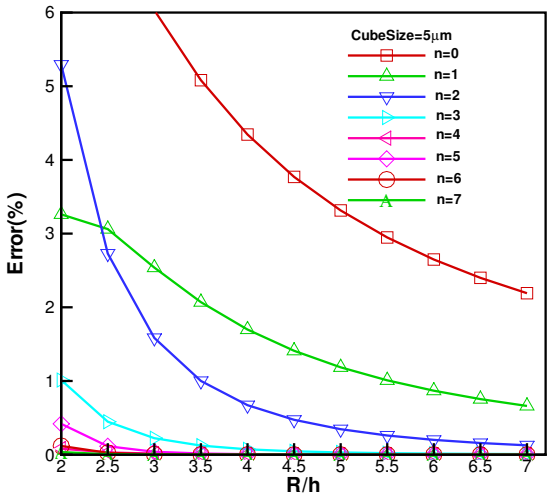

Figure 6.5: Relative error vs R/h for different expansion orders, Volume size $5\mu m$..

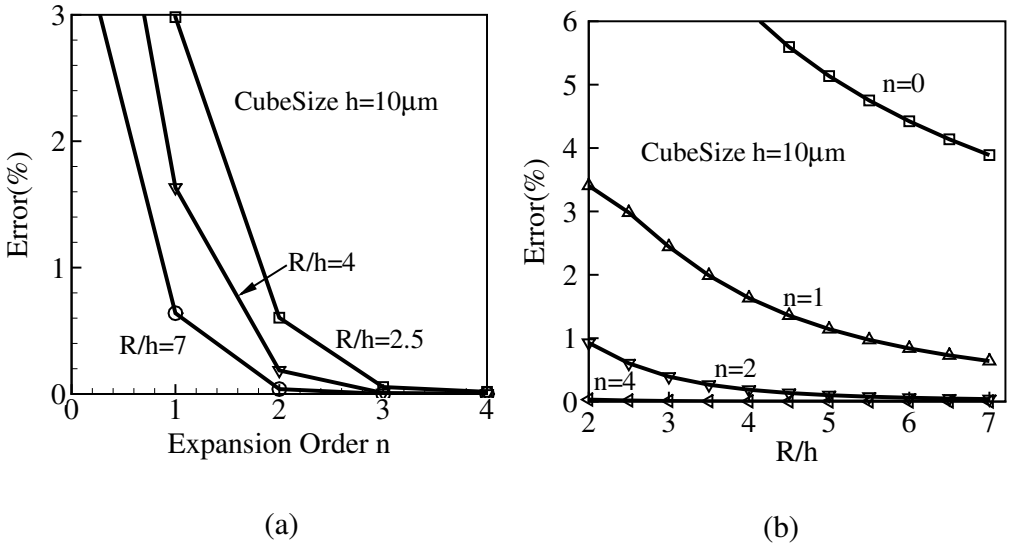

Figure 6.6: Relative error of the MEM vs (a) the expansion order n, (b) the R/h value for a simulation volume with an edge length of 10 μm.

6.2.4 Applications to dislocation boundaries and walls

6.2.4.1 Dislocation Interaction with A Tilt Boundary

An important consequence of heavy plastic deformation is the re-arrangement of dislocations into well-separated tangles or periodic arrays. Dislocation tangles evolve into walls that can act as sources of new dislocations, or stop approaching glide dislocations from neighboring volumes. On the other hand, some grain boundaries can be represented by dislocation arrays. The elastic field generated by grain boundaries in compatibility can thus be determined from the dislocation array representing its structure. Such dislocation microstructures have profound effect on the deformation characteristics of materials, and more often, some "effective" properties are needed. In this section, the feasibility of "effective" elastic representation of periodic dislocation arrays and dislocation walls utilizing the MEM derived earlier is investigated. The effective influence of a tilt boundary on the deformation of a dislocation emitted from a near-by Frank-Read source is first investigated. Then the nature of the Peach-Koehler force on dislocations approaching a dense entanglement of dislocations within a dislocation wall is studied. The following examples are for single crystal Cu, with the following parameters: shear modulus $\mu = 50$ GPa, lattice constant $a = 3.615 \times 10^{-10}$ m, Poisson's Ratio $\nu = 0.31$.

Figure 6.7 shows the geometry of a 1° tilt boundary containing 35 dislocations with $\frac{1}{2}[\bar{1}01]$ Burgers vector. A Frank-Read(F-R) source is located 1 μm away from the tilt boundary. The source, which lies on the [111] glide plane, and emits dislocations with $[\bar{1}2\bar{1}]$ tangent vector and $\frac{1}{2}[\bar{1}01]$ Burgers vector as well. The initial length of the F-R source dislocation between pinned ends is 700 a. A constant uniaxial stress of 25 MPa is applied in the [100]-direction.

Dislocation motion under the influence of the externally applied stress and the internal stress generated by the tilt boundary is determined using the method of Parametric Dislocation Dynamics(PDD)[39, 40]. Interaction forces between the tilt boundary and the F-R source dislocation are calculated by two methods:(1) the fast sum method[3], which adds up the contributions of every dislocation segment within the boundary; (2) the current MEM up to second-order quadropole term. Dislocation configurations at different time steps are shown in figure 6.8(a). The relative error in the MEM in the position of the dislocation (at its closest point to the tilt boundary) is shown in Figure 6.8(b). The results of the simulation show that the MEM is highly accurate (error on the order of 0.4%), and that the overall dislocation configuration is indistinguishable when evaluated by the two methods. However, the MEM is found to be 22 times faster than the full field calculation.

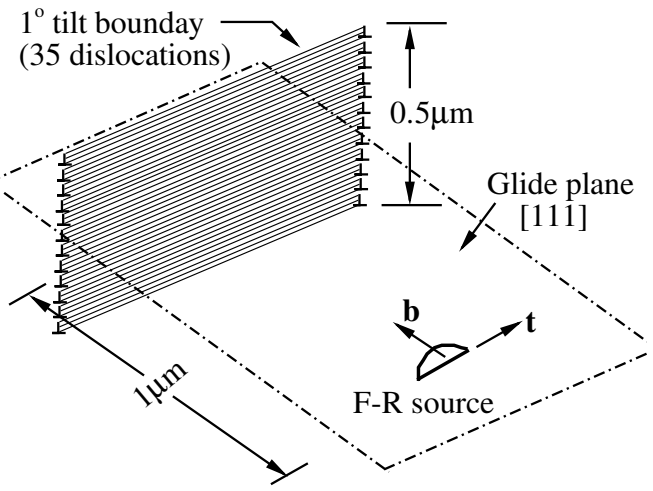

Figure 6.7: Illustration of a tilt boundary. A single dislocation from an F-R source lies on the [111] glide plane with Burgers vector $\frac{1}{2}[\bar{1}01]$ interacts with the tilt boundary.

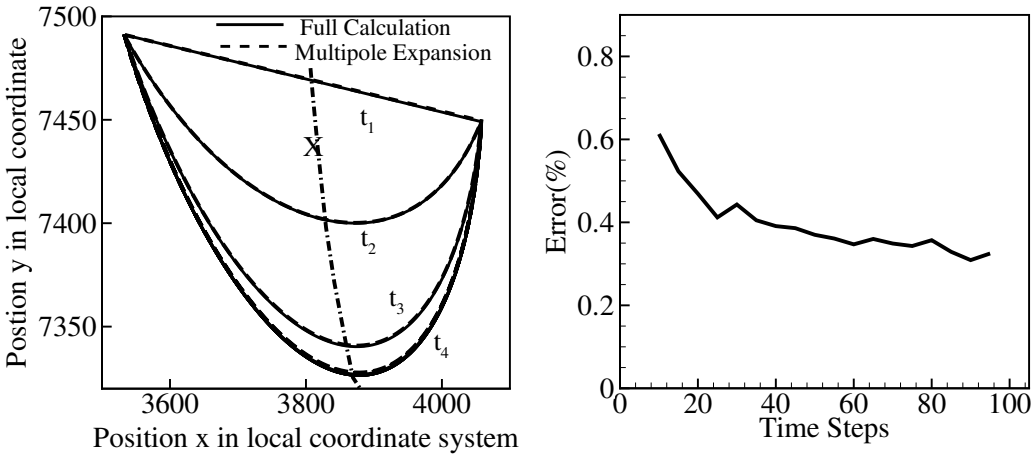

(a) (b)

Figure 6.8: (a)Dislocation configurations at different simulation time steps: t_1=0 ns, t_2=0.31 ns, t_3=0.62 ns, t_4=1.23 ns, (b)Relative error of the dislocation position along the line X in (a).

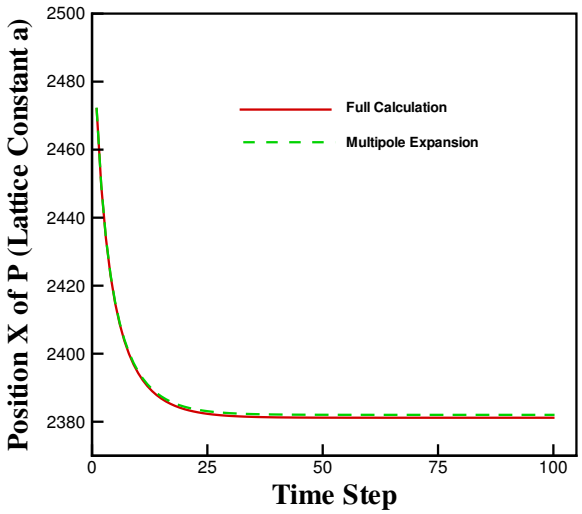

Figure 6.9: Comparison of the position of a moving point due to different methods.

6.2.4.2 Dislocation Interaction with a Dense Dislocation Wall

The physical role of dislocation walls in material deformation is recognized to be significant because they control the free path of mobile dislocations within subgrains[77]. Dislocation walls generally contain high dislocation densities. Therefore, explicit large-scale simulation of the interaction between these walls and approaching dislocations can present computational difficulties. If the nature of decay of the elastic field away from the wall is determined, this would be helpful in studies of dislocation interaction with such walls without the excessive details.

A special algorithm was designed to implement the MEM in dense dislocation walls. The wall was divided into many small volumes, and a hierarchical tree structure was constructed on the bases of these small volumes. Each level of the hierarchical tree contains one or several nodes that correspond to specific volumes of the wall. Larger volumes correspond to higher levels of the tree. For each volume, the following properties of center, size, dislocation distribution and various moments are determined. Dislocation moments for the lowest level volumes are first calculated. Then, by using Equation (6.11), dislocation moments for upper tree levels can be easily determined.

The procedure for calculations of the Peach-Koehler force on an approaching dislocation at point P is as follows:

1. The distance between the volume center and the point P is first evaluated. If the distance is larger than the volume's size, MEM is used.

2. If the distance is smaller than the volume size and the volume does not have sub-volumes, the P-K force is determined by full calculation.

3. If the distance is smaller than the volume's size and the volume has sub-volumes, the algorithm checks on the distance between P and the center of

each sub-volume, and the above procedures are repeated.

Figure 6.10 shows a dislocation wall structure with a density of 5×10^{10} cm/cm^3. The wall dimensions are 5 μm×5 μm×0.2 μm. The P-K force on a small dislocation segment, located at various positions along the center line X, with Burgers vector $\frac{1}{2}[10\bar{1}]$ was evaluated by both MEM and full calculations. The results of the P-K force and the relative errors are plotted in figure 6.11.

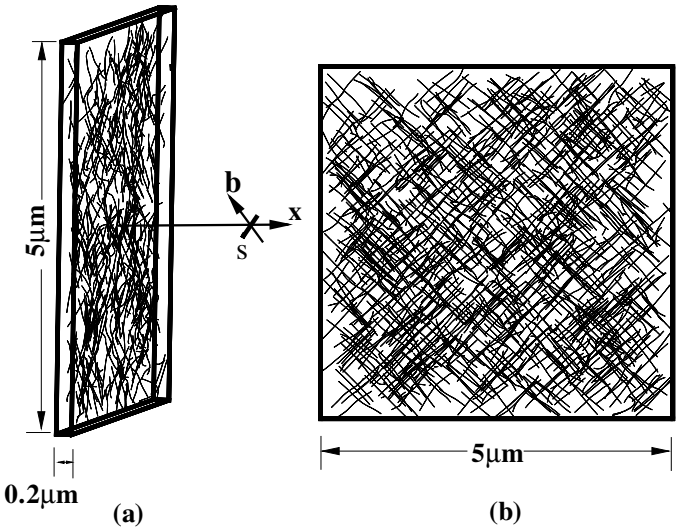

Figure 6.10: Dislocation wall structure with dislocation density 5×10^{10} cm/cm^3. A small dislocation segment S with Burgers vector $\frac{1}{2}[10\bar{1}]$ lies along x.

While the relative error using MEM of order 2 is very small (see Figure 6.11(b)), a great advantage in computational speed is gained. The results (figures 6.12 and 6.13) show that the CPU time (on a Pentium-4 CPU, 2.26GHz) increases almost linearly from 416 seconds to 3712 seconds for the full calculation, when the number of dislocations in the wall increases from 250 to 2200. However, the CPU time does not change much for the MEM (varying from 39 seconds to 40 seconds) for the same increase in the number of dislocations. For the case

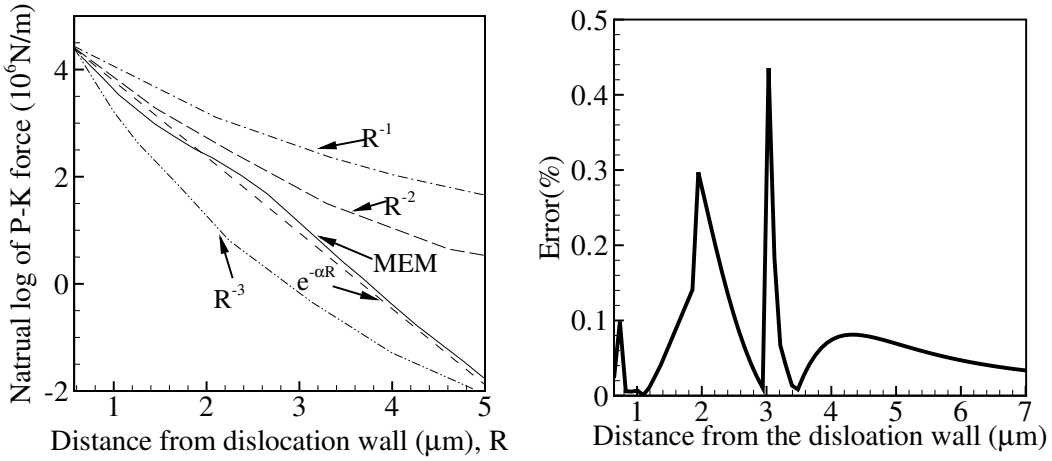

(a) (b)

Figure 6.11: (a) P-K forces on a small dislocation segment at different positions along direction x, (b) Relative error of the P-K force from MEM with respect to that from full calculation.

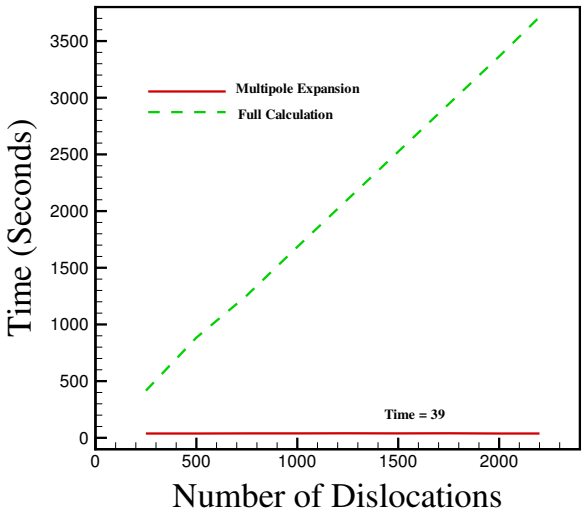

Figure 6.12: CPU time used by multipole expansion method and full calculation method in the case of evaluation of P-K forces.

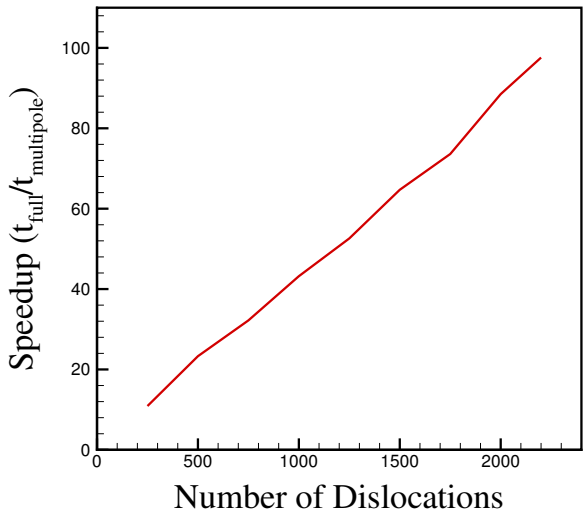

Figure 6.13: Speedup factor of the multipole expansion method to the full calculation method in the case of evaluation of P-K forces.

of 2200 dislocations within the wall, a speedup factor of almost 100 is achieved for the MEM. Recognizing that the CPU time for the MEM is almost constant and mostly dependent on the hierarchical tree structure, it is concluded that the method is very suitable for large scale simulations, which involve high dislocation densities.

It is of interest to determine the decay nature of the elastic field emanating from dislocation walls. Figure 6.11(a) shows a comparison between various forms of the spatial decay of the P-K force as a function of the distance R away from the wall, normalized to the force at $R_0 = 0.59$ μm. It is seen that the force decays faster than R^{-2}, and it can be simply represented by an exponential function of the form:

$$F(R) = F(R_0)e^{-\alpha(R-R_0)} \tag{6.12}$$

where $\alpha = 1.36$ μm^{-1}. Such simple exponential representation is a result of the

self-shielding of the dislocations within the wall.

6.3 Statistical Extrapolation Method

Simulations in Chapter 5 have shown that the dislocation density increases dramatically during the loading process. Correspondingly, numbers of interacting dislocation segments also increase. Thus, more computation is required after the simulation has run for a period of time and strain. It is not difficult to draw the conclusion that the simulation will become slower and slower while the system is becoming larger and larger. An different approach to target this problem is to neglect some of the intermediate simulations on microstructures. The statistical extrapolation method uses the relation between applied strain and dislocation distribution parameters obtained from previous steps of simulation at strain ϵ_1 to extrapolate the relation to a higher strain ϵ_2. Direct simulations between ϵ_1 and ϵ_2 are omitted. Dislocation microstructure and measured external load are assumed to follow the statistical relation in previous simulations. Direct simulation resumes at strain ϵ_2 on a reconstructed microstructure corresponding to the strain ϵ_2 and goes to another higher strain level. The predicted strain-stress relation in this step is used to adjust the previous results and for followed extrapolations. By repeating the procedure, it is anticipated to be easier to reach higher strain simulations with less computation compared to direct simulations all the way up. Following results illustrate the method.

As shown in figure 6.14, there are 3 steps for the method. Direct numerical simulations are performed for strains below 0.3%, which is the first step. For strains larger than 0.3%, instead of doing direct simulations for all the degrees of freedom of the system, the dislocation density is extrapolated to 0.6% strain. At this strain level, the dislocation density is twice as at 0.3%. The microstructure at

a strain of 0.6% is generated by adding the same microstructure at 0.3% to double the original density but with a rigid translation of the original microstructure with the translation distance as half the size of the simulation cube.

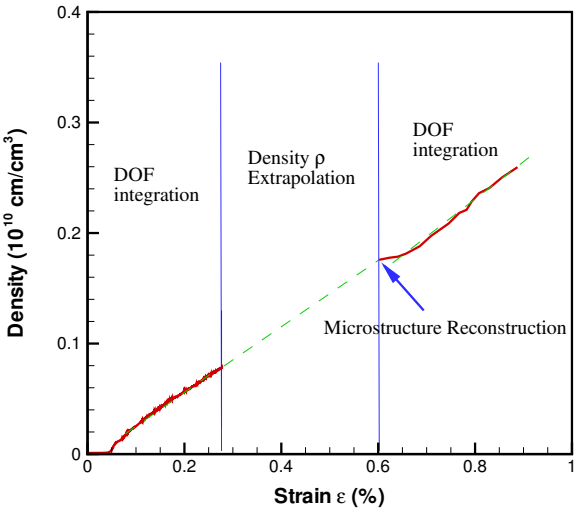

Figure 6.14: Extrapolation of the dislocation density to larger strains

The regenerated microstructure is first relaxed and then the same simulation procedure used in the first step (described in section 5.2) is applied to the current microstructure to obtain the new stress-strain relation. Results are shown in figure 6.15. This new stress-strain curve will represent the deformation of materials beyond 0.6% strain. On completing the second stage to obtain the stress-strain curve at this strain level, a full stress-strain curve for the entire strain range from 0 to 1% is obtained by connecting the two separated stress-strain curves. Here it is assumed that the evolution of the dislocation density between 0.3% and 0.6% will follow the same rate determined from the simulations between 0 and 0.3% strain.

By repeating the process, the stress-strain relationship for larger strains can

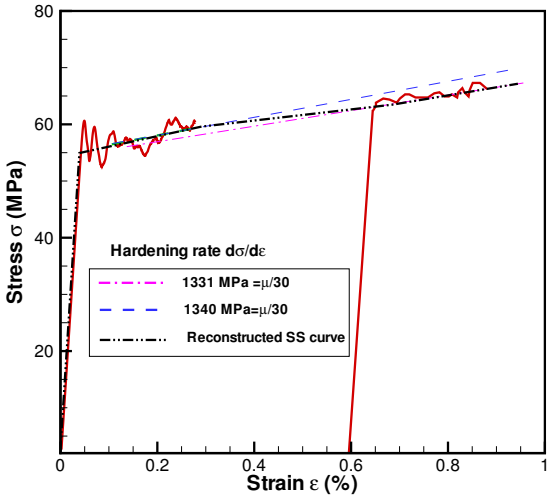

Figure 6.15: Stress-strain curve from the extrapolation method extends to larger strain.

be simulated.

6.4 Discussion

The MEM presented here shows a number of features that facilitate investigations of the physical and computational aspects of large dislocation ensembles in materials undergoing plastic deformation. The following conclusions are drawn for this chapter:

(1) By re-expressing the elastic field of dislocation ensembles as a series solution of moments, the relative contributions of open loops, dipoles, quadropoles, etc are easily separated out.

(2) The method results in significant computational advantages as compared to calculations performed in most dislocation dynamics simulation method. First,

vast computational speed-up is achieved, especially in simulations of dense dislocation interactions. Second, the method offers a simple algebraic procedure for transfer of moments from one volume to another, in a manner similar to the parallel axis theorem for moments of inertia in the mechanics of distributed masses. This property is well-suited to algorithms based on hierarchical tree methods that are now efficiently used in $O(N)$ calculations.

(3) The zeroth order term in the MEM expansion is the Nye's dislocation density tensor, which is a direct measure of lattice curvature, and is affected only by open dislocation loops within the ensemble. Diagonal components of this tensor describe screw dislocations, while off-diagonal components represent edge dislocations. On the other hand, higher order moments of the Eshelby tensor are associated with definite length-scale measures that may be useful in connections between discrete dislocation simulations and the continuum theory of dislocations.

(4) The analysis of dense dislocation walls indicates that the Peach-Koehler force has an exponential decay character as a result of mutual shielding effects of multipole dislocations within random ensemble constituting the walls.

With the statistical extrapolation method, dislocation dynamics simulations can be extended to large strains in comparison to real experimental situation which makes it possible to study the entire range of the deformation of single crystals. The combination of MEM and SEM will be able to predict the mechanical behavior of materials with a simulation containing a much larger collective system of dislocations.

CHAPTER 7

Conclusions

With the development of advanced material technologies and the desire to fully understand the physical nature of plastic deformation, fundamental investigations of the mechanisms of dislocation motion and its relation to the mechanical properties has become an important topic. Direct numerical simulation of dislocation motion and interaction has been developed through the past decade and has become more mature as a scientific discipline. Future developments are becoming easier on the base of past successes. The theory of dislocation dynamics has been applied to explain many phenomena. The understanding from these explanation will enhance the design and manufacturing of stronger materials that are widely demanded in those advanced and traditional areas.

Although computer technology has provided a lot of computational power for simulation, it is still not satisfactory when parallel computational techniques are not used and real material simulations are in demand. Besides the development of a physical theory of dislocations, the development of better computational methodology is another critical point to achieve the objective of direct numerical simulation of materials.

In this work, both analytical understanding of material deformation and numerical implementation of simulations are explored in details with the method of parametric dislocation dynamics. The main focus of the work is on efficient computational implementation of the method and on its application to thin films

and single crystal material deformation.

In chapter 2, description of dislocation motion is introduced by the derivation of equations of motion, equations of dislocation geometry and equations for the elastic fields of dislocation loops. These equations are fundamental for the theory of dislocation dynamics, and they need to be implemented into the computer code and to be solved numerically. Our solution gives simple equations based on operations of vectors and tensors, which are very easy to be implemented and are critical to large scale simulations.

In chapter 3, a parallel computer code is presented to utilize the computational power provided by parallel computing techniques based on computer clusters. The concept of dislocation nodal-points is derived to translate the line defect to a particle-like defect. Dislocation loops are represented by points and these points are distributed to different processors. Similar implementation of the hierarchical representation of the computational domain is introduced into the code and 3 concepts of the global, local and ghost trees are created. The test results show that the computational speed has been greatly improved with great communication and load balancing control. The code provides a useful tool for large scale dislocation dynamics simulations.

In chapter 4, dislocation motion in thin films is investigated through the dislocation dynamics method to study the mechanisms that control the plastic deformation of materials with small size. Because of the existence of free boundary conditions, the motion of dislocations is greatly affected by the image force from the free surface, which is different from dislocation motion in bulk materials. The study reveals the effects on dislocation motion by implementation of the cross-slip mechanism into the computer code. Experimental results are utilized to make comparison with the simulation results. These comparisons show that

the simulation results are in agreement with experiments. This observation gives the numerical simulation direct experimental validation that is always needed to make sure that the simulation correctly and accurately represents real materials deformation. The work suggests that it is completely possible and reasonable to use computer simulation to study the microstructure of the materials if the simulation incorporates key dislocation mechanisms.

In chapter 5, the developed parallel computer code is used to simulate the work hardening of single crystal copper and has shown its potential as an effective tool to solve many problems of plasticity. Initial work hardening stage II has been predicted with hardening rates on simulated stress-strain curves in good agreement with experimental data. Dislocation microstructure evolution is obtained from the simulation along with detailed information, such as dislocation density as a function of strain, which can be used for further analysis.

In chapter 6, a multipole expansion method for dislocation interaction is presented. The method is used for the determination of elastic stress fields of dislocation ensembles, such as dislocation walls, grain boundaries, etc. Application of the method to such ensembles shows that it can greatly increase the calculation speed. As it can be used independently, the method is very suitable for incorporation into the parallel code for large scale simulations and to obtain $O(N)$ algorithm while dealing with far-field interactions with very high accuracy. In developing this method, it is found that some variables defined in determination of the dislocation geometry are connected to the continuum dislocation theory, which may provide a possible connection between the microscale and macroscale properties of materials. This will help in the implementing of a multiscale model for simulation of materials. A statistical extrapolation method is also presented in this chapter for modeling deformation of materials at large strains.

Through a series of simulations, detailed investigation of material microstructure and macroscale mechanical properties were performed by the method of dislocation dynamics. The result show that numerical simulations can be of great help in understanding material deformation.

CHAPTER 8

Appendix

8.1 R and Its Derivatives

R is the vector connecting a field point Q and another point P on the dislocation or O, center of the volume (see Figure 6.1). **R** and its derivatives are used in expressions of displacements, strains, stresses and energies of dislocations[40]. Here, we define a way to express **R** and its derivatives in compact tensor forms.

Define

$$\mathbf{R} = \{x_i\} \text{ and } \mathbf{g} = \left\{\frac{x_i}{R}\right\} \tag{8.1}$$

where $R = |\mathbf{R}|$. Thus,

$$\begin{aligned}
R_{,i} &= \frac{x_i}{R} = g_i && (8.2)\\
R_{,ij} &= \frac{\delta_{ij}}{R} - \frac{x_i x_j}{R^3} = -\frac{1}{R}(-\delta_{ij} + g_i g_j) && (8.3)\\
R_{,ijk} &= -\frac{\delta_{jk}x_i + \delta_{ik}x_j + \delta_{ij}x_k}{R^3} + \frac{3x_i x_j x_k}{R^5}\\
&= \frac{1}{R^2}\left[-\left(\delta_{jk}g_i + \delta_{ik}g_j + \delta_{ij}g_k\right) + 3g_i g_j g_k\right] && (8.4)\\
R_{,ijkl} &= -\frac{\delta_{ij}\delta_{kl} + \delta_{ik}\delta_{jl} + \delta_{il}\delta_{jk}}{R^3}\\
&\quad + \frac{3(\delta_{jk}x_i x_l + \delta_{ik}x_j x_l + \delta_{ij}x_k x_l + \delta_{kl}x_i x_j + \delta_{jl}x_i x_k + \delta_{il}x_j x_k)}{R^5}\\
&\quad - \frac{3\cdot 5 x_i x_j x_k x_l}{R^7}\\
&= -\frac{1}{R^3}\left[(\delta_{ij}\delta_{kl} + \ldots) - 3\left(\delta_{jk}g_i g_l + \ldots\right) + 3\cdot 5 g_i g_j g_k g_l\right] && (8.5)
\end{aligned}$$

$$\ldots \tag{8.6}$$

Based on the above derivations and after careful analysis, we can write these derivatives as:

$$\begin{aligned} R_{,a_1a_2\ldots a_n} &= \left(\frac{-1}{R}\right)^{n-1} \sum_{m=0}^{|\frac{n}{2}|} \{(-1)^m (2n-3-2m)!! \\ &\quad \sum^{C_n^{2m}(2m-1)!!} \left(\delta_{t_1t_2}\delta_{t_3t_4}\ldots\delta_{t_{2m-1}t_{2m}} \cdot g_{t_{2m+1}}g_{t_{2m+2}}\ldots g_{t_n}\right)\} \end{aligned} \tag{8.7}$$

where t_1, t_2, ..., t_{2m} are a group of indices selected from a_n in a permutation manner, and t_{2m+1}, ..., t_n are the other group of a_n after such a selection. The summation $\sum^{C_n^{2m}(2m-1)!!}$ means taking sum over all combinations.

By defining

$$\mathbf{1} = \{e_i\} \tag{8.8}$$

and,

$$\mathbf{R}^{(n)} = \{R_{,a_1a_2\ldots a_n}\} \tag{8.9}$$

we can write equation (8.7) as:

$$\mathbf{R}^{(n)} = \left(\frac{-1}{R}\right)^{n-1} \sum_{m=0}^{|\frac{n}{2}|} \left\{(-1)^m (2n-3-2m)!! \sum^{C_n^{2m}C_{2m}^2} \left[(\amalg \otimes^{n-2m} \mathbf{g})(\amalg \otimes^{2m} \mathbf{1})\right]\right\} \tag{8.10}$$

In this equation, m is the number of δ's and is from 0 to $|\frac{n}{2}|$ which indicates the largest integer not larger than $n/2$. The symbol $\amalg\otimes^n$ indicates that there are a number of n items of $\mathbf{g}$ or $\mathbf{1}$ with the operation $\otimes$. The second summation $\sum^{C_n^{2m}C_{2m}^2}$ means doing summing in a permutation and combination manner, with the number of items $\mathbf{1}$ as $2m$ and the number of items $\mathbf{g}$ as $n-2m$. For example, with $m=1$ and $n=4$, we have:

$$\sum^{C_n^{2m}(2m-1)!!} \left[(\amalg \otimes^{n-2m} \mathbf{g})(\amalg \otimes^{2m} \mathbf{1})\right] = \sum^{C_4^2} \left[(\amalg \otimes^2 \mathbf{g})(\amalg \otimes^2 \mathbf{1})\right]$$

$$= \mathbf{1}\otimes\mathbf{1}\otimes\mathbf{g}\otimes\mathbf{g}+\mathbf{1}\otimes\mathbf{g}\otimes\mathbf{1}\otimes\mathbf{g}+\mathbf{1}\otimes\mathbf{g}\otimes\mathbf{g}\otimes\mathbf{1}$$
$$+\mathbf{g}\otimes\mathbf{1}\otimes\mathbf{1}\otimes\mathbf{g}+\mathbf{g}\otimes\mathbf{1}\otimes\mathbf{g}\otimes\mathbf{1}+\mathbf{g}\otimes\mathbf{g}\otimes\mathbf{1}\otimes\mathbf{1} \quad (8.11)$$

8.2 List of computer code files

The large scale parallel computer code of UCLA-MICROPLASTICITY contains about 20 files, which include 1 main program, 23 modules, 50 functions and 179 subroutines. The total number of code lines is $11,555$.

8.2.1 List of files

The source files of the code are listed in figure 8.1:

1. Microplasticity.f90	2. SimInitialization.f90
3. SimulationMain.f90	4. Update.f90
5. ZQMPI.f90	6. TreeModule.f90
7. SplitBuild.f90	8. Annihilation.f90
9. CrossSlip.f90	10. Communication.f90
11. MPIModule.f90	12. Module.f90
13. LoopRearrange.f90	14. FunctionMD.f90
15. Dynamics.f90	16. EliminateSmall.f90
17. ComputeStrain.f90	18. Output.f90
19. CommonUsed.f90	20. ReadWritePast.f90

Figure 8.1: Files containing source codes for UCLA-MICROPLASTICITY.

8.2.2 Sample Input/Output

There are two input files, one is named as "materials.txt", which contains the parameters of materials, and the other one is named as "geometry.txt", which contains input of dislocation geometries. The sample files are shown in figure 8.2 and 8.3.

```
&MATERIAL MU=50D9,NU=0.31,LATTICE=3.615D-10, APPLIED_SIG=1.0D2,
DELTA_SIG=1D6, A_CUBE=13832, MOBILITY=1.0D-3,RTOLL=1.0D-4,
ATOLL=1.0D-5, ERROR=1.0D-4, DTIME=1D-11, StrainRate=250,
ElasticCons=131d9, CheckNeiBur=1, dcrit=250, IntegrateMethod=2,
logAnnihilation=0/
&DIMENSIONS MAX_QUAD=16, N_TIMES=500, ILOOP_TIME=2000,
MAX_NODE=10, MAX_LOOP=20, MAX_PLANE=2000, NPOINT_I=5/
```

Figure 8.2: Sample input file "materials.txt".

```
 DEFECT  PLANE  NODES Mil_1 Mil_2 Mil_3 BURG_1 BURG_2    BURG_3
RIGIN_x ORIGIN_
 y ORIGIN_z RADIUS Shift_x Shift_y Shift_z
 frs
 frs         1 2   1.00000000000000      1.00000000000000
1.00000000000000      0.0000000000000000E+000  0.500000000000000
-0.500000000000000      1942.46034320707      1942.46034320707
1942.46034320707            1  0.0000000E+00  0.0000000E+00
 1   1606.67024200737      1478.48575843811
 2  -2811.60139166907     -1851.29956223668
frs
 frs         2 2   1.00000000000000      1.00000000000000
1.00000000000000      0.0000000000000000E+000  0.500000000000000
-0.500000000000000      3557.01367696510      3557.01367696510
3557.01367696510            1  0.0000000E+00  0.0000000E+00
 1  -2811.60139166907     -1851.29956223668
 2   1606.67024200737      1478.48575843811
frs
 frs         3 2   1.00000000000000     -1.00000000000000
1.00000000000000      0.500000000000000   0.0000000000000000E+000
 -0.500000000000000      1942.46034320707      25721.5396567929
1942.46034320707            2  0.0000000E+00  0.0000000E+00
 1   1606.67024200737      1478.48575843811
 2  -2811.60139166907     -1851.29956223668
frs
 frs         4 2   1.00000000000000     -1.00000000000000
1.00000000000000      0.500000000000000   0.0000000000000000E+000
 -0.500000000000000      3557.01367696510      24106.9863230349
3557.01367696510            2  0.0000000E+00  0.0000000E+00
 1  -2811.60139166907     -1851.29956223668
 2   1606.67024200737      1478.48575843811
 frs
 frs         5 2  -1.00000000000000     -1.00000000000000
1.00000000000000      0.0000000000000000E+000 -0.500000000000000
-0.500000000000000      25721.5396567929      25721.5396567929
1942.46034320707            3  0.0000000E+00  0.0000000E+00
 1   1606.67024200737      1478.48575843811
 2  -2811.60139166907     -1851.29956223668
ENDDEFECT
```

Figure 8.3: Sample input file "geometry.txt".

References

[1] D. Weygand, L.H. Friedman, E. Van der Giessen, and A. Needleman. Aspects of boundary-value problem solutions with three-dimensional dislocation dynamics. *Modelling and Simulation in Materials Science and Engineering*, 10(4):1, 2002.

[2] N.M. Ghoniem and R. Amodeo. Computer simulation of dislocation pattern formation. *Solid State Phenomena*, 3 & 4:377, 1988.

[3] N.M. Ghoniem and L.Z. Sun. Fast sum method for the elastic field of 3-d dislocation ensembles. *Phys. Rev. B*, 60(1):128, 1999.

[4] Hussein M. Zbib, Moono Rhee, and John P. Hirth. On plastic deformation and the dynamics of 3d dislocations. *Int. J. Mech. Sci.*, 40(2-3):113–127, 1998.

[5] Benoit Devincre and Ladislas P. Kubin. The modelling of dislocation dynamics: Elastic behavior versus core properties. *Philosophical Transactions: Mathematical, Physical and Engineering Sciences*, 355(1731):2003, 1997.

[6] M. Rhee, H.M. Zbib, J.P. Hirth, H. Huang, and T. Rubia. Models for long-/short-range interactions and cross slip in 3d dislocation simulation of bcc single crystals. *Modelling Simul. Mater. Sci. Eng.*, 6:467–492, 1998.

[7] B Devincre and L.P. Kubin. Simulations of forest interactions and strain hardening in fcc crystals. *Modelling Simul. Mater. Sci. Eng.*, 2:559, 1994.

[8] B. Devincre and L.P. Kubin. Mesoscopic simulations of dislocations and plasticity. *Materials Science and Engineering*, A234-236:8, 1997.

[9] M.C. Fivel, T.J. Gosling, and G.R. Canova. Implementing image stresses in a 3d dislocation simulation. *Modelling Simul. Mater. Sci. Eng.*, 4:581–596, 1996.

[10] M. Fivel, M. Verdier, and G. Canova. 3d simulation of a nanoindentation test at a mesoscopic scale. *Materials Science and Engineering*, A234-236:923, 1997.

[11] C. Depres, C.F. Robertson, and M.C. Fivel. Low-strain fatigue in 316l steel surface grains: a three dimensional discrete dislocation dynamics modelling of the early cycles. part-1: Dislocation microstructures and mechanical behaviour. *Phil. Mag.*, 84(22):2257, 2004.

[12] T.A. Khraishi and H.M. Zbib. Free surface effects in 3d dislocation dynamics: formulation and modeling. *J. Eng. mat. Tech. (JEMT)*, 124(3):342, 2002.

[13] H. Yasin, H.M. Zbib, and M.A. Khaleel. Size and boundary effects in discrete dislocation dynamics: coupling with continuum finite element. *Materials Science and Engineering*, A309-310:294, 2001.

[14] Hussein M. Zbib and T.D. Rubia. A multiscale model of plasticity: Patterning and localization. *Society of Materials Science of Japan*, A:341, 2001.

[15] K.W. Schwarz. Simulation of dislocations on the mesoscopic scale. i. mehtods and examples. *Journal of Applied Physics*, 85(1):108–119, 1999.

[16] K.W. Schwarz. Simulation of dislocation on the mesoscopic scale. ii. application to strained-layer relaxation. *Journal of Applied Physics*, 85(1):120, 1999.

[17] K.W. Schwarz and D. Chidambarrao. Dislocation dynamics near film edges and corners in silicon. *Journal of Applied Physics*, 85(10):7198, 1999.

[18] Wei Cai and et al. Massively parallel dislocation dynamics simulations. In *IUTAM Symposium on Mesoscopic Dynamics of Fracture Process and Material Strength*, Osaka, Japan, July 7-11 2003. Kluwer Academic Publisher.

[19] Geoffrey H. Campbell, Stephen M. Foiles, Hanchen Huang, Darcy A. Hughes, Wayne E. King, David H. Lassila, Daniel J. Nikkel, John Y. Shu, and Valery P. Smyshlyaev. Multi-scale modeling of polycrystal plasticity: a workshop report. *Materials Science and Engineering*, A251:1–22, 1998.

[20] T. Diaz de la Rubia and V.V. Bulatov. Materials research by means of multiscale computer simulation. *MRS Bulletin*, 26(3):169–175, 2001.

[21] Erik Nes. Modelling of work hardening and stress saturation in fcc metals. *Progress in Materials Science*, 41:129–193, 1998.

[22] F.R.N. Nabarro. Work hardening of face-centered cubic single crystals. *Strength of Metals and Alloys*, 3:1667, 1985.

[23] F. Szekely, I. Groma, and J. Lendvai. Statistic properties of dislocation structures investigated by x-ray diffraction. *Materials Science and Engineering*, A309:352, 2001.

[24] P.N.B. Anongba, J. Bonneville, and J.L. Martin. Hardening stages of [112] copper single crystals at intermediate and high temperatures–i. mechanical behaviour. *Acta Metall. Mater.*, 41(10):2897–2906, 1993.

[25] P.N.B. Anongba, J. Bonneville, and J.L. Martin. Hardening stages of [112] copper single crystal at intermediate and high temperatures–ii. slip system and microsturctures. *Acta Metall. Mater.*, 41(10):2907–2922, 1993.

[26] E. Voce. *J. Inst. Metals.*, 74:537, 1948.

[27] E. Voce. *Metallurgia*, 51:219, 1955.

[28] R. Martinez and N. M. Ghoniem. The infuence of crystal surfaces on dislocation interactions in mesoscopic plasticity: A combined dislocation dynamics-finite element approach. *J. Comp. Meth. Engr. Science, CMES*, 3(2):229, 2002.

[29] B.T. Ma and C. Laird. Overview of fatigue behaviors in copper single crystals-i. surface morphology and stage i crack initiation sites for tests at constant strain amplitude. *Act. Metal.*, 37(2):325, 1989.

[30] E.A. Repetto and M. Ortiz. A micromechanical model of cyclic deformation and fatigue-crack nucleation in fcc single crystals. *Acta. Mater.*, 45(6):2577, 1997.

[31] L. Cretegny and A. Saxena. Afm characterization of the evolution of surface deformation during fatigue in polycrystalline copper. *Acta. mater.*, 49:3755, 2001.

[32] E.H. Yoffe. A dislocation at a free surface. *Philosophical Magazine*, 6:1147, 1961.

[33] P.P. Groves and D.J. Bacon. The dislocation loop near a free surface. *Philosophical Magazine*, 22:83, 1970.

[34] Y. Maurissen and L. Capella. Stress field of a dislocation segment parallel to a free surface. *Philosophical Magazine*, 29:1227, 1973.

[35] J. Lothe, V.L. Indenbom, and V.A. Chamrov. Elastic field and self-force of dislocations emerging at the free surfaces of an anisotropic halfspace. *Phys. Stat. Solid.*, 111:671, 1982.

[36] D. Hull and D.J. Bacon. *Introduction to Dislocations*. Pergamon Press, 3 edition, 1984.

[37] A. El-Azab and N.M. Ghoniem. Green's function for the elastic field of an edge dislocation in a finite orthotropic medium. *International Journal of Fracture*, 61:17, 1993.

[38] N.M. Ghoniem and J.M. Huang. Computer simulations of mesoscopic plastic deformation with differential geometric forms for the elastic field of parametric dislocations : Review of recent progress. *J. de Physique*, 11(5):53, 2001.

[39] N.M. Ghoniem, S.H. Tong, and L.Z. Sun. Parametric dislocation dynamics: A thermodynamcis-based approach to investigations of mesoscopic plastic deformation. *Phys. Rev. B*, 61:913, 2000.

[40] N.M. Ghoniem, J. Huang, and Z. Wang. Affine covariant-contravariant vector forms for the elastic field of parametric dislocations in isotropic crystals. *Phil. Mag. Lett.*, 82(2):55–63, 2002.

[41] Nasr M. Ghoniem. Computational methods for mesoscopic, inhomogeneous plastic deformation. In *Proceddings of First Latin American Symposium on Materials Instabilities*. Valpareso, Chile, Kluwer Publication, 2000.

[42] G. Holzapfel. *Nonlinear Solid Mechanics*. Chichester, West Sussex:Wiley, 2000.

[43] Marc Snir, Steve Otto, Steven Huss-Lederman, David Walker, and Jack Dongarra. *MPI—The Complete Reference*, volume 1. The MIT Press, 2 edition, 1998.

[44] William Gropp, Ewing Lusk, and Anthony Skjellum. *Using MPI: Portable Parallel Programming with the Message-Passing Interface*. The MIT Press, 1994.

[45] Jaswinder Pal Singh, Chris Holt, Takashi Totsuka, Anoop Gupta, and John Hennessy. Load balancing and data locality in adaptive hierarchical n-body methods: Barnes-hut, fast multipole, and radiosity. *Journal of Parallel and Distributed Computing*, 27:118, 1995.

[46] H.Y. Wang and R. Lesar. O(n) algorithm for dislocation dynamics. *Philosophical Magazine A*, 71(1):149, 1995.

[47] Jui-Lin Lu and Daniel I. Okunbor. Parallel implementation of 3d fma using mpi. *Proceedings of Second MPI Developer's Conference*, page 119, 1996.

[48] L. Greengard and V. Rokhlin. A fast algorithm for particle simulations. *Journal of Computational Physics*, 73:325–348, 1987.

[49] A.Y. Grama, Vinpin Kumar, and Ahmed Sameh. Scalable parallel formulations of the barnes-hut method for n-body simulations. *Proceedings Supercomputings 94*, page 439, 1994.

[50] M. Amor, F. Arguello, J. Lopez, O. Plata, and E.L. Zapata. A data parallel formulation of the barnes-hut method for n-body simulations. *Proceedings for Applied Parallel Computing, PARA 2000*, page 342, 2000.

[51] A.Y. Grama, Vipin Kumar, and Ahmed Sameh. n-body simulations using message passing parallel computers. *Proceedings of the Seventh SIAM Conference on Parallel Processing for Scientific Computing*, page 355, 1995.

[52] Carl E. Pearson. *Numerical Methods in Engineering And Science*. Van Nostrand Reinhold Company, New York, 1986.

[53] Z.Q. Wang, N.M. Ghoniem, and R. LeSar. Multipole representation of the elastic field of dislocation ensembles. *Physical Review B*, 69(17):174102–07, 2004.

[54] M. Tang, L.P. Kubin, and G.R. Canova. Dislocation mobility and the mechanical response of bcc (ta) single crystals: a mesoscopic approach. *Acta. Materialia*, 46:3221, 1998.

[55] V. V. Bulatov, M. J. Tang, and H. M. Zbib. Crystal plasticity from dislocation dynamics. *MRS Bulletin*, 26:1991, 2001.

[56] F. Pettinari, A. Couret, D. Caillard, G. Molenat, N. Clement, and A. Coujou. Quantitative measurements in in-situ straining experiments in transmission electron microscopy. *Journal of Microscopy*, 203:47, 2001.

[57] B.W. Lagow, I. M. Robertson, M. Jouiad, D. H. Lassila, T. C. Lee, and H. K. Birnbaum. Observation of dislocation dynamics in the electron microscope. *Mat. Sci. Engin. A*, 309:445, 2001.

[58] I.M. Robertson. The effect of hydrgen on dislocation dynamics. *Engin. Fract. Mech.*, 68:671, 2001.

[59] R.J. McCabe, A. Misra, T.E. Mitchell, and K.B. Alexander. A single-tilt tem stereomicroscopy technique for crystalline materials. *Microscopy and Microanalysis*, 9:29, 2003.

[60] J. Bonnevilie and B. Escaig. Cross-slippling process and the stress-orientation dependence in pure cooper. *Acta Metallurgica*, 27:1477–1486, 1979.

[61] J.P. Hirth and J. Lothe. *Theory of Dislocations*. McGraw-Hill, New York, 2 edition, 1982.

[62] D. Turnbull and R.E. Hoffman. The effect of relative crystal and boundary orientations on grain boundary diffusion rates. *Acta Metall.*, 2:419, 1954.

[63] G.R. Love. Dislocation pipe diffusion. *Acta Metall.*, 12:731, 1964.

[64] M Marko and A. Leith. Sterecon–three-dimensional reconstruction from stereoscopic contouring. *J. Struct. Biol*, 116:93, 1996.

[65] E. Van der Giessen and A. Needleman. On the solution of 2-d plasticity problems with discrete dislocations. *Comp. Mater. Model.*, 42:294, 1994.

[66] L.P. Kubin, G. Canova, M. Condat, B. Devincre, V. Pontikis, and Y. Bréchet. Dislocation microstructure and plastic flow: a 3d simulation. *Solid State Phenomena*, 23&24:455, 1992.

[67] M.C. Fivel, C.F. Robertson, G.R. Canova, and L.Boulanger. Three-dimensional modelling of indent-induced plastic zone at a mesoscale. *Acta. Mater.*, 46(17):6183, 1998.

[68] U.F. Kocks H. Mecking and Ch. Hartig. Taylor factors in materials with many deformation modes. *Scripta Materialia*, 35:465, 1996.

[69] W.C. Crone and T.W. Shield. An experimental study of the effect of the hardening on plastic deformation at notch tips in metallic single crystals. *Journal of the mechanics and physics of solids*, 51:1623, 2003.

[70] Nasr M. Ghoniem, Hanchen Huang, Esteban Busso, and Nicolas Kioussis. Multiscale modeling of nano- and micro-mechanics: an overview. *Phil. Mag.*, 83(31-34):3475–3528, 2003.

[71] Nasr M. Ghoniem and Kyeongjae Cho. The emerging role of multiscale modeling in nano- and micro-mechanics of materials. *J. Comp. Meth. Engr. Science*, 3(2):147, 2002.

[72] R. Lesar and J. M. Rickman. Multipole expansion of dislocation interactions i. application to discrete dislocation. *Physical Review B*, 65:144110–1, April 2002.

[73] V. Rokhlin, H. Cheng, and L. Greengard. A fast adaptive multipole algorithms in three dimensions. *Journal of Computational Physics*, 155:468, 1999.

[74] E. Kröner. In R. Balian et al., editor, *Physics of Defects*, chapter Continuum Theory of Defects,Course 3. North-Holland, Amsterdam, 1981.

[75] J.F. Nye. Some geometrical relations in dislocated crystals. *Acta metall.*, 1:153, 1953.

[76] A. Arsenlis and D.M. Parks. Crystallographic aspects of geometrically-necessary and statistically-stored dislocation density. *Acta Mater.*, 47(5):1597, 1999.

[77] Darcy A. Hughes, Shafique M.A. Khan, Andrew Godfrey, and Hussein M. Zbib. Internal structures of deformation induced planar dislocation boundaries. *Material Sciences and Engineering*, A309-310:230–236, 2001.